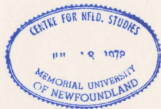


001311



Dynamics of Conformational Gating and Charge Trapping in Dendritic Chromophores

by

© Brent Donald Bruce Myron

B.Sc., Memorial University of Newfoundland, 2002

A Dissertation submitted to the
School of Graduate Studies
in partial fulfillment of the
requirements for the degree of
Doctor of Philosophy

Department of Chemistry
Faculty of Science
Memorial University of Newfoundland

March 22, 2012
St. John's, Newfoundland, Canada

To Karen, Mom, and Dad.

Abstract

The research presented in this Dissertation concerns the elucidating the origin of observed photoinduced dynamics in two distinct types of dendritic chromophores. Physical phenomena such as photon absorption, radiative and non-radiative decay, Förster and Dexter energy transfer, Marcus electron transfer, and Energy Gap Law of non-radiative decay are introduced and discussed in this context.

Following a general introduction of the physical, chemical, and photophysical properties of dendrimers, the unique excited state dynamics of a family of heteroleptic ruthenium polypyridyl complexes of the form $[\text{Ru}(\text{bpy})_2\text{L}]^{2+}$ (where L represents a ligand derivatized with several sizes of poly(phenylenevinylene) dendrimers) are presented and discussed. Laser flash photolysis and emission spectroscopy reveal the presence of atypical risetime kinetics and dual emission in these compounds. It is hypothesized that conformational dynamics about these dendritic groups cause profound attenuation of interligand charge transfer, leading to emission from two separate $^3\text{MLCT}$ states.

The second part of the research involves two families of Fréchet-type dendrimers surrounding a tris(methyl viologen) core, wherein the potent electron accepting ability of the MV^{2+*} excited state drives electron transfer and long-term charge trapping. The structural features of these dendrimers that yield such long-lived charge separated states are addressed in the context of the inverted region for non-radiative decay as described by Energy Gap Law.

Acknowledgements

I would like to thank my supervisor Dr. David Thompson for his guidance, knowledge, and friendship during our lengthy partnership. His passion for research and discovery is as present now as it was when we first met, leading to thought-provoking and, at times, eye-opening discussions. He has always been willing to let me pursue our research objectives in my own way, and I have learned a great deal from the experience. My supervisory committee members, Dr. Peter Pickup and Dr. Graham Bodwell, have been friends and mentors for matters both academic and personal for as long as I have been a part of MUN Chemistry, and for that they will always have my thanks.

I would like to thank past and present Thompson group members in general and Adam Bishop, Jamie Vaters, Amanda Collier, and Steven Smith in particular, for their assistance with school and work, for the laughter, and for the discussions about chemistry, religion, life, and stupid cartoon shows.

While an acknowledgement of the services provided by C-CART is certainly warranted, my thanks to Julie, Louise, Céline, and Linda extend well beyond that simple gesture. I am proud to be "one of the girls" and thankful for their expertise and friendship, as well as their patience with my extended absence as I was completing this Dissertation.

During my Ph.D. program I have been fortunate enough to meet some great chemists and great people. Along with the people I have previously mentioned, Dr. Jean Burnell, Dr. Brian Maclean, Dr. Brandi Langsdorf, and Mrs. Nathalie Vanasse have all had a profound and unique influence on my development as a chemist and as a person.

To Mom and Dad: thank you for your unconditional love and your support for whatever endeavour I chose to undertake. I am who I am today because of your guidance and love, because of the teaching and morals you instilled in your children, and for your continuing influence on my life and the lives of your grandchildren.

To Michael and Jennifer: you have always been there when I needed you, be it for life advice or some such serious topic, or for quoting movies and making stupid faces at each other. I'm making one right now as I type this one-handed; you know which one it is.

To Diane and Ed: I literally could not have gotten to this point without your utter selflessness. You are quick to praise Karen and I for raising two great children, but you deserve a tremendous share of the credit yourselves. Thank you.

To Jacob and Abby - You didn't make this process any easier but, paradoxically, I'm not sure that I would have finished this project without you! Words cannot express how happy and proud I am to have you in my life.

Last but not least, to my best friend, my confidant, my advisor, the mother of my children, and the love of my life:

Karen, for your love, support, and obviously boundless patience, I owe you debt of gratitude that I fear I can never adequately repay. This dissertation is as much yours as it is mine, as I could not have done this without you.

Brent D. B. Myron

March 22, 2012

Table of Contents

Abstract.	iii
Acknowledgements.	iv
Table of Contents.	vii
List of Tables.	xii
List of Figures.	xiii
List of Symbols and Abbreviations.	xxiii

Chapter 1. Introduction.

1.1 Fermi Golden Rule.	1
1.2 Franck-Condon Principle.	3
1.3 Radiative and Non-Radiative Transitions of Excited States.	
1.3.1 Radiative Transitions.	5
1.3.2 Non-Radiative Transitions.	6
1.3.2.1 Total Rate of Non-Radiative Decay.	8
1.3.2.2 Energy Gap Law.	10
1.3.2.3 Attenuation of k_w in Nested Potential Energy Surfaces.	12
1.3.2.4 Spin-Orbit Coupling.	13
1.4 Energy Transfer ($E_N T$) and Electron Transfer ($E_L T$) Theory.	14
1.4.1 An Overview of $E_N T$ Mechanisms.	15
1.4.2 $E_L T$: Marcus Theory.	19
1.4.3 Quantum Mechanical $E_L T$ Theory.	25
1.5 Dendrimers.	
1.5.1 Origins and Development of Dendrimer Research.	27
1.5.2 Synthetic Strategies.	30
1.5.3 Photoinduced $E_N T$ and $E_L T$ in Dendrimers.	34

1.5.4	Poly(aryl ether) (Fréchet-type) Dendrimers.	36
1.5.5	Poly(phenylenevinylene) Dendrimers.	37
1.5.6	Excited State Properties of Stilbene.	39
1.5.6.1	<i>cis-trans</i> Isomerism in Sterically-Hindered Environments.	42
1.6	Conclusion.	43
1.7	References.	44

Chapter 2. Conformational Dynamics of Dendritic Poly(phenylenevinylene)-Substituted Bipyridines in $[\text{Ru}(\text{bpy})_2(\text{L})]^{2+}$ Complexes

2.1	Introduction.	
2.1.1	Photophysics of Ru^{II} Polypyridyl Metal Complexes.	50
2.1.2	The Role of Conformational Dynamics in Chromophoric System Design.	56
2.2	Experimental Details.	
2.2.1	Materials.	61
2.2.2	Synthesis.	62
2.2.3	Instrumentation and Methods.	67
2.3	Results.	
2.3.1	Absorbance Spectra of $\text{G}_n\text{-bpy}$ ($n = 0 - 3$).	77
2.3.2	Absorbance Spectra of RuD_n ($n = 0 - 3$) in Fluid Media.	78
2.3.3	Absorbance Spectra of RuD_n ($n = 0 - 3$) in a Rigid Medium.	80
2.4	Excited States.	
2.4.1	Photochemistry.	82
2.4.2	Emission Spectra.	
2.4.2.1	Fluorescence of $\text{G}_n\text{-bpy}$ in Fluid Media.	85
2.4.2.2	Variable Temperature Phosphorescence Spectra.	88
2.4.2.3	Luminescence Spectra of RuD_n ($n = 0 - 3$) in CH_3CN at RT	89

2.4.2.4	Luminescence Spectra of RuDn ($n = 0 - 3$) in PMMA at RT.	92
2.4.3	Emission Spectral Fitting of RuDn in CH ₃ CN.	94
2.4.4	Time-Resolved Luminescence Decay of the RuDn Dendrimers.	
2.4.4.1	Luminescence Decay in Fluid Media at Room Temperature.	97
2.4.4.2	Luminescence Decay in a Frozen Medium at 77 K.	100
2.4.4.3	Luminescence Decay in a Rigid Medium at RT.	101
2.4.5	Laser Flash Photolysis.	
2.4.5.1	RuD0 in a Fluid Medium at Room Temperature.	102
2.4.5.2	RuD0 in a Rigid Medium at Room Temperature.	104
2.5	Discussion.	
2.5.1	Spectral Properties and Photochemistry of the Gn-bpy Dendrimers.	107
2.5.2	Ground State Photophysics of the RuDn Dendrimers.	111
2.5.3	Excited State Photophysics of the RuDn Dendrimers.	
2.5.3.1	Emission Spectra.	116
2.5.3.2	Emission Spectral Fitting.	117
2.5.3.3	Time-Resolved Luminescence Decay.	120
2.5.3.4	Laser Flash Photolysis and Global Analysis.	121
2.5.4	Elucidation of the Origin of Dual Emission and Growth Kinetics in Luminescence and Transient Absorption of the RuDn Dendrimers.	
2.5.4.1	Luminescence of Impurities or Ligand-Based States.	126
2.5.4.2	The Role of Conformational Gating in the Dynamics and Spectroscopy of a Non-Thermally-Equilibrated ³ MLCT State.	128
2.5.4.3	Attenuation of Interligand Charge Transfer Between Dual Emissive ³ MLCT States.	131
2.5.4.4	Comparison of Models.	134
2.5.5	Re-Evaluation of the Model of Excited State Dynamics of RuDn.	139
2.5.6	The Origin of Ultrafast Excited State Dynamics of the RuDn Dendrimers.	141
2.6	Conclusions and Future Work.	145
2.7	References.	147

Chapter 3. Long-Lived Excited States in Benzyl- and Naphthyl-capped Fréchet-type Dendrimers with a Tris(Methyl Viologen) Core

3.1 Introduction.	
3.1.1 Ground and Excited State Electronic Properties of MV ²⁺ .	153
3.1.2 MV ²⁺ as an Electron Acceptor.	155
3.1.3 MV ²⁺ in Dendrimers.	157
3.2 Experimental Details.	
3.2.1 Materials.	160
3.2.2 Synthesis.	160
3.2.3 Instrumentation and Methods.	164
3.3 Results.	
3.3.1 Absorbance Spectra.	165
3.3.2 Laser Flash Photolysis.	167
3.4 Discussion.	
3.4.1 Spectroscopy of BB _n V ⁶⁺ and NB _n V ⁶⁺ .	
3.4.1.1 Laser Flash Photolysis of BB ₂ V ⁶⁺ and NB _n V ⁶⁺ in CH ₃ CN.	172
3.4.1.2 UV-Visible Spectroscopy and Laser Flash Photolysis of BB ₀ V ⁶⁺ in CH ₃ CN.	174
3.4.2 Charge Trapping in a tris-Methyl Viologen Acceptor Core.	
3.4.2.1 Long-Lived Transient Absorption of MV ^{•+} Cation Radical at 590 nm.	176
3.4.2.2 Biphasic Transient Absorption Kinetics at 400 nm.	178
3.4.2.3 Electron Transfer in BB _n V ⁶⁺ and NB _n V ⁶⁺ .	180
3.4.2.4 The Energy Gap Law in Electron Transfer in BB ₀ V ⁶⁺ .	183
3.4.3 Emission in NB _n V ⁶⁺ Dendrimers.	188
3.5 Conclusions and Future Work.	192
3.6 References.	191

Appendix A. Quantum Mechanical Description of Transitions Between States.

A.1	The Schrödinger Equation.	196
A.2	Born-Oppenheimer Approximation.	197
A.3	Adiabatic Approximation.	198
A.4	Formation and Relaxation of Excited States by Radiative Processes.	
A.4.1	Absorption of a Photon.	200
A.4.2	Spontaneous and Stimulated Emission of a Photon From an Excited State.	200
A.5	References.	203

Appendix B. Supplemental Data.

B.1	Transient absorption decay traces from 365 – 510 nm and 520 - 650 nm upon 355 nm excitation of RuD0 in CH ₃ CN solution at 298 K (450 ns timescale, 5 nm increments, 2.325 nm slit width).	204
B.2	Transient absorption decay traces from 400 – 690 nm upon 355 nm excitation of RuD0 in a glass-supported PMMA film at 298 K (9.0 μ s timescale, 10 nm increments, 2.325 nm slit width).	233

List of Tables

Table 2.1	Absorbance data for Gn-bpy in CHCl_3 and CH_2Cl_2 .	78
Table 2.2	Absorbance data for RuDn in CH_2Cl_2 , CHCl_3 , CH_3CN , and PMMA.	81
Table 2.3	Luminescence data for Gn-bpy in CHCl_3 , CH_2Cl_2 and 4:5 (v/v) <i>n</i> -PrCN/EtCN.	86
Table 2.4	Luminescence data for RuDn in CH_2Cl_2 , CH_3CN and PMMA.	93
Table 2.5	Emission spectral fitting parameters, Franck-Condon factors and reorganization energies for $[\text{Ru}(\text{bpy})_3](\text{PF}_6)_2$ in CH_3CN and PMMA, and RuDn ($n = 0-2$) in CH_3CN ($(298 \pm 3) \text{ K}$).	94
Table 2.6	Summary of luminescence decay data from biexponential and WWK fits of RuDn in several solvents.	98
Table 2.7	Spectral characteristics of peaks determined from Gaussian deconvolution of the absorbance spectrum of RuD0 in CH_3CN .	112
Table 3.1	Absorbance data of BBnV⁶⁺ ($n = 0, 2$) and NBnV⁶⁺ ($n = 0 - 2$) in CH_3CN .	165
Table 3.2	Transient absorption decay lifetimes ¹ for BBnV⁶⁺ and NBnV⁶⁺ dendrimers.	167

List of Figures

- Figure 1.1** Depiction of vertical transitions between potential energy surfaces in accordance with the Franck-Condon principle. Note the lack of wavefunction overlap between the $v' = 0$ and $v'' = 0$ levels, preventing a direct transition between these states. 4
- Figure 1.2** Radiative (k_r) and non-radiative (k_{nr}) transitions of an excited singlet state S_1 , formed by absorption of a photon $h\nu$ by the ground state GS. k_{IC} and k_{ISC} are non-radiative spin-allowed and spin-forbidden transitions respectively; ($k_r + k_{nr}$) is the observed rate of decay of an excited state. 7
- Figure 1.3** Illustration of the interaction of potential energy surfaces in the weak (left) and strong (right) coupling limits (see text), where the increased horizontal displacement ΔQ of the excited state PE surface in the strong coupling limit yields a marked increase in the reorganization energy (λ) and the total energy of excitation (E_{sp}) relative to the weak coupling limit. 12
- Figure 1.4** Comparison of the distance dependence of dipole-dipole (Förster) and exchange (Dexter) mechanisms for energy transfer. 19
- Figure 1.5** Illustration of the energetics of $E_L T$, where λ is the reorganization energy and represents the vertical transition to an excited state; ΔG^0 is the difference in Gibbs energy between the reactants and products; H_{AB} is the electronic coupling of initial and final states; and D, L and A signify donor, link (i.e. bridge) and acceptor, respectively. 20
- Figure 1.6** Illustration of adiabatic vs. nonadiabatic potential energy surface crossings. 21
- Figure 1.7** Experimental confirmation of the Marcus inverted region in the intramolecular electron transfer reaction of the 4-biphenyl ion to a series of acceptors with similar reorganization energies. 24
- Figure 1.8** Evolution of polymeric structures, from (i) linear chains to (ii) hyperbranched macromolecules to (iii) dendrimers. 27

Figure 1.9	Illustration of the general structure of a dendrimer.	29
Figure 1.10	Demonstration of how the properties of large sterically-crowded dendrimers are driven by their surface groups.	31
Figure 1.11	Representation of the convergent and divergent synthetic methods.	32
Figure 1.12	A selection of monomers that have been used in the preparation of Fréchet-type poly(aryl ether) dendrimers.	37
Figure 1.13	Example of a poly(phenylenevinylene) dendrimer.	38
Figure 1.14	Potential energy surfaces of the S_0 and S_1 states of stilbene.	39
Figure 1.15	Overview of the potential fates of excited states of stilbene.	41
Figure 1.16	Comparison of the "hula twist" (HT) to the "one-bond flip" (OBF) olefinic isomerization mechanism.	42
Figure 2.1	Structure of $[\text{Ru}(\text{bpy})_3]^{2+}$.	51
Figure 2.2	Summary of relevant species and molecular quantities associated with energy and electron transfer processes of $[\text{Ru}(\text{bpy})_3]^{2+*}$ relative to the ground state.	52
Figure 2.3	Jabloński diagram of $[\text{Ru}(\text{bpy})_3]^{2+}$ at room temperature.	53
Figure 2.4	Absorbance and corrected luminescence spectra ($\lambda_{\text{exc}} = 446 \text{ nm}$) of $[\text{Ru}(\text{bpy})_3]^{2+}$ in CH_3CN ($(298 \pm 3) \text{ K}$, 1 atm N_2).	54
Figure 2.5	Illustration of the potential energy surfaces of the major metal-centred states of $[\text{Ru}(\text{bpy})_3]^{2+}$.	56
Figure 2.6	Use of increasingly long oligo- <i>p</i> -phenylenevinylene (OPV) bridges to separate a tetracene (TET) electron donor from a pyromellitimide (PI) electron acceptor.	58

Figure 2.7	Structures of the ligands used in Damrauer's study. Three types of spacer were used ($R_1=R_2=H$, $R_1=R_2=CH_3$, $R_1=H$ and $R_2=CH_3$) to alter the degree of steric inhibition of planarization of the MV and bpy groups.	59
Figure 2.8	Conformational gating in an intramolecular donor-acceptor pair: charge trapping by using sterics to attenuate back-electron transfer.	60
Figure 2.9	Syntheses of G0-bpy and RuD0.	63
Figure 2.10	Syntheses of G1-bpy and RuD1.	64
Figure 2.11	Syntheses of G2-bpy and RuD2.	65
Figure 2.12	Syntheses of G3-bpy and RuD3.	66
Figure 2.13	Illustration of 90° excitation of samples in solution and 60° excitation of samples in Pyrex-supported films. Excitation of films was through the backside of the support to minimize scattering of the excitation source towards the detector.	68
Figure 2.14	Absorbance of G <i>n</i> -bpy ($n = 0 - 3$) in $CHCl_3$ ((298 ± 3) K, 1 atm N_2). Spectra were normalized relative to their wavelength of maximum absorbance.	77
Figure 2.15	Absorption spectra of RuD0 - RuD2 in CH_3CN ((298 ± 3) K, 1 atm N_2). Spectra were normalized relative to their wavelength of maximum absorbance.	79
Figure 2.16	Absorbance spectra of RuD0 in $CHCl_3$ and CH_3CN ((298 ± 3) K, 1 atm N_2). Spectra were normalized relative to their wavelength of maximum absorbance.	80
Figure 2.17	Absorbance spectra of RuD <i>n</i> ($n = 0 - 3$) in PMMA ((298 ± 3) K, 1 atm N_2). Spectra were normalized relative to the maximum of the 3MLCT peak at ~ 465 nm.	81
Figure 2.18	Comparison of absorbance spectra of G0-bpy in CH_3CN and $CHCl_3$ ((298 ± 3) K, 1 atm N_2). The transition at ~ 375 nm is assigned to <i>cis</i> -G0-bpy.	82

- Figure 2.19 Changes in absorption of G0-bpy in CHCl₃ upon extended photolysis ($\lambda_{exc} = 355$ nm) using an Nd:YAG laser source ((298 ± 3) K, 1 atm N₂). (In decreasing order at 325 nm: G0-bpy in CHCl₃; 1, 2, 6, 17 and 27 laser shots.) 83
- Figure 2.20 Absorption spectra of G3-bpy in CHCl₃ ((298 ± 3) K, 1 atm N₂). **Black line:** Fresh solution. **Red line:** Spectrum following prolonged 322 nm excitations. **Blue line:** After storage for 24 hours in the dark. 84
- Figure 2.21 Normalized and corrected fluorescence spectra of the G n -bpy ($n = 0 - 3$) dendrimers in CHCl₃ ((298 ± 3) K, 1 atm N₂). 86
- Figure 2.22 Luminescence decay of G0-bpy in CH₂Cl₂ upon sustained 363 nm irradiation ((298 ± 3) K, 1 atm N₂). ($\tau_1 \sim 15$ s, $\tau_2 \sim 1$ hr). 87
- Figure 2.23 Phosphorescence spectra of: (dashed) G1-bpy, (dotted) G2-bpy and (solid) G3-bpy in 10% EtI in 4:5 (v/v) n -PrCN/EtCN at 77 K ($\lambda_{exc} = 320$ nm). Figure provided by Dr. Tarek Ghaddar at AUB. 88
- Figure 2.24 Corrected luminescence spectra of RuD n ($n = 0 - 2$) in CH₃CN upon excitation of λ_{max}^{abs} of the $[(d\pi)^6] \rightarrow {}^1[(d\pi)^5(\pi^*)^1]$ absorbance bands (see Table 2.2) ((298 ± 3) K, 1 atm N₂). 89
- Figure 2.25 Corrected luminescence spectra of RuD0 in CHCl₃ upon 290, 340 and 465 nm excitations ((298 ± 3) K, 1 atm N₂). The break in the spectrum from $\lambda_{em} = 660 - 700$ nm is due to the second harmonic of the excitation light ($\lambda_{exc} = 340$ nm). 90
- Figure 2.26 Steady state luminescence of G1-bpy and RuD1 in CH₂Cl₂ upon 320 nm excitation. RuD1 (solid) emission magnified 10x relative to G1-bpy (dotted). Inset: Relative luminescence intensity of RuD1 in CH₂Cl₂ upon 320 nm (dotted) and 470 nm (solid) excitation. Figure provided by Dr. Tarek Ghaddar at AUB. 91
- Figure 2.27 Corrected luminescence spectra of RuD n ($n = 1 - 3$) in PMMA upon excitation of λ_{max}^{abs} of the $[(d\pi)^6] \rightarrow {}^1[(d\pi)^5(\pi^*)^1]$ absorbance bands (see Table 2.2) ((298 ± 3) K, 1 atm N₂). 92

Figure 2.28	(top) Residual data from the initial fitting procedure. (bottom) Comparison of spectral fitting results of RuD0 in CH ₃ CN before and after spectral subtraction (procedure described in text).	96
Figure 2.29	(top) Luminescence decay of RuD0 in CH ₃ CN (0-1000 ns timescale). Inset: Luminescence decay from 40-200 ns for emphasis of risetime ($\tau = (11 \pm 2)$ ns). (bottom) Luminescence decay of RuD n ($n = 0 - 2$) in CH ₃ CN. All spectra acquired at (298 ± 3) K under 1 atm N ₂ .	99
Figure 2.30	Luminescence decay of RuD0 in 4:1 (v/v) EtOH/MeOH at 655 nm upon 446 nm excitation at 77 K under 1 atm N ₂ .	100
Figure 2.31	Luminescence decay of RuD n ($n = 0 - 3$) in PMMA at 640 nm ($\lambda_{exc} = 446$ nm) ((298 ± 3) K, 1 atm N ₂).	101
Figure 2.32	Transient absorption decay trace of RuD0 in CH ₃ CN at 385 nm ($\lambda_{exc} = 355$ nm) ((298 ± 3) K, 1 atm N ₂).	102
Figure 2.33	3D (top) and 2D (bottom) transient absorption spectra of RuD0 in CH ₃ CN ($\lambda_{exc} = 355$ nm) ((298 ± 3) K, 1 atm N ₂).	103
Figure 2.34	Transient absorption decay trace of RuD0 in PMMA at 400 nm ($\lambda_{exc} = 355$ nm) ((298 ± 3) K, 1 atm N ₂).	105
Figure 2.35	3D (top) and 2D (bottom) transient absorption spectra of RuD0 in PMMA ($\lambda_{exc} = 355$ nm) ((298 ± 3) K, 1 atm N ₂).	106
Figure 2.36	Isomerization of G3-bpy in CHCl ₃ upon prolonged irradiation ($\lambda_{exc} = 322$ nm) as evidenced by changes in the corrected fluorescence spectra acquired periodically during the irradiation ((298 ± 3) K, 1 atm N ₂).	110
Figure 2.37	Illustration of branching ratios from along the S ₁ and S ₀ potential energy surfaces of stilbene.	110
Figure 2.38	Gaussian deconvolution of the absorbance spectrum of RuD0 in CH ₃ CN (red line shows cumulative fit from individual peaks).	112

Figure 2.39	Normalized absorbance of G0-bpy and RuD0 in CHCl ₃ and CH ₃ CN ((298 ± 3) K, 1 atm N ₂).	113
Figure 2.40	Proposed 3-step kinetic model (the “dual emission model”) for global analysis of laser flash photolysis data acquired for RuD0 in CH ₃ CN.	122
Figure 2.41	Proposed 2-step kinetic model (the “conformational dynamics model”) for global analysis of laser flash photolysis data acquired for RuD0 in CH ₃ CN.	124
Figure 2.42	Concentration profiles of ³ MLCT _{bpy} (A, blue), ³ MLCT _L (B, green), and ground states of RuD0 in CH ₃ CN as determined from global analysis of laser flash photolysis data.	125
Figure 2.43	Illustration of the lack of cross-conjugation in RuD0 (top) relative to RuD1 (bottom), where cross-linked sites are denoted by red arrows.	130
Figure 2.44	Illustration of the effect of small S_M and $\Delta\bar{\nu}_{1/2}$ values on ³ MLCT potential energy surfaces. Note the higher energy of the point of intersection between ³ MLCT _{bpy} and ³ MLCT _L (red) versus a more typical ³ MLCT PE surface (pale red), inhibiting ILCT without changing the driving force for this reaction.	134
Figure 2.45	Structures of dmb and vbpy ligands from references 46 and 91.	136
Figure 2.46	Summary of excited state dynamics of the RuD _n dendrimers, demonstrating the interplay of conformational dynamics and ILCT. See text for details.	139
Figure 3.1	Structure of methyl viologen.	154
Figure 3.2	Kinetic schemes describing (a) E _N T and (b) E _L T in a Ru ^{II} polypyridyl-derivatized polymer, wherein both processes involve electron transfer to a MV ²⁺ acceptor.	156
Figure 3.3	NBV3 ²⁺ : an example of a 3 rd generation, Fréchet-type MV ²⁺ -cored dendrimer with naphthalene capping groups.	158

- Figure 3.4 (left) Transient absorption decay of NB3V^{2+} in CH_2Cl_2 at 600 nm following 266 nm excitation. The increase in ΔA from a - d corresponds to increasing laser power intensities (270 μJ , 520 μJ , 765 μJ , and 1.3 mJ, respectively.) (right) Plot of ΔA vs. laser power for NB3V^{2+} at 600 nm, taken after 10 ns and 20 ns. 159
- Figure 3.5 Synthesis of the tris(methyl viologen) core (1) and of the dendron arms for dendrimer generations 0 - 3 (structures 2 -5). 161
- Figure 3.6 Synthesis of $\text{BB}n\text{V}^{6+}$ and $\text{NB}n\text{V}^{6+}$ ($n = 0 - 2$). 162
- Figure 3.7 Synthesis of BB3V^{6+} and NB3V^{6+} . 163
- Figure 3.8 UV-Visible absorbance spectra of $\text{BB}n\text{V}^{6+}$ ($n = 0, 2$) (top) and $\text{NB}n\text{V}^{6+}$ ($n = 0 - 2$) (bottom) in CH_3CN at (298 ± 3) K. Spectra were normalized to the maximum absorbance of the MV^{2+} -based band centred at ~ 260 nm. 166
- Figure 3.9 Transient absorption decay of $\text{NB}n\text{V}^{6+}$ in CH_3CN at 400 nm (top) and 590 nm (bottom) upon 266 nm collinear excitation at (298 ± 3) K. 169
- Figure 3.10 Transient absorption decay of BB0V^{6+} and BB2V^{6+} in CH_3CN at 400 nm (top) and 590 nm (bottom) upon 266 nm collinear excitation ((298 ± 3) K, 1 atm N_2). 170
- Figure 3.11 Laser flash photolysis of NB1V^{6+} in CH_3CN at 400 nm upon 266 nm collinear excitation at (298 ± 3) K. 171
- Figure 3.12 Laser flash photolysis of BB2V^{6+} and $\text{NB}n\text{V}^{6+}$ ($n = 0 - 2$) in CH_3CN at 400 nm (top) and 590 nm (bottom) upon 266 nm collinear excitation at (298 ± 3) K. 173
- Figure 3.13 Absorbance spectra of BB0V^{6+} in CH_3CN following a single 266 nm excitation pulse ((298 ± 3) K, 1 atm N_2). Spectra were acquired periodically over 10 minutes in the order 1-8. (Inset: Baseline magnified to show spectral changes with time.) 176

- Figure 3.14** Hole migration *via* sequential E_LT processes upon photoexcitation of the tris(methyl viologen) core in NB2V⁶⁺ (remainder of structure omitted for the sake of clarity). Hole quenching side reactions are not shown but are possible from all BnO[•] and Np[•] states. 182
- Figure 3.15** UV-Vis spectra of NB1V⁶⁺ in low quality (top) and high quality (bottom) CH₃CN following 266 nm excitation at (298 ± 3) K. 185
- Figure 3.16** Illustration of potential energy surfaces corresponding to possible reaction pathways of the BB_nV⁶⁺ and NB_nV⁶⁺ dendrimers. (a) The [Ph[•]/MV^{••}] charge-separated state lies in the inverted region, attenuating the rate of relaxation by charge recombination. The [BnO[•]/MV^{••}] and [Np[•]/MV^{••}] PE surfaces are not as nested and can easily undergo exchange with each other. (b) Deprived of a facile back-reaction pathway, the [Ph[•]/MV^{••}] state is quenched intermolecularly. 187
- Figure 3.17** Electron transfer pathway and naphthalene cation radical dimer formation in NB1V⁶⁺ (majority of structure omitted for simplicity). 191

List of Symbols and Abbreviations

Chapter 1

$\lambda_{I \rightarrow F}$	probability of a transition between initial and final states
$M_{I \rightarrow F}$	matrix element for coupling of two states
ρ_F	density of final acceptor states
\hbar	Planck's constant/ 2π
h	Planck's constant
Ψ	wavefunction
$k_{I \rightarrow F}$	rate constant for a transition between initial and final states
\hat{H}	Hamiltonian operator
\vec{r}, \vec{R}	coordinate vectors
E	energy
χ_v	vibrational nuclear wavefunction
ψ	electronic wavefunction
ψ_{el}, ψ_s	electronic, spin wavefunctions
k_{max}^0	maximum possible rate constant for a transition
f_{el}, f_s, f_v	electronic, spin and vibrational prohibition factors
$h\nu$	energy of a photon
v	energy level
q	nuclear coordinate
k_{ic}	rate constant for internal conversion
k_{isc}	rate constant for intersystem crossing
k_r / k_{nr}	rate constant for radiative/nonradiative decay
R	rate
A	Einstein coefficient of emission

B	Einstein coefficient of absorption
ΔE	difference in energy between initial and final states
τ	lifetime
ϕ	quantum yield
ν	quantum number
Q	internal coordinate for a normal vibrational mode k
C_{nn}^k	electronic coupling matrix
ω_k	vibrational angular frequency
S	Huang-Rhys factor
\bar{n}_l	average number of excited vibrations for a mode l
M	reduced mass
λ	reorganization energy
ΔG°	difference in Gibbs energy between final and initial states
$E_L T / E_N T$	electron transfer/energy transfer
HOMO/LUMO	highest occupied/lowest unoccupied molecular orbital
D/A	donor/acceptor
$\bar{\mu}$	dipole moment
R_{D-A}	donor/acceptor distance of separation
n	refractive index of a solvent
κ	dipole orientation factor
L	sum of the average Bohr radii for the donor and acceptor
Y	overlap cancellation factor
K	orbital interaction coefficient
J	spectral overlap integral
I	emission intensity
H_{AB}	donor/acceptor electronic coupling factor
ν_N	collisional/vibrational frequency of interaction between states

κ	normalized electronic transmission coefficient
ΔG^\ddagger	Gibbs energy of activation at the transition state
R	gas constant
d^p	equilibrium bond distance
a	radius
r	distance of radial separation
D_{op}/D_s	optical/static dielectric constant of a solvent
ν_e	effective nuclear frequency
$\kappa_{E,T}$	electronic factor
Γ_λ	nuclear tunneling factor
ps	picosecond
DHP	dihydrophenanthrene
M_w	molecular weight

Chapter 2

$[\text{Ru}(\text{bpy})_3]^{2+}$	ruthenium (II) tris-2,2'-bipyridine ion
bpy	2,2'-bipyridine
ISC	intersystem crossing
λ	wavelength
nm	nanometer
M	molarity
CH_3CN	acetonitrile (methyl cyanide)
LC	ligand centred
MLCT	metal-to-ligand charge transfer
fs	femtosecond
cm^{-1}	wavenumber

K	Kelvin
°C	degrees Celsius
LF	ligand field
μs	microsecond
MV, MV ²⁺	methyl viologen (1,1'-dimethyl-4,4'-bipyridinium ion)
PF ₆ ⁻	hexafluorophosphate ion
mV	millivolt
DFT	density functional theory
ILCT	interligand charge transfer
UV	ultraviolet
EtOH	ethanol
<i>n</i> -PrCN	butyronitrile (<i>n</i> -propyl cyanide)
EtCN	propionitrile (ethyl cyanide)
GC	gas chromatography
MeOH	methanol
CH ₂ Cl ₂	methylene chloride
CHCl ₃	chloroform
PMMA	poly(methyl methacrylate)
GPC	gel permeation chromatography
<i>t</i> -BuOK	potassium <i>t</i> -butoxide
THF	tetrahydrofuran
NH ₄ PF ₆	ammonium hexafluorophosphate
W	watt
PMT	photomultiplier tube
UV-Vis	UV-Visible
s	second
mM	millimolar
Hz	Hertz

IRF	instrument response function
Nd:YAG	neodymium-doped ytterbium aluminum garnet
fwhm	full width at half maximum
MHz	megahertz
bar	bar (unit of pressure)
$I(\bar{\nu})$	intensity of emission at energy $\bar{\nu}$
β	stretching exponent
$\langle \tau \rangle$	average lifetime of a heterogeneous distribution
ν_M	vibrational quantum number
$\hbar\omega_M$	quantum spacing of averaged coupled vibrational modes of medium frequency
$\Delta\bar{\nu}_{0,1/2}$	full width for individual vibronic lines at half-maximum height
NMR	nuclear magnetic resonance
MALDI-TOF	matrix-assisted laser desorption/ionization time-of-flight spectrometry
mg	milligram
mL	millilitre
NIR	near-infrared
atm	atmosphere
EtI	ethyl iodide
hr	hour
$F(\text{calc})$	Franck-Condon factor
ΔA	change in absorbance
LFP	laser flash photolysis
TA	transient absorption
k_B	Boltzmann constant
ns	nanosecond

\bar{M}	transition moment
IL	interligand

Chapter 3

MV ^{•+}	methyl viologen cation radical
eV	electronvolt
IP	ionization potential
PTZ	phenothiazine
μJ	microjoule
mJ	millijoule
V	volt
4,4'-bpy	4,4'-bipyridine
K ₂ CO ₃	potassium carbonate
CBr ₄	carbon tetrabromide
PPh ₃	triphenylphosphine
B	bridge
Ph	phenyl
Np	naphthyl
BnO	1,3-bis(methyleneoxy)benzene
Q	quencher
Np ₂ ^{•+}	naphthalene dimer cation radical

Appendix A

\hat{T}	kinetic energy operator
V	potential energy
\hat{p}	momentum
m	mass
∇	gradient vector (nabla)
Z	nuclear charge
e	charge of an electron

Chapter 1. Introduction.

The purpose of this Section is to introduce some of the theory and background that is important to the understanding and discussion of the research presented in this Dissertation. Topics such as the origin and implications of Energy Gap Law for non-radiative decay, the basic principles of energy and electron transfer, the origin of the Marcus inverted region and the physical and photochemical properties of poly(phenylenevinylene) and poly(aryl ether) (i.e. Fréchet-type) dendrimers are addressed in some depth. Some basic principles of photophysics that underpin the theory described in Section 1.1 can be found in Appendix A.

1.1 Fermi Golden Rule.

For situations where the probability of a transition between initial and final states is constant in time, this probability $\lambda_{I \rightarrow F}$ is dependent on the magnitude of coupling between initial and final states (expressed as the matrix element for interaction, $M_{I \rightarrow F}$) and on the number of pathways through which the transition can occur (which is effectively the same as the density of final acceptor states, ρ_F),

$$\lambda_{I \rightarrow F} = \frac{2\pi}{\hbar} |M_{I \rightarrow F}|^2 \rho_F \quad [1.1]$$

where $\hbar = h / 2\pi$, and $h =$ Planck's constant. Alternately, this equation can be restated in terms of wavefunctions Ψ , wherein the causative interaction for the transition is treated as a potential \hat{V} that operates on the initial state, taken over all space:

$$M_{I \rightarrow F} = \int \Psi_F^* \hat{V} \Psi_I dV \quad [1.2]$$

Noting that the probability $\lambda_{I \rightarrow F}$ is related to the rate constant of a transition, [1.1] can be expressed in terms of the rate constant $k_{I \rightarrow F}$ for a transition between states described by these two wavefunctions, whereby the initiator of the transition (previously the potential operator \hat{V}) is expressed by the Hamiltonian operator $\hat{H}_{I \rightarrow F}$ in equation [1.3]:

$$k_{I \rightarrow F} = \langle \Psi_F | \hat{H}_{I \rightarrow F} | \Psi_I \rangle^2 \rho_F \quad [1.3]$$

These equations are all alternate expressions of the *Fermi Golden Rule*,^{1,2} which is the result of subjecting a time-independent wavefunction to a time-dependent Hamiltonian, a treatment that is known as time-dependent perturbation theory. Substituting the fully-separated wavefunction [1.4] (see **Appendix A** for a derivation of this expression)

$$\Psi(\vec{r}, \vec{R}) = \Psi_e(\vec{r}, \vec{R}) \chi_e(\vec{R}) = \psi_{el}(\vec{r}, \vec{R}) \psi_r(\vec{r}, \vec{R}) \chi_e(\vec{R}) \quad [1.4]$$

into the latter result [1.3] yields an expression relating the probability of a transition to the product of three separate matrix elements,

$$\begin{aligned}
k_{I \rightarrow F} &= \langle \Psi_F | \hat{H}_{I \rightarrow F} | \Psi_I \rangle^2 \rho_F = [\langle \Psi_F | \Psi_I \rangle E_{I \rightarrow F}]^2 \rho_F \\
&= [\rho_F E_{I \rightarrow F}^2] \langle \Psi_F | \Psi_I \rangle^2 \\
&= [\rho_F E_{I \rightarrow F}^2] \langle \psi_{el,F} | \psi_{el,I} \rangle^2 \langle \psi_{v,F} | \psi_{v,I} \rangle^2 \langle \chi_{v,F} | \chi_{v,I} \rangle^2 \\
&= k_{\max}^0 [f_{el} \times f_s \times f_v]
\end{aligned}
\tag{1.5}$$

where the matrix elements $f_{el} = \langle \psi_{el,F} | \psi_{el,I} \rangle$, $f_s = \langle \psi_{v,F} | \psi_{v,I} \rangle$, and $f_v = \langle \chi_{v,F} | \chi_{v,I} \rangle$ are the electronic spatial (orbital), spin selection, and vibrational overlap integrals, respectively. These terms are defined as the prohibition factors for a transition between weakly interacting states, which describe the effect of changes in the orbital, spin, and vibrational configurations in the transition from initial to final states, relative to the maximum possible rate constant for the transition, k_{\max}^0 ; thus, these prohibition factors are less than or equal to one.^{1,2}

1.2 Franck-Condon Principle.

Given that the Fermi Golden Rule describes the probability of a transition as being dependent upon the degree of coupling between initial and final states, there must therefore exist some degree of overlap of all three pairs of wavefunctions in both the initial and final states for the transition to occur (in other words, $\langle \psi_F | \psi_I \rangle \neq 0$). A key ramification of this requirement is that the initial and final vibrational wavefunctions - which correspond to the configuration and nature of the nuclei of the molecule - must overlap, and the greater the degree of overlap the greater the probability that the transition will take place; this is a description of what is known as the *Franck-Condon*

principle (Figure 1.1).^{1,2} The vibrational prohibition factor (also known as the Franck-Condon factor) acts as a selection rule for allowed vibrational transitions and is thus of great importance in spectroscopy, as it provides an explanation for the observed intensities of these transitions. In particular, this principle states that the so-called “vertical” transition between potential energy surfaces is the most probable, demonstrating that the nuclear coordinates are largely static on the timescale of electronic transitions.

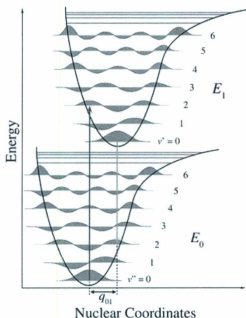


Figure 1.1 Depiction of vertical transitions between potential energy surfaces in accordance with the Franck-Condon principle. Note the lack of wavefunction overlap between the $v' = 0$ and $v'' = 0$ levels, preventing a direct transition between these states.³

1.3 Radiative and Non-Radiative Transitions of Excited States.

1.3.1 Radiative Transitions.

In the absence of conditions that are conducive to excited state depletion by stimulated emission, the rate of radiative decay of a molecule from the excited state (ES) to an excited vibrational level of the ground state (GS) is dependent on the Einstein coefficient of emission, A_{21} :

$$R_{spE} = N_2 A_{21} \quad [1.6]$$

$$k_r = \frac{1}{\tau_r} = A_{21} \quad [1.7]$$

where equation [1.6] is the equation of spontaneous emission [A.13] and A_{21} is as delineated by [A.15] from Appendix A; k_r is the rate constant for spontaneous emission; and τ_r is the lifetime of the excited state. Equation [1.7] describes the rate at which this process takes place, but as it can only address the states that spontaneously emit it offers little insight into how many or few excited states relax by this mechanism. It could, for example, be useful to know what fraction of the absorbed photons are re-emitted by a molecule. Thus, the *quantum yield* ϕ for emission is defined as

$$\phi = \frac{k_r}{k_r + k_{nr}} \quad [1.8]$$

where k_{nr} is the rate constant of non-radiative decay, a process which is addressed in the next Section. Combining the latter two equations, it can be seen that

$$k_r = \frac{\phi}{\tau}; k_{nr} = \frac{(1-\phi)}{\tau} \quad [1.9]$$

$$k_{\text{obs}} = \frac{1}{k_r + k_{nr}} = \tau \quad [1.10]$$

where [1.10] yields τ , the experimentally-observed excited state lifetime.⁴

1.3.2 Non-Radiative Transitions.

Equation [1.10] demonstrates that the longevity of an excited state, which is often determined by measurement and quantification of radiative processes, is inextricably tied to concurrent non-radiative relaxation pathways as well (Figure 1.2). These radiationless transitions can be conceptualized as molecular energy disposal processes that allow these excited states to relax back to a vibrationally-excited state of the ground state. This is most commonly achieved by vibrational cooling, caused by the coupling of wavefunctions of donor states in the molecule with appropriate acceptor states in the surrounding medium, causing mixing of the otherwise orthogonal Born-Oppenheimer adiabatic states. This mechanism is favoured in condensed phases where there are countless appropriate acceptor states available to the molecule, enabling dissipation of the excess energy into vibrational states involving large molecules that experience only weak interactions with solvent (such as certain situations where the molecules in question are embedded in a rigid matrix), there is little opportunity for non-radiative decay by dumping excess energy into this large heat sink. Rather than depending on the environment to act as a heat bath, some molecules can exploit acceptor vibrational modes within their own structure to spread and dissipate this excess energy.

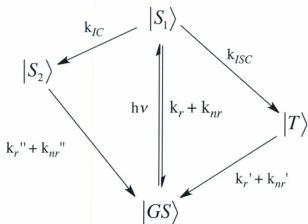


Figure 1.2 Radiative (k_r) and non-radiative (k_{nr}) transitions of an excited singlet state S_1 , formed by absorption of a photon $h\nu$ by the ground state GS . k_{IC} and k_{ISC} are non-radiative spin-allowed and spin-forbidden transitions to singlet states S_2 and triplet states T , respectively; $(k_r + k_{nr})$ is the observed rate of decay of an excited state.

Alternately, there are pathways through which a molecule does not dispose of energy by vibrational cooling, and instead uses this excited state energy to induce a transition to another electronic state of lower energy. The coupling of wavefunctions for two states of the same spin or of opposite spin gives rise to two different types of transitions; namely, *internal conversion* (IC) and *intersystem crossing* (ISC), respectively. Transitions between states of opposite spin are typically disallowed processes, and it is only by the mixing of spin states induced by spin-orbit coupling that these transitions are permitted.²

1.3.2.1 Total Rate of Non-Radiative Decay.

The development of the theory of non-radiative decay by Lin, Freed, and Jortner^{4,11} considered not just the transition of one predominant donating excited vibronic state to one predominant accepting vibronic level of the ground state, but rather sought to devise a more inclusive description of non-radiative decay by including a summation of contributions from all available donor and acceptor vibronic states. To reach this formulation of radiationless decay, the ground and excited states must first be defined according to equations [1.11] and [1.12], respectively:

$$\text{Ground state} = \Psi_m \prod_{k=1}^{3N-6} \chi_v^m(Q_k) \quad [1.11]$$

$$\text{Excited state} = \Psi_n \prod_{k=1}^{3N-6} \chi_v^n(Q_k) \quad [1.12]$$

where Ψ and $\chi_v(Q_k)$ represent the electronic and vibrational wavefunctions of quantum number v , respectively; Q_k is the internal coordinate for the normal mode k , and m and n represent ground and excited states. From this point the development is predicated on the assumptions that transitions arise from a Boltzmann distribution of vibrational levels and that vibrational relaxation is more rapid than electronic relaxation; this requires that the excited state be in equilibrium with its solvent environment. Incorporating these terms into the Fermi Golden Rule yields equation [1.13]:

$$k_{nr} = \frac{2\pi}{\hbar} \left[\left\langle \Psi_n \prod_k \chi_v^n(Q_k) \left| \hat{H}' \right| \Psi_m \prod_k \chi_v^m(Q_k) \right\rangle \right]^2 \delta(E_{m'} - E_{m'}) \quad [1.13]$$

Applying the Franck-Condon principle, the dependences of the electronic wavefunctions Ψ upon the nuclear coordinates are ignored, and thus the matrix element of [1.13] is reformulated in terms of an electronic coupling matrix $C_{nm}^{k'}$ (equation [1.14]),⁸

$$k_{nr} = \frac{2\pi}{\hbar} \left[\sum_{k'} C_{nm}^{k'} \langle \chi_v^n(Q_i) | \frac{\delta}{\delta Q_{k'}} | \chi_v^m(Q_i) \rangle \prod_{i \neq k'} \langle \chi_v^n(Q_i) | \chi_v^m(Q_i) \rangle \right]^2 \delta(E_{nv} - E_{mv}) \quad [1.14]$$

where the introduction of the Dirac delta function is necessary for conservation of energy and the electronic coupling element $C_{nm}^{k'}$ is given as equation [1.15],

$$C_{nm}^{k'} = i\hbar \langle \Psi_n | \frac{\delta}{\delta Q_{k'}} | \Psi_m \rangle \quad [1.15]$$

Equations [1.14] and [1.15] introduce the vibrational modes k' as part of the electronic coupling element matrix, and thus they describe vibrational modes that enable mixing between these electronic wavefunctions. Therefore, as this coupling matrix equals zero for those modes k' that do not enable mixing and is non-zero for those that do, these k' modes are known as promoting modes; furthermore, in large systems the superposition of large numbers of closely-spaced vibrational modes lifts the $k \neq k'$ restriction. Equation [1.16] can be greatly simplified by eliminating the summation of coupling matrices by recognizing that the majority of transitions are enabled by one dominant promoting mode, yielding an expression that describes one effective transition from one excited vibronic state to one ground vibronic state. For a complete determination of the rate of non-radiative decay this assessment must be expanded to consider transitions between all available vibrational levels of both the excited and ground states, and then weighting

them according to the Boltzmann population $p(nv')$ of the excited states (thereby incorporating not only the number of potential transitions, but also the likely magnitude of the contribution of each vibronic state to the overall rate at a given temperature).⁴

$$k_{nr} = \frac{2\pi}{\hbar} |C_{mn}^{k'}|^2 \left[\left\langle \chi_{v'}^n(Q_{k'}) \left| \frac{\delta}{\delta Q_{k'}} \right| \chi_{v'}^m(Q_{k'}) \right\rangle \right]^2 \times \prod_k \sum_{v'} p(nv') \langle \chi_{v'}^n(Q_k) | \chi_{v'}^m(Q_k) \rangle^2 \delta(E_{nv'} - E_{mv'}) \quad [1.16]$$

1.3.2.2 Energy Gap Law.

Equation [1.16] is a complete representation of the rate of non-radiative decay. This equation is commonly recast in terms of single predominant promoting and accepting modes k' and k , along with a number of weak lower frequency acceptor modes l to yield the expression [1.17], which is known as the *Energy Gap Law*:¹²

$$k_{nr} = |C_{mn}^{k'}|^2 \omega_{k'} \sqrt{\frac{\pi}{2\hbar\omega_k E_{0k'}}} \exp(-S_k) \times \exp \left[-\frac{\gamma E_{0k'}}{\hbar\omega_k} + \left(\frac{\gamma+1}{\hbar\omega_k} \right)^2 \sum_l \frac{\lambda_l \hbar\omega_l (2\bar{n}_l + 1)}{2} \right] \quad [1.17]$$

In this expression, ω_k and $\omega_{k'}$ are the vibrational angular frequencies of the medium acceptor k and promoting k' modes, $E_{0k'} = E_{00} - \hbar\omega_{k'}$ is the energy gap for where ΔQ_k , the change in the nuclear coordinate for the medium acceptor mode k , is zero. γ is represented by the expression [1.18],

$$\gamma = \ln \left(\frac{E_{0k'}}{S_k \hbar\omega_k} \right) - 1 \quad [1.18]$$

\bar{n}_l is the average number of excited vibrations for the normal mode l ,

$$\bar{n}_l = \frac{1}{\exp\left(\frac{\hbar\omega_l}{k_B T}\right) - 1} \quad [1.19]$$

and S_l is the *Huang-Rhys factor* (equation [1.20]), where M_l is the reduced mass,

$$S_l = \frac{M_l \omega_l}{2\hbar} (\Delta Q_l)^2 \quad [1.20]$$

This formulation of the total rate of radiationless decay (equation [1.17]) is valid in the so-called weak coupling limit, where the energy gap E_{00} (defined as the energy difference between the zeroth vibrational levels of the excited and ground potential energy surfaces) is much larger than the product $\lambda_l = S_l \hbar \omega_l$. λ_l is called the *reorganization energy*¹³ and is briefly described in this context as the amount of energy required to rearrange the geometries of a molecule and of solvent to accommodate the structural and electronic changes caused by photon absorption. By the Franck-Condon principle this reorganization is not instantaneous, and thus this energy is part of the total energy of vertical excitation, representing an energetic barrier to formation of an excited state. In the strong coupling limit (Figure 1.3), the total energy of this transition ($E_{sp} = \Delta G + \lambda_l$) is greater than the difference in Gibbs energy ΔG of the potential energy surfaces, while λ_l (required for reorganization) comprises the balance of the full energy of excitation. This excess energy is consumed by motion of the molecule and solvent as they reorganize themselves to accommodate the new electronic environment of the excited state.¹²

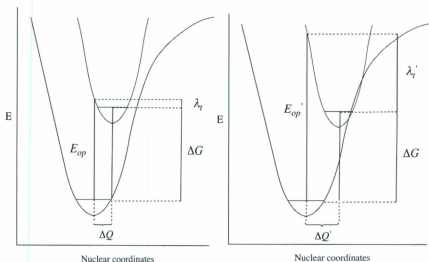


Figure 1.3 Illustration of the interaction of potential energy surfaces in the weak (left) and strong (right) coupling limits (see text), where the increased horizontal displacement ΔQ of the excited state PE surface in the strong coupling limit yields a marked increase in the reorganization energy (λ_γ) and the total energy of excitation (E_{op}) relative to the weak coupling limit.

1.3.2.3 Attenuation of k_{nr} in Nested Potential Energy Surfaces.

The formulation of the total rate of non-radiative decay presented in [1.17] yields a surprising, counterintuitive result: it predicts that, with all other things being equal, as the driving force for non-radiative decay increases (meaning that the excited state potential energy surface lies at higher and higher energies, yielding increasing separation between the $v = 0$ states of excited and ground state PE surfaces) the rate of non-radiative decay decreases. The key to understanding this behavior lies in the Franck-Condon factors for the ground and excited states, as the rate of a transition between states is dependent upon, among other things, the degree of overlap between vibrational states. At increasing values

of ΔG , the overlap (and thus, coupling) between the $n' = 0$ mode of the excited state and an appropriate acceptor mode of the ground state decreases, leading to smaller Franck-Condon factors for the transition, and slower rates as per equation [1.5]. Thus, excited-ground state PE surface pairs with the appropriate combination of large ΔG and small Huang-Rhys factors (the latter of which are dependent on $\langle \Delta Q \rangle^2$) will yield so-called "nested" PE wells with low rates of non-radiative decay.

1.3.2.4 Spin-Orbit Coupling.

The probability that a transition between states that requires a change in electron spin (the two most prominent examples being singlet-triplet and triplet-singlet) will occur is mediated by the spin prohibition factor f_s in the Fermi Golden Rule ([1.5]). This is a reflection of the degree of *spin-orbit coupling* between the electron spin and the electron orbital motion, wherein the interaction between these two parameters causes a "flip" in the spin direction of one of the electrons.² To a first approximation, the spin prohibition factor selects between transitions that are either spin allowed or spin forbidden, as determined by the spin overlap integral $\langle \psi_{s,F} | \psi_{s,I} \rangle$. Due to the orthogonality of these wavefunctions, this integral is identically 1 when there is no change in spin (i.e. spin allowed) and identically 0 otherwise (i.e. spin forbidden). However, due to the motion of electrons about a charged nucleus, perturbations to these wavefunctions can arise which break their strict orthogonality and relax these prohibitory factors. The most prominent of these perturbations arises *via* an interaction of the magnetic moment of an electron's

spin with the orbital angular momentum, which allows for the conservation of magnetic energy of the two states for the spin-flipping transition.² Furthermore, given that the magnitude of a magnetic field (and thus, the magnetic moment) produced by a moving charge is proportional to its velocity, it then follows that the electrons of heavier atoms will yield a larger degree of spin-orbit coupling. This is due to the near-relativistic velocities exhibited by these particles in response to the large electrostatic attraction of the nuclei of heavy atoms.² For this reason, spin-orbit coupling is often a potent effect in larger transition metals as exemplified by the mixed electronic states exhibited by Ru polypyridyl complexes, discussed in **Chapter 2**.

1.4 Energy Transfer ($E_N T$) and Electron Transfer ($E_L T$) Theory.

The formation of an excited state donor D^* by absorption of a photon necessarily leads to the eventual relaxation of this state by disposal of the excess energy, be that by radiative decay, cooling *via* vibrational coupling with solvent, or by methods such as electron or energy transfer from an excited D^* state to an appropriate acceptor A. The main driving force for $E_N T$ or $E_L T$ reactions lies in the ability of a molecule in an excited state to stabilize itself (that is, reduce its energy) by coupling with a different molecule in its ground state. Interactions between half-filled HOMOs and LUMOs of D^* and A, for example, serve to stabilize excited states.² The pathway that leads to quenching of the D^* excited state is determined by a variety of parameters, such as by the degree of coupling between D^* and A states, or by the manner in which these states interact with each other.

1.4.1 An Overview of $E_N T$ Mechanisms.

Energy transfer in molecules can proceed by several mechanisms: (1) trivial $E_N T$, wherein an emitted photon from an excited state D^* is absorbed by an acceptor A ;^{2,14} (2) Förster $E_N T$, a long-range, dipole-dipole donor-acceptor interaction involving singlet states; (3) Dexter $E_N T$, a short-range, singlet-singlet or triplet-triplet quantum mechanical electron exchange mechanism;¹⁵ or (4) quantum-coherent electron $E_N T$, a recently discovered mechanism of $E_N T$ which relies on quantum mechanical resonances (roughly akin to standing waves) between donor and acceptor groups over intermediate (sub-nanosecond) distances.^{16,17} The latter mechanism is discussed here for the sake of completeness, but given that quantum coherency is unlikely to persist for nanoseconds at a time it is not relevant to the observed photodynamics of the dendritic chromophores discussed in this Dissertation.

The trivial $E_N T$ mechanism is rather dissimilar from the other three mechanisms. This process involves an emissive excited state D^* , whereby the photons released by an emissive event are captured by a suitable acceptor A . Because this involves a vertical photophysical transition between potential energy surfaces, this mechanism has been found in molecules with *no* suitable electron exchange or dipole-dipole interactions, as the only requirement for this mechanism to occur is that there must be overlap between the absorption and emission spectra of the two molecules in question.²

Förster^{14,18} energy transfer (also known as dipole-dipole, or Coulombic $E_N T$) involves a resonant interaction between an excited state donor D^* and a ground state acceptor A

through the overlap of their respective dipolar electric fields. The energy of electrostatic interaction of dipoles (equation [1.23]) is classically proportional to (a) the magnitudes of the dipoles $\vec{\mu}_D$ and $\vec{\mu}_A$, and (b) the inverse of the cubed distance of separation between dipoles $R_{D'A}^3$,

$$E \propto \frac{\vec{\mu}_D \cdot \vec{\mu}_A}{R_{D'A}^3} \quad [1.21]$$

This classical relationship can be integrated into a quantum mechanical framework through the Fermi Golden Rule by considering the interaction of the donor and acceptor wavefunctions of both the initial and final states through an appropriate dipole-dipole operator. In this manner it is shown that the rate of Förster E_NT is proportional to the square of the energy of electrostatic interaction, and thus the rate of transfer is inversely proportional to the 6th power of the distance of separation.

The application of the Fermi Golden Rule introduces prohibition factors to the Förster E_NT process, the most important of which (in this case) is the requirement for non-orthogonal spin states; for this reason, Förster transfer is exclusively a singlet-singlet interaction, as triplet dipoles are too weak for E_NT to occur at any appreciable rate.^{2,14} The final derivation of the probability for Förster E_NT is shown in equation [1.22],

$$k_{E_{NT}} = \frac{2\pi}{\hbar} \left[\frac{3\hbar^5 c^4 Q_A}{8\pi^2 R_{D'A}^6 n^4 \tau_D} \right] \int \frac{f_D(E) F_A(E)}{E^4} \delta E \quad [1.22]$$

where n is the refractive index of the solvent; τ_D is the radiative lifetime of D^{*}; Q_A is the integrated area of the absorbance spectrum of A; and $R_{D'A}$ is the donor/acceptor distance

of separation. The latter half of this equation represents the overlap of the Franck-Condon states of donor and acceptor, where $f_{D'}(E)$ and $F_A(E)$ are the normalized emission and absorption spectra, respectively.^{14,15}

Dexter¹⁹ energy transfer, on the other hand, involves the mutual transfer of two electrons *via* their exchange interaction (a quantum mechanical property with no classical analogue) wherein the interconversion of identical particles is an energetically desirable property. The equations that govern this mechanism can be derived in a similar manner as those of the Förster E_NT mechanism, whereby the dipole-dipole interaction operator is replaced by one for electron exchange. The rate of Dexter E_NT can be expressed in a similar form to that seen in equation [1.22] for Förster E_NT; that is,

$$k_{E_N T} = \frac{2\pi}{\hbar} \left[\frac{Y e^4}{\kappa^2 R_{D'A}^2} \exp\left(\frac{-2R_{D'A}}{L}\right) \right] \int \frac{f_{D'}(E) F_A(E)}{E^4} \delta E \quad [1.23]$$

where L is the sum of the average Bohr radii for the donor and acceptor; and Y is a dimensionless quantity that accounts for overlap cancellation as a result of sign changes in the overlapping wave functions.^{15,19} κ is a dipole orientation factor given as

$$\kappa = \cos\phi_{D'A} - 3\cos\phi_{D'} \cdot \cos\phi_A \quad [1.24]$$

Alternatively, the rate of Dexter transfer can be expressed as in equation [1.25],

$$k_{E_N T} = KJ \exp\left(-\frac{2R_{D'A}}{R_{D'A}^0}\right) \quad [1.25]$$

where K is an orbital interaction coefficient; R_{DA}^0 is the "critical" distance of separation, or the sum of the van der Waals radii of D^* and A ; and J is the spectral overlap integral,

$$J = \int_0^{\infty} I_{D'}(\bar{\nu}) \epsilon_A(\bar{\nu}) d\bar{\nu} \quad [1.26]$$

where $I_{D'}(\bar{\nu})$ is the intensity of emission as a function of wavenumber.

Comparing the terms of the rate equations for both of these mechanisms, the most notable differences are that (a) whereas the rate of Dexter $E_N T$ decreases as an exponential of the D^* - A distance of separation, Förster $E_N T$ rates are inversely proportional to the 6th power of the D^* - A distance, owing to the different mechanism of interaction of these two mechanisms (Coulombic vs. orbital overlap); and (b) the Förster mechanism is strongly dependent on the spectral properties of the donor ($\tau_{D'}$) and the acceptor (Q_A) while the Dexter mechanism is not, due to differences in the operators for these two pathways. However, as shown in Figure 1.4, while the Dexter mechanism is the most rapid at short separations, the Förster mechanism does not depend on orbital overlap and therefore is effective at much longer distances; for this reason, Förster transfer is most commonly seen in biological systems while Dexter transfer is typically reserved for smaller molecules.²⁰

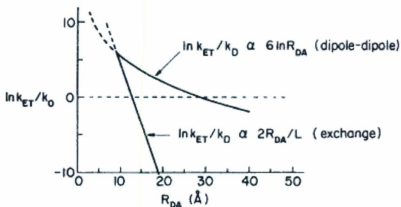


Figure 1.4 Comparison of the distance dependence of dipole-dipole (Förster) and exchange (Dexter) mechanisms for energy transfer.² Reproduced from Modern Molecular Photochemistry of Organic Molecules, by Turro, Ramamurth and Scaiano, (2010) University Science Books. All rights reserved.

1.4.2 E_LT: Marcus Theory.

Marcus' theories of E_LT were largely influenced by the previous work of Libby,^{13,21} who applied Franck-Condon principles to electron transfer reactions in solution,²² noting that the solvent and nuclear coordinates of the ground state were inappropriate for the excited state. However, Marcus reasoned that while Libby's interpretation of the electron transfer process occurring as a vertical transition was valid for photoinitiated E_LT reactions, it was unlikely that the mechanism for a thermally-driven E_LT reaction would require amassing sufficient thermal energy to cause a vertical transition to a separate potential energy surface.^{13,21}

Instead, Marcus reasoned that a thermal transfer would not require a large vertical transfer, but rather small and subtle solvent and geometric perturbations that ensured that thermal equilibrium was maintained at all points along the reaction coordinate, and would thus allow the transfer of an electron from one state to another by a roughly horizontal PE surface crossing (Figure 1.5).¹³ This mechanism considered a wide variety of reaction conditions, ranging from strongly coupled adiabatic E_LT to the non-adiabatic E_LT of weakly-interacting states (Figure 1.6).²¹ Importantly, Marcus incorporated a modification of Libby's theories regarding solvent and geometric reorganizations, recognizing the importance of these parameters in the rates of E_LT reactions.²

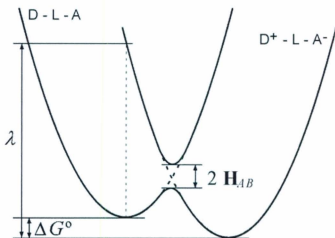


Figure 1.5 Illustration of the energetics of E_LT, where λ is the reorganization energy and represents the vertical transition to an excited state; ΔG° is the difference in Gibbs energy between the reactants and products; H_{AB} is the electronic coupling of initial and final states; and D, L and A signify donor, link (i.e. bridge) and acceptor, respectively.²³

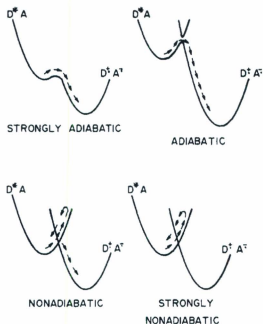


Figure 1.6 Illustration of adiabatic vs. nonadiabatic potential energy surface crossings.²¹ Adapted with permission from Kavarnos, G. J. and Turro, N. J., *Chem. Rev.* 1986, 86, 401. © 1986 American Chemical Society.

Marcus' theory states that the barrier to transfer of an electron is not the vertical transition from one ground state PE to another, but rather the barrier to a horizontal transition along the PE surface that results from the intersection of the PE surfaces of the reactants and products. The small solvent and geometric perturbations cause, when taken together, reorganization of the solvent/nuclear coordinates into a configuration that is appropriate for the transition state of the $R \rightarrow P E_L T$ reaction, which is located at the point of crossing of the two PE curves. Thus, the rate of the $E_L T$ reaction can be determined by application of transition state theory, resulting in the expression [1.27],

$$k_{E,T} = A \exp\left(\frac{-\Delta G^*}{RT}\right) = \nu_N \kappa \exp\left(\frac{-\Delta G^*}{RT}\right) \quad [1.27]$$

where the pre-exponential A represents the probability of a transition occurring from reactants to products, such that a fully-allowed reaction (wherein the probability of transition ~ 1) has a pre-exponential of $\sim 10^{13} \text{ s}^{-1}$ and occurs at the maximum possible rate of reaction, k_0 ; ν_N is the collisional/vibrational frequency of interaction between states (depending on whether the interaction is inter- or intramolecular); κ is the normalized electronic transmission coefficient, which relates the orientation of a molecule to the probability of $E_L T$ occurring; and ΔG^* (or ΔG^\ddagger) is the Gibbs energy of activation at the transition state (i.e. the point of PE surface crossing). From this point the Marcus theory for electron transfer can be derived, resulting in the well-known expression for the driving force (i.e. Gibbs energy), equation [1.28],²⁴

$$\Delta G^* = \frac{(\Delta G_{00} + \lambda_r)^2}{4\lambda_r} \quad [1.28]$$

and therefore by [1.27] it follows that the rate of $E_L T$ is

$$k_{E,T} = \nu_N \kappa \exp\left(-\frac{(\Delta G_{00} + \lambda_r)^2}{4\lambda_r RT}\right) \quad [1.29]$$

The reorganization energy λ_r is given as $\lambda_r = \lambda_{in} + \lambda_{out}$, where λ_{in} is the inner-sphere (vibrational trapping) reorganizational energy and λ_{out} is the outer-sphere (solvent trapping) reorganizational energy. Using a harmonic oscillator model, λ_{in} is estimated as

$$\lambda_m = \frac{1}{2} \sum_i k_i (d_d^0 - d_u^0)_i^2 \quad [1.30]$$

where k_i is the reduced force constant for the i -th inner shell vibration, $(d_d^0 - d_u^0)_i$ is the difference in the equilibrium bond distances in the two oxidation states, and the summation is over all molecular vibrations. Similarly, λ_{sw} was expanded by Marcus using dielectric continuum theory into

$$\lambda_{sw} = (\Delta e)^2 \left(\frac{1}{2a_d} + \frac{1}{2a_u} + \frac{1}{r} \right) \left(\frac{1}{D_{op}} - \frac{1}{D_s} \right) \quad [1.31]$$

where D_{op} and D_s are the optical and static dielectric constants of the solvent; a_d and a_u are the radii for the donor and acceptor, separated by r ; and Δe is the quantity of charge transferred from one reactant to another.^{2,24}

As shown in **Figure 1.5**, there is often no true "point" of intersection of two surfaces, as the PE wells split apart to form the adiabatic PE surface over which the E_LT reaction will take place, as well as a separate high-lying potential energy surface that is accessible only by a vertical transition. The size of this splitting (that is, the difference in energy between the two PE surfaces at the transition state) is a reflection of the magnitude of electronic coupling between the donor and acceptor states, denoted as H_{AB} . This parameter serves as an indicator of the adiabaticity of the reaction, as a fully non-adiabatic transition will show no splitting and a distinct point of PE surface crossing, while a fully adiabatic transition between highly-coupled states will show a very large separation between ground and excited state PE surfaces.

It is within equation [1.29] that an extremely unexpected result can be found: Marcus' theory states that reaction rates will increase with decreasing ΔG° (increasing driving force) until the reaction becomes energetically barrierless, i.e. $\Delta G^\circ = -\lambda$, and thus $k_{ELT} = \nu_N k$. From this point onward, increasing the driving force for ELT actually yields a *decrease* in reaction rate, and systems for which $\Delta G^\circ < -\lambda$ are said to reside in the *Marcus inverted region*. This counterintuitive result was a source of great controversy until experimentally verified some 25 years after its initial proposal (Figure 1.7).^{13,21}

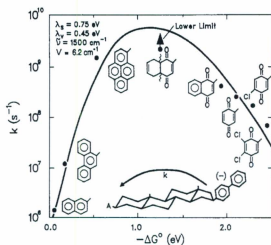


Figure 1.7

Experimental confirmation of the Marcus inverted region in the intramolecular electron transfer reaction of the 4-biphenyl ion to a series of acceptors with similar reorganization energies.²⁵ Adapted with permission from Closs *et al.*, *J. Phys. Chem.* **1986**, *90*, 3673. © 1986 American Chemical Society.

1.4.3 Quantum Mechanical E_LT Theory.

Marcus' derivation of the rate of E_LT from the principles of classical transition state theory clearly allows for E_LT reactions to take place between weakly coupled states *via* small steps along a shared potential energy surface. Such a treatment is naturally ignorant of quantum mechanical effects such as tunneling, but these shortcomings can be addressed in a semi-classical fashion (by introducing coefficients relating to quantum mechanical properties) or by developing the principles of E_LT in a full quantum mechanical treatment. This is necessary to account for E_LT reactions that occur in spite of factors that should cause near-complete cessation of electron transfer (such as, for example, prohibitively large values of ΔG^\ddagger , or a small value of \mathcal{A} in equation [1.27]). As the biggest contribution to the rate of electron transfer is the short-range interaction of a reactant pair, the observed rate for an outer-sphere reaction is given by²⁶⁻²⁹

$$k_{\text{obs}} = K_A k_{E_L T} \quad [1.32]$$

where

$$k_{E_L T} = \nu_n \kappa_{E_L T} \Gamma_A \exp\left(-\frac{\Delta G^\ddagger}{RT}\right) \quad [1.33]$$

where K_A is the equilibrium constant for the formation of the reactant pair separated by a distance r ; ν_n is an effective nuclear frequency; $\kappa_{E_L T}$ is the electronic factor (if $\kappa_{E_L T} \sim 1$ the reaction is adiabatic, if $\kappa_{E_L T} < 1$ it is nonadiabatic); Γ_A is a nuclear tunneling factor; and ΔG^\ddagger is the Gibbs energy of activation of the reaction.

More rigorously, quantum mechanical approaches have been used to explain the behavior of non-adiabatic reactions, wherein simple perturbations are not sufficient to enable coupling of initial and final states *via* a transitory state. Instead, the region of thermal crossing between the two PE surfaces that is created by electronic coupling of states is replaced with a consideration of the overlap of the vibrational wavefunctions of initial and final states. Returning to the Fermi Golden Rule and relating it to an electronic transition,^{26,30}

$$k_{el} = k_{m \rightarrow n} = \frac{2\pi |H_{AB}|^2}{\hbar} \sum_{k=1}^{3N-6} \langle \chi_v^m(Q_k) | \chi_{v'}^n(Q_k) \rangle \rho_{mn} \quad [1.34]$$

the electron transfer of a donor in its vibrational ground state is given by

$$k_{E,T} = \sqrt{\frac{\pi}{\hbar^2 \lambda_{out} k_B T}} |H_{AB}|^2 \sum_{v'=0} \exp(-S) \frac{S^{v'}}{v'!} \exp\left\{-\left[\frac{(\lambda_{out} + \Delta G^0 + v' \hbar \omega)^2}{4\lambda_{out} k_B T}\right]\right\} \quad [1.35]$$

Interestingly, equation [1.35] bears more than a passing resemblance to the Energy Gap Law expression derived in equation [1.17], though they describe very different processes.

1.5 Dendrimers.

1.5.1 Origins and Development of Dendrimer Research.

Early synthetic polymer research was focused on the study of simple linear polymers, wherein the underlying structural motif was generally that of one-dimensional covalent repetition of a small subunit (Figure 1.8). The creation of monomers with the potential to polymerize at more than one site led to branched polymer chains with three-dimensional structure on a local scale, but this method would often tend towards the formation of non-uniform macromolecular structures of somewhat random size and composition. The

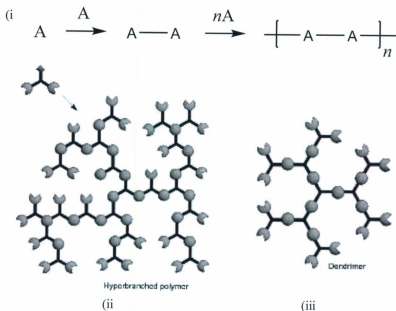


Figure 1.8 Evolution of polymeric structures, from (i) linear chains to (ii) hyperbranched macromolecules to (iii) dendrimers.³¹ Adapted with permission from Grayson, S. M. and Fréchet, J. M. J., *Chem. Rev.* 2001, 101, 3819. © 2001 American Chemical Society.

development of research into combining the best properties of both classes of polymer was initially based in the theoretical works of Flory,³² who examined the feasibility of preparing large three-dimensional branched polymers without the incidence of gelation. Progress towards realizing the macromolecular structures of Flory's theoretical predictions was slow, but the development of an "iterative cascade" method of branched amine polymer synthesis by Vögtle³³ produced the first rational syntheses of the monodisperse three-dimensional macromolecular architectures that would come to be known as dendrimers. However, the modern concept of a dendrimer as a highly-symmetrical globular structure was truly first represented in the Starburst[®] poly(amidoamine) (PAMAM) polymers of Donald Tomalia in 1985.³⁴

Dendrimers (from the Greek word "δέντρο" or "δένδρο", which translates as "tree"³⁵) are composed of a central core surrounded by layers of repeating, branching subunits, and it is by the number of these layers of branches that these macromolecules are characterized (known as the dendrimer "generation"). Finally, capping of each of these individual chains of subunits by an end group terminates the coupling reactions and completes the dendrimer (Figure 1.9). While the quantity of end groups of a family of dendrimers is found to grow exponentially with increasing generation, the volume of the dendrimer can only expand as the cube of the radius, resulting in rising steric dispersion forces concomitant with the increasing density of surface groups until the clustering of surface groups reaches a critical threshold at which uniform growth of further dendrimer generations is no longer possible; this process is described as de Gennes dense packing.³⁶

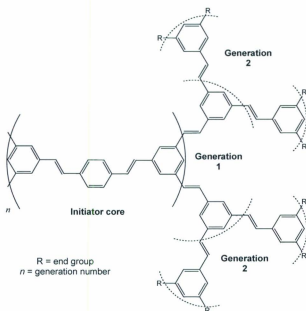


Figure 1.9 Illustration of the general structure of a dendrimer.

In practice, the generation at which the de Gennes limit inhibits further growth varies greatly upon the nature of the dendrimer being prepared, and sometimes does not play a role until the macromolecule in question reaches a truly vast scale; for example, the original synthetic strategies employed in the Starburst[®] molecules were used commercially to prepare PAMAM dendrimers of generation number 13, corresponding to structures with molecular masses in excess of one million daltons.³⁷

The ability to prepare a vast array of dendritic architectures in a controlled and uniform manner allows researchers some ability to alter and tune their physical properties as desired. Furthermore, the properties of low generation number dendrimers can vary

quite profoundly from high generation number dendrimers with the same repeating subunits and end groups owing to the isolated, globular nature of these macromolecules.

As these structures become increasingly crowded on their periphery, the centre of the nanostructure can become isolated from its environment, resulting in a structure whose properties are largely governed by the end groups, largely irrespective of the nature of the internal subunits that make up the dendrimer (described as "site isolation" in recognition of the use of this phrase to describe the effects of protein folding about the active sites of enzymes).^{38,39} As a dendrimer increases in generation number, the number of capping end groups increases exponentially and shields the long chains of repeating subunits that make up the interior of the macromolecule. Consequentially, the physical and chemical properties of dendrimers are initially driven by the properties of the individual branching chains but become increasingly dominated by the end groups in larger generations, such that modification of the external groups can greatly change their physical properties (Figure 1.10).³¹ This non-aggregating, globular nature persists in the molten state, making them potentially useful as additives in materials science.⁴⁰

1.5.2 Synthetic Strategies.

Modern methods for dendrimer synthesis were developed in order to combine the best properties of both linear and hyperbranched polymers into a uniform three-dimensional macromolecular architecture. By using iterative chain-lengthening synthetic methods, dendrimers are produced with a desirable combination of the uniformity of linear

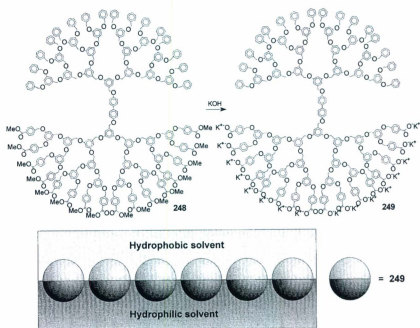


Figure 1.10 Demonstration of how the properties of large sterically-crowded dendrimers are driven by their surface groups.³¹ Adapted with permission from Grayson, S. M. and Fréchet, J. M. J., *Chem. Rev.* 2001, 101, 3819. © 2001 American Chemical Society.

polymers and the three-dimensional scale of hyperbranched polymers. Importantly, the monodispersity of these molecules simplifies the correlation of their observed physical and chemical properties with their own physical dimensions and surface topology.

Tomalia's aforementioned work in PAMAM dendrimer synthesis is exemplary of the cascading, or "divergent" synthetic method, whereby an initiator core is expanded upon, layer-by-layer, in a stepwise fashion to iteratively prepare larger and larger structures (Figure 1.11). A synthetic scheme that typifies this method employs a monomer with two

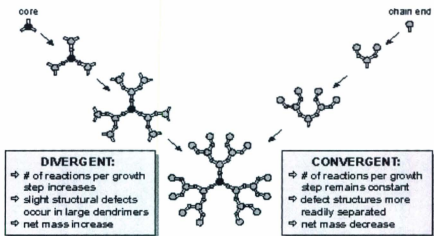


Figure 1.11 Representation of the convergent and divergent synthetic methods.³⁷ © 2002 Wiley Periodicals, Inc..

active functionalities, whereby one is usually a protected or modified version of the active sites found on the core molecule and the other is reactive to these core molecule groups. Exposure of the core molecule to an excess of monomeric reagent followed by separation and purification steps should yield a monodisperse, first-generation dendrimer product. By this strategy the steps of reaction, purification and deprotection are cycled to make progressively larger and larger dendrimers; however, while the generation number increases linearly, the number of active sites that require deprotection and coupling increases exponentially, such that the efficacy of the synthetic strategy becomes limited both by its capability to carry out these propagation cycles quantitatively and in the methods used to achieve this objective.

As the ultimate goal is to achieve the synthesis of fully monodisperse macromolecular assemblies, complete inhibition of site defect formation is of critical importance. This challenge is temporarily overcome by using a large excess of reagents to drive the equilibrium towards the monodisperse product, but as the number of active sites increases exponentially the quantity of reagent required increases at an even greater rate. Ultimately, the ability to extend the dendrimer generation to larger and larger sizes becomes dependent upon the kinetics of the reaction, the ability to isolate and purify the end product from ever-increasing quantities of side product and unused reagent, and in steric encumbrance within the final product. Once sterics start to interfere with the complete conversion of all available reaction sites then purification is required to eliminate side products. However, with increasing generation this task also becomes increasingly onerous, as the magnitude of difficulty of separating "fully-monodisperse" product from "nearly-monodisperse" side product scales dramatically with increasing generation, especially as the size of the molecule approaches the de Gennes limit and the surface characteristics of the various products become virtually indistinguishable.³¹

The second synthetic strategy in use is the "convergent" method (Figure 1.11), which was first advanced and popularized by Jean Fréchet⁴¹ in order to minimize the difficulties caused by exponential scaling encountered in the divergent synthetic approach. While the latter method is an expensive approach that requires a great deal of synthetic material and time and effort for separation/purification, the convergent strategy is not unlike that used in conventional organic synthetic chemistry, whereby a large target molecule is first

retrosynthetically fragmented into smaller segments and each segment is then synthesized separately in order to minimize the profound impact of product losses by non-quantitative reaction yields and sample handling on overall product yield. The convergent strategy of building dendrimers from the terminal groups towards the core reduces the number of active sites with each successive iteration, thereby eliminating the requirement for exponentially increasing quantities of starting materials to drive the reaction equilibrium to completion at all active sites. As a result, convergent synthetic methodologies tend to produce dendrimers with greater monodispersity than their divergent counterparts.⁴²

Though not exploited in the dendrimers studied in this Dissertation, an attractive feature of convergent synthetic strategies is that they can allow for the introduction of more than one type of peripheral or spacer group in the final molecule, which can theoretically expand their utility by, for example, enabling such a polyfunctional dendrimer to simultaneously carry out multiple processes.⁴³⁻⁴⁵

1.5.3 Photoinduced $E_N T$ and $E_L T$ in Dendrimers.

An important feature of dendrimers is that they provide researchers with the means to prepare a stunning variety of structures by enabling the synthesis of larger and larger monodisperse macromolecules with large surface areas. The ability to arrange multiple chromophoric groups into well-defined polymeric arrays⁴⁶ and the means to prepare long conjugated⁴⁷⁻⁴⁹ or non-conjugated^{46,49,50} chains to funnel charge and/or energy to a central acceptor core seems to be a perfect fit for researchers hoping to create novel materials for

photoinduced charge and energy transfer or artificial photosynthetic applications. In particular, the three-dimensional hyperbranched structure that is the hallmark of these macromolecules makes them ideal antennae for light-harvesting applications.^{46,51,52} This expansive structure potentially allows for absorption of a large cross-section of incident photons, enabling the transfer of photonic energy through the dendritic structure by multi-step electron⁵³⁻⁵⁷ or energy transfer^{49,57-63} reactions, eventually terminating in (for example) a redox-active site. A great deal of research effort has been invested into energy transfer processes in these dendritic systems, specifically into the ability of dendrimer singlet states to carry out through-space energy transfer *via* dipole-dipole coupling of donor and acceptor states (i.e. the Förster E_NT mechanism).⁶⁴ Alternately, short range E_NT can also occur by a Dexter mechanism, whereby the method of transfer is by an electron exchange process, and is therefore dependent on the degree of overlap between the donor and acceptor states. Of the two, the role of the Dexter pathway in these dendrimers seems to be less thoroughly investigated.⁶³⁻⁶⁸

However, as dendrimers grow to ever larger and larger sizes, they begin to exhibit properties that are deleterious to their utility as conduits for energy and/or electrons. With increasing dendrimer generation (and, thus, increasing size and molecular weight) these complex macromolecules can begin to suffer from internal backfolding as a consequence of their internal flexibility and due to the close packing of their polymer chains. This internal association of neighbouring dendrons can lead to excimer formation and quenching side reactions, so bigger molecules and larger numbers of chromophores

will not necessarily yield better results in charge/energy transfer applications.^{46,69} The key, it seems, is to strike a balance between the enhanced opportunity of photon absorption afforded by creating larger dendrimers with more chromophores, with the increased likelihood that this increase in molecular size will cause quenching side reactions, due to the interaction of neighbouring dendron arms.

1.5.4 Poly(aryl ether) (Fréchet-type) Dendrimers.

Dendrimers based upon the 3,5-dihydroxybenzyl alcohol monomer were successfully prepared by the research group of Fréchet⁴¹ in the first example of a convergent dendrimer synthesis, and these poly(aryl ether) structures are commonly called Fréchet-type dendrimers in recognition of this fact (e.g. **Figure 1.10**). Their relative ease of preparation has led to the synthesis of a wide variety of structures by modification of this simple monomeric unit (**Figure 1.12**),³¹ as well as by the introduction of other functional groups into the polymer structure. For example, in order to overcome the steric hindrance that impedes synthesis of larger dendrimers (beyond the 5th generation), the use of monomers with spacer groups has been successful in synthesizing larger structures and with better yields than is possible with the 3,5-dihydroxybenzyl alcohol-based synthesis.^{31,41,70-73} Poly(aryl ether) dendrimers based on this synthetic strategy have been used in a wide variety of light harvesting applications.⁷⁴⁻⁷⁸

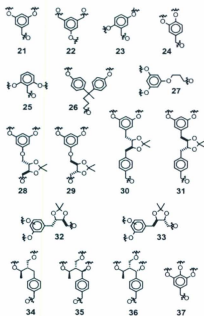


Figure 1.12 A selection of monomers that have been used in the preparation of Fréchet-type poly(aryl ether) dendrimers.³¹ Adapted with permission from Grayson, S. M. and Fréchet, J. M. J., *Chem. Rev.* **2001**, *101*, 3819. © 2001 American Chemical Society.

1.5.5 Poly(phenylenevinylene) Dendrimers.

The literature regarding the synthesis and properties of poly(phenylenevinylene) dendrimers is rather scant relative to that for the poly(aryl ether) dendrimers. The purpose of constructing a dendrimer in such a manner is to yield a highly conjugated polymer for the purposes of efficient E_NT ; however, the physical properties of macromolecules such as dendrimers are often far less straightforward and predictable than expected. The synthesis of a poly(phenylenevinylene) dendrimer requires strict control of

the stereochemistry of the alkene functionalities, while the presence of myriad stilbene groups introduces the potential for photoinduced isomerizations and undesired side reactions;⁷⁹⁻⁸² this topic is addressed in the following Sections. In addition, the 1,3,5-trisubstituted nature of the aryl rings in these polymers introduces cross-conjugation⁸³ and was thought to limit their utility and efficiency as E_{NT}/E_{LT} antennae, though subsequent research has suggested that this may only be valid in the ground state (Figure 1.13).⁶⁴ There have been few reports of the photophysical properties of such structures, save for discussions regarding photoisomerization of the stilbenoid moieties.⁷⁹⁻⁸² The exception to this is in the research of Burn *et al.* into the utility of these polymers as organic LEDs, where spin-coating of these molecules into films virtually eliminates any deleterious side reactions.⁸³⁻⁸⁸

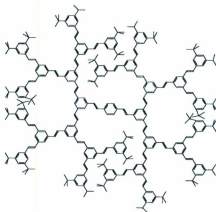


Figure 1.13 Example of a poly(phenylenevinylene) dendrimer.⁸⁴ © 1999 WILEY-VCH Verlag GmbH, Weinheim, Fed. Rep. of Germany.

1.5.6 Excited State Properties of Stilbene.

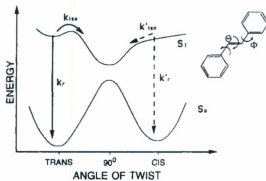


Figure 1.15 Potential energy surfaces of the S_0 and S_1 states of stilbene.⁸⁹ Adapted with permission from Waldeck, D. H., *Chem. Rev.* 1991, 91, 415. © 1991 American Chemical Society.

The photodynamics of stilbene and its related compounds have been studied for over 65 years, as it is an ideal structural motif for examining the intimate details of the properties of C=C bonds in general and of *cis/trans* isomerization processes in particular.⁸⁹ Isomerization in stilbene is a rapid and efficient process that can proceed via direct photoinitiation or by sensitization through inter- or intramolecular energy transfer.^{80,90,91} Upon irradiation the stilbene molecule isomerizes from *cis*-to-*trans* or *trans*-to-*cis*, depending on the initial configuration of the parent molecule upon excitation. Though the potential barrier to rotation about this C=C bond is sufficiently large to inhibit thermal isomerization along the ground state potential energy surface from either isomer, this barrier is circumvented upon excitation of either isomer to the excited state potential energy surface (Figure 1.14). The *cis* and *trans* isomers can freely interconvert between

each other on the S_1 potential energy surface with a small thermal barrier to *trans*-to-*cis* isomerization due to the existence of a "twisted" singlet state that lies on a shared pathway to isomerization between the *cis* and *trans* S_1 states (herein named $^1c^*$ and $^1t^*$, respectively).^{90,92,93} In opposition to its role in the ground state - where the intermediate state lies at the apex of the barrier to rotation between the isomers - this twisted excited state lies at lower energy than either S_1 state, and the intermediate to isomerization is at its lowest energy when rotation of half of the molecule about the C=C double bond forms a perpendicular geometry (referred to as $^1p^*$) relative to the plane of the other half of the molecule.⁸⁹ Whereas the *trans*-stilbene isomer is fluorescent ($\phi_{em} = 0.04$, $\tau = 70$ ps) the *cis* isomer is both non-fluorescent and photochemically reactive, either undergoing *cis*-to-*trans* isomerization or cyclization to form dihydrophenanthrene (DHP), with the latter process occurring with a quantum yield on the order of $\phi = 0.10$.⁹⁴ While this cyclization is reversible in an inert atmosphere, dehydrogenation takes place in air (or in the presence of a suitable oxidant) to form phenanthrene.⁹⁰

While these properties have been carefully studied and rather well mapped out, the interaction of isomers of stilbene with triplet excited state donors is rather less straightforward. It was found by Hammond *et al.* that *cis*-stilbene is not only an eager acceptor of triplet excitation energy but that it does so very quickly and at unexpectedly large rates. Notably, there are cases where the energy of the donating triplet state lies below that of the accepting triplet state of the *cis*-stilbene molecule, but the transfer nonetheless proceeds.^{91,95-97} It is believed this is because the geometry of the excited state

that is formed upon photoexcitation is not representative of the excited state that is involved at the moment of sensitization, such that the true accepting state lies at a lower energy than that expected of the triplet excited state based on the Franck-Condon geometry. This process is described as “nonvertical” energy transfer, owing to the fact that the geometry formed from the “vertical” (i.e. spectroscopic) photoexcitation and energy transfer pathway is not representative of the true active species.^{91,96,98}

The T_1 potential energy surface for stilbene also demonstrates a low-lying $^3p^*$ twisted state that is nearly degenerate with the 1p twisted state.⁹⁹ The $^3p^*$ state is analogous to the $^1p^*$ state in that it lies between the $^3c^*$ and $^3t^*$ excited states with an activation barrier impeding $^3t^* \rightarrow ^3c^*$, so the mechanism of population of either ground state isomer follows a similar pathway from both the $^3p^*$ and $^1p^*$ states (Figure 1.15).

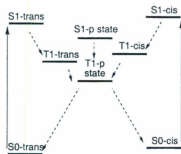


Figure 1.15 Overview of the potential fates of excited states of stilbene.¹⁰⁰ Adapted with permission from Dugave, C. and Demange, L., *Chem. Rev.* 2003, 103, 2475. © 2003 American Chemical Society.

1.5.6.1 *cis-trans* Isomerism in Sterically-Hindered Environments.



Figure 1.17 Comparison of the "hula twist" (HT) to the "one-bond flip" (OBF) olefinic isomerization mechanism.¹⁰¹ © 2001 WILEY-VCH Verlag GmbH, Weinheim, Fed. Rep. of Germany.

The ability of the isomers of stilbene and other such small molecules to quickly and efficiently rotate about their C=C bond is logically not shared by sterically-encumbered compounds, such as the poly(phenylenevinylene) dendrimers of Deb *et al.*¹⁰² Such molecules can have molecular weights that number into the thousands of grams per mole, and simple 180° rotation about a single C=C bond would not be possible without considerable volume displacement, solvent reorganization and expenditure of energy. However, it has been reported that such molecules not only undergo *cis/trans* isomerization, but that the rate of such processes is largely insensitive to the size of the compound, even when considering the 3rd or 4th generations of these dendrimers. The mechanism for isomerization in these compounds is not a simple 180° one-bond rotation but rather a so-called "hula twist" mechanism, whereby the bonds on either side of a central atom undergo a concerted rotation, inverting the stereochemistry about the olefinic bond (Figure 1.17).^{101,103,104} This mechanism involves almost no side chain motion relative to that of the one-bond rotation model, and as such the hula twist mechanism is predominant in situations where steric encumbrance or restriction of motion due to rigid

media or low temperature are a concern.^{101,103,105} This has been proposed as the active mechanism in the *cis/trans* isomerization of the stilbene-centered poly(benzyl ether) dendrimers of Arai, where structures of $M_w \sim 6000 \text{ g mol}^{-1}$ were found to isomerize within 10 ns.¹⁰⁵ Interestingly, it has been reported that the presence of steric hindrance is not a requirement, as studies of free stilbenes in the gas phase suggest that the hula twist mechanism may in fact represent the lowest energy pathway.¹⁰⁶

1.6 Conclusion.

The preceding Sections serve to summarize key concepts in photophysics that pertain to the study of the types of chromophoric systems described in this Dissertation. For the purposes of the work presented here, an introduction of key theoretical concepts - such as the Fermi Golden Rule and the Franck-Condon Principle - is important for developing an understanding of the importance of later topics, among which the Energy Gap Law and the inverted region (as predicted by Marcus Theory) are of particular relevance. This discussion of the underlying theory is succeeded by an introduction of the physical and electronic properties of dendrimers in general, as well as of the poly(aryl ether) and poly(phenylenevinylene) dendrimers discussed in this Dissertation in particular, as this information is vital to gaining a comprehensive understanding of the photophysics of this class of molecules.

1.7 References.

- (1) In *Comprehensive Chemical Kinetics*; Compton, R. G., Ed.; Elsevier: 1990; Vol. Volume 30, p 69.
- (2) Turro, N. J.; Ramamurthy, V.; Scaiano, J. C. *Modern Molecular Photochemistry of Organic Molecules*; University Science Books: Sausalito, California, 2010.
- (3) Depiction of Franck-Condon principle in absorption and fluorescence. Distributed under the terms of the GNU Free Documentation License (<http://creativecommons.org/licenses/by-sa/3.0/deed.en>), Somoza, M. M., 2006.
- (4) Claude, J. P. Ph.D. Dissertation, University of North Carolina at Chapel Hill, 1995.
- (5) Bixon, M.; Jortner, J. *J. Chem. Phys.* **1968**, *48*, 715.
- (6) Englman, R.; Jortner, J. *Mol. Phys.* **1970**, *18*, 145.
- (7) Freed, K. F.; Jortner, J. *J. Chem. Phys.* **1970**, *52*, 6272.
- (8) Freed, K. J. *Top. Curr. Chem.* **1972**, *31*, 65.
- (9) Heller, E. J.; Brown, R. C. *J. Chem. Phys.* **1983**, *79*, 3336.
- (10) Lin, S. H. *J. Chem. Phys.* **1966**, *44*, 3759.
- (11) Lin, S. H. *Radiationless Transitions*; Academic: New York, 1980.
- (12) Englman, R.; Jortner, J. *Mol. Phys.* **1970**, *18*, 145.
- (13) Marcus, R. *J. Phys. Chem.* **1986**, *90*, 3460.
- (14) Förster, T. *Discuss. Faraday Soc.* **1959**, *27*, 7.
- (15) Murtaza, Z.; Graff, D.; Zipp, A.; Worl, L.; Jones, W. A.; Bates, W.; Meyer, T. J. *J. Phys. Chem.* **1994**, *98*, 10504.
- (16) Scholes, G. D. *J. Phys. Chem. Lett.* **2012**, *1*, 2.
- (17) Collini, E.; Scholes, G. D. *Science* **2009**, *323*, 369.
- (18) Förster, T. *Ann. Physik* **1948**, *437*, 55.
- (19) Dexter, D. L. *J. Chem. Phys.* **1953**, *21*, 836.
- (20) Stryer, L.; Haugland, R. P. *Proc. Natl. Acad. Sci. USA* **1967**, *58*, 719.
- (21) Kavarnos, G. J.; Turro, N. J. *Chem. Rev.* **1986**, *86*, 401.

- (22) Libby, W. F. *Annu. Rev. Phys. Chem.* **1977**, *28*, 105.
- (23) Parameters of the Marcus Equation. Image released into the public domain by the author., Holman, M., 2007.
- (24) Marcus, R. *Rev. Mod. Phys.* **1993**, *65*, 599.
- (25) Closs, G.; Calcaterra, L.; Green, N.; Penfield, K.; Miller, J. J. *Phys. Chem.* **1986**, *90*, 3673.
- (26) Meyer, T. J.; Taube, H. In *Comprehensive Coordination Chemistry* 1987; Vol. 1, p 331.
- (27) Kestner, N.; Logan, J.; Jortner, J. J. *Phys. Chem.* **1974**, *78*, 2148.
- (28) Sutin, N.; Creutz, C. *Adv. Chem. Ser.* **1978**, *168*, 1.
- (29) Sutin, N.; Creutz, C. *J. Chem. Ed.* **1983**, *60*, 809.
- (30) Marcus, R.; Sutin, N. *Biochim. Biophys. Acta* **1985**, *811*, 265.
- (31) Grayson, S.; Fréchet, J. M. J. *Chem. Rev.* **2001**, *101*, 3819.
- (32) Flory, P. J. *J. Am. Chem. Soc.* **1952**, *74*, 2718.
- (33) Buhleier, E.; Wehner, W.; Vögtle, F. *Synthesis* **1978**, 155.
- (34) Tomalia, D.; Baker, H.; Dewald, J.; Hall, M.; Kallos, G.; Martin, S.; Roeck, J.; Ryder, J.; Smith, P. *Polym. J.* **1985**, *17*, 117.
- (35) Dykes, G. J. *Chem. Technol. Biotechnol.* **2001**, *76*, 903.
- (36) de Gennes, P.; Herve, H. *J. Physique Lett.* **1983**, *44*, 351.
- (37) Tomalia, D.; Fréchet, J. M. J. *J. Polym. Sci. Part A: Polym. Chem.* **2002**, *40*, 2719.
- (38) Hecht, S.; Fréchet, J. M. J. *Angew. Chem. Int. Ed.* **2001**, *40*, 74.
- (39) Cameron, C. S.; Gorman, C. B. *Adv. Funct. Mater.* **2002**, *12*, 17.
- (40) Bodnár, I.; Silva, A. S.; Deitcher, R. W.; Weisman, N. E.; Kim, Y. H.; Wagner, N. J. *J. Polym. Sci. Part B: Polym. Phys.* **2000**, *38*, 857.
- (41) Hawker, C. J.; Fréchet, J. M. J. *J. Am. Chem. Soc.* **1990**, *112*, 7638.
- (42) Mansfield, M. *Macromolecules* **1993**, *26*, 3811.
- (43) Larré; Bressolles, D.; Turrin, C.; Donnadiou, B.; Caminade, A.-M.; Majoral, J.-P. *J. Am. Chem. Soc.* **1998**, *120*, 13070.

- (44) Maraval, V.; Laurent, R.; Donnadiou, B.; Mauzac, M.; Caminade, A.-M.; Majoral, J.-P. *J. Am. Chem. Soc.* **2000**, *122*, 2499.
- (45) Freeman, A.; Christoffels, L.; Fréchet, J. M. J. *J. Org. Chem.* **2000**, *65*, 7612.
- (46) Stewart, G.; Fox, M. *J. Am. Chem. Soc.* **1996**, *118*, 4354.
- (47) Devadoss, C.; Bharathi, P.; Moore, J. S. *J. Am. Chem. Soc.* **1996**, *118*, 9635.
- (48) Wang, Y.; Ranasinghe, M. I.; Goodson, T. *J. Am. Chem. Soc.* **2003**, *125*, 9562.
- (49) Justin Thomas, K.; Thompson, A.; Sivakumar, A.; Bardeen, C.; Thayumanavan, S. *J. Am. Chem. Soc.* **2005**, *127*, 373.
- (50) Hahn, U.; Gorka, M.; Vögtle, F.; Vicinelli, V.; Ceroni, P.; Maestri, M.; Balzani, V. *Angew. Chem. Int. Ed.* **2002**, *41*, 3595.
- (51) Newkome, G. R.; He, E.; Moorefield, C. N. *Chem. Rev.* **1999**, *99*, 1689.
- (52) Bosman, A.; Janssen, H.; Meijer, E. *Chem. Rev.* **1999**, *99*, 1665.
- (53) Ghaddar, T.; Wishart, J.; Kirby, J.; Whitesell, J.; Fox, M. A. *J. Am. Chem. Soc.* **2001**, *123*, 12832.
- (54) Ghaddar, T.; Wishart, J.; Thompson, D. W.; Whitesell, J.; Fox, M. A. *J. Am. Chem. Soc.* **2002**, *124*, 8285.
- (55) Luo, H.; Choi, M.-S.; Araki, Y.; Ito, O.; Aida, T. *Bull. Chem. Soc. Japan* **2005**, *78*, 405.
- (56) Capitosti, G. J.; Cramer, S. J.; Rajesh, C. S.; Modarelli, D. A. *Org. Lett.* **2001**, *3*, 1645.
- (57) Houjeiry, T. I.; Ghaddar, T. H. *Chem. Phys. Lett.* **2008**, *460*, 543.
- (58) Kimura, M.; Shiba, T.; Muto, T.; Hanabusa, K.; Shirai, H. *Tetrahedron Lett.* **2000**, *41*, 6809.
- (59) Larsen, J.; Brüggemann, B.; Polívka, T.; Sundström, V.; Åkesson, E.; Sly, J.; Crossley, M. J. *J. Phys. Chem. A* **2005**, *109*, 10654.
- (60) Ranasinghe, M. I.; Hager, M. W.; Gorman, C. B.; Goodson, T. *J. Phys. Chem. B* **2004**, *108*, 8543.

- (61) de Schryver, F. C.; Vosch, T.; Cotlet, M.; Van der Auweraer, M.; Müllen, K.; Hofkens, J. *Acc. Chem. Res.* **2005**, *38*, 514.
- (62) Kodis, G.; Terazono, Y.; Liddell, P. A.; Andréasson, J.; Garg, V.; Hamburger, M.; Moore, T. A.; Moore, A. L.; Gust, D. *J. Am. Chem. Soc.* **2006**, *128*, 1818.
- (63) Chen, J.; Li, S.; Zhang, L.; Liu, B.; Han, Y.; Yang, G.; Li, Y. *J. Am. Chem. Soc.* **2005**, *127*, 2165.
- (64) Thompson, A.; Gaab, K.; Xu, J.; Bardeen, C.; Martinez, T. *J. Phys. Chem. A* **2004**, *108*, 671.
- (65) Bergamini, G.; Ceroni, P.; Maestri, M.; Balzani, V.; Lee, S.-K.; Vögtle, F. *Photochem. Photobiol. Sci.* **2004**, *3*, 898.
- (66) Chen, J.; Li, S.; Zhang, L.; Li, Y.-Y.; Chen, J.; Yang, G.; Li, Y. *J. Phys. Chem. B* **2006**, *110*, 4047.
- (67) Zhang, L.; Chen, J.; Li, S.; Chen, J.; Li, Y.-Y.; Yang, G.; Li, Y. *J. Photochem. Photobiol., A* **2006**, *181*, 429.
- (68) de Carvalho, I. M.; de Sousa Moreira, O.; Gehlen, M. *Inorg. Chem.* **2003**, *42*, 1525.
- (69) Sullivan, P.; Rommel, H.; Liao, Y.; Olbricht, B.; Akelaitis, A.; Firestone, K.; Kang, J.-W.; Luo, J.; Davies, J.; Choi, D.; Eichinger, B.; Reid, P.; Chen, A.; Jen, A.; Robinson, B.; Dalton, L. *J. Am. Chem. Soc.* **2007**, *129*, 7523.
- (70) Moore, J. S. *Acc. Chem. Res.* **1997**, *30*, 402.
- (71) Moore, J. S.; Xu, Z. *Macromolecules* **1991**, *24*, 5893.
- (72) Wooley, K. L.; Hawker, C. J.; Fréchet, J. M. J. *J. Am. Chem. Soc.* **1991**, *113*, 4252.
- (73) Xu, Z.; Moore, J. S. *Angew. Chem. Int. Ed.* **1993**, *32*, 246.
- (74) Adronov, A.; Malenfant, P. R. L.; Fréchet, J. M. J. *Chem. Mater.* **2000**, *12*, 1463.
- (75) Gilat, S. L.; Adronov, A.; Fréchet, J. M. J. *Angew. Chem. Int. Ed.* **1999**, *38*, 1422.
- (76) Gilat, S. L.; Adronov, A.; Fréchet, J. M. J. *J. Org. Chem.* **1999**, *64*, 7474.
- (77) Kawa, M.; Fréchet, J. M. J. *Chem. Mater.* **1998**, *10*, 286.

- (78) Ceroni, P.; Vicinelli, V.; Maestri, M.; Balzani, V.; Muller, W. M.; Muller, U.; Hahn, U.; Osswald, F.; Vögtle, F. *New J. Chem.* **2001**, *25*, 989.
- (79) Imai, M.; Ikegami, M.; Momotake, A.; Nagahata, R.; Arai, T. *Photochem. Photobiol. Sci.* **2003**, *2*, 1181.
- (80) Momotake, A.; Arai, T. *J. Photochem. Photobiol., C* **2004**, *5*, 1.
- (81) Uda, M.; Mizutani, T.; Hayakawa, J.; Momotake, A.; Ikegami, M.; Nagahata, R.; Arai, T. *Photochem. Photobiol.* **2002**, *76*, 596.
- (82) Uda, M.; Momotake, A.; Arai, T. *Org. Biomol. Chem.* **2003**, *1*, 1635.
- (83) Halim, M.; Pillow, J.; Samuel, I.; Burn, P. *Synth. Met.* **1999**, *102*, 922.
- (84) Halim, M.; Pillow, J.; Samuel, I.; Burn, P. *Adv. Mater.* **1999**, *11*, 371.
- (85) Halim, M.; Samuel, I.; Pillow, J.; Burn, P. *Synth. Met.* **1999**, *102*, 1113.
- (86) Halim, M.; Samuel, I.; Pillow, J.; Monkman, A.; Burn, P. *Synth. Met.* **1999**, *102*, 1571.
- (87) Pillow, J.; Burn, P.; Samuel, I.; Halim, M. *Synth. Met.* **1999**, *102*, 1468.
- (88) Pillow, J. N. G.; Halim, M.; Lupton, J. M.; Burn, P. L.; Samuel, I. D. W. *Macromolecules* **1999**, *32*, 5985.
- (89) Waldeck, D. H. *Chem. Rev.* **1991**, *91*, 415.
- (90) Wrighton, M.; Markham, J. *J. Phys. Chem.* **1973**, *77*, 3042.
- (91) Schanze, K. S.; Lucia, L.; Cooper, M.; Walters, K.; Ji, H.-F.; Sabina, O. *J. Phys. Chem. A* **1998**, *102*, 5577.
- (92) Saltiel, J. *J. Am. Chem. Soc.* **1967**, *89*, 1036.
- (93) Olson, A. *Trans. Faraday Soc.* **1931**, *27*, 69.
- (94) Muszkat, K. A.; Fischer, E. *J. Chem. Soc. B* **1967**, 662.
- (95) Saltiel, J.; Hammond, G. S. *J. Am. Chem. Soc.* **1963**, *85*, 2515.
- (96) Hammond, G. S.; Saltiel, J. *J. Am. Chem. Soc.* **1963**, *85*, 2516.
- (97) Herkstroeter, W.; Hammond, G. *J. Am. Chem. Soc.* **1966**, *88*, 4769.
- (98) Saltiel, J.; Marchand, G.; Kirkor-Kaminska, E.; Smothers, W.; Mueller, W.; Charlton, J. *J. Am. Chem. Soc.* **1984**, *106*, 3144.

- (99) Ni, T.; Caldwell, R.; Melton, L. *J. Am. Chem. Soc.* **1989**, *111*, 457.
- (100) Dugave, C.; Demange, L. *Chem. Rev.* **2003**, *103*, 2475.
- (101) Liu, R. S. H.; Hammond, G. S. *Chem. Eur. J.* **2001**, *7*, 4536.
- (102) Deb, S.; Maddux, T.; Yu, L. *J. Am. Chem. Soc.* **1997**, *119*, 9079.
- (103) Liu, R. S. H. *Acc. Chem. Res.* **2001**, *34*, 555.
- (104) Liu, R. S.; Asato, A. E. *Proc. Natl. Acad. Sci. USA* **1985**, *82*, 259.
- (105) Mizutani, T.; Ikegami, M.; Nagahata, R.; Arai, T. *Chem. Lett.* **2001**, *30*, 1014.
- (106) Fuß, W.; Kosmidis, C.; Schmid, W. E.; Trushin, S. A. *Angew. Chem. Int. Ed.* **2004**, *43*, 4178.

Chapter 2. Conformational Dynamics of Dendritic Poly(phenylenevinylene)-Substituted Bipyridines in $[\text{Ru}(\text{bpy})_2(\text{L})]^{2+}$ Complexes.

2.1 Introduction.

A family of 2,2'-bipyridines with substitutions by poly(phenylenevinylene)-based dendrimers in the 5 and 5' positions are examined, both as free ligands and as part of heteroleptic ruthenium polypyridyl complexes. Analysis of these Ru metal complexes by emission spectral fitting and global analysis reveals that conformational dynamics attenuate delocalization of the $^3\text{MLCT}$ state onto the dendron arms. This inhibits intraligand charge transfer between bpy-based and dendrimer-based $^3\text{MLCT}$ states, giving rise to dual emission from these states as well as the observation of growth kinetics on a nanosecond timescale in fluorescence and transient absorption decay measurements.

2.1.1 Photophysics of Ru^{II} Polypyridyl Metal Complexes.

Ruthenium (II) tris-2,2'-bipyridine ion (Figure 2.1) and its associated family of Ru^{II} polypyridyl compounds make up one of the most thoroughly studied and well-documented classes of transition metal coordination compounds in Chemistry. Since the first reference to the luminescent properties of $[\text{Ru}(\text{bpy})_3]^{2+}$ was reported nearly 50 years ago by Paris and Brandt,¹ these octahedral d^6 coordination complexes of approximately D_3 symmetry have been successfully employed in a broad array of photoconversion devices and applications including dye-sensitized solar cells (DSSCs, or Grätzel cells),² DNA or protein probes,^{3,4} medical imaging and anti-cancer applications,⁵⁻⁸ pressure-sensitive

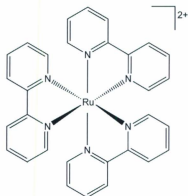


Figure 2.1 Structure of $[\text{Ru}(\text{bpy})_3]^{2+}$.

dyes⁹, and photochemical water oxidation centres,^{10,11} which illustrates the diversity of the chemistry of these compounds. The widespread utility of Ru^{II} polypyridyl compounds is due to their favourable chemical properties such as potent excited state redox character (Figure 2.2), long-term stability, long-lived luminescent excited states, and – at least for the less complex cases – relative ease of preparation.¹² Despite these successes, there are still many unanswered questions about these compounds, and a tremendous amount of current research effort is being dedicated to the goal of gaining a comprehensive understanding of the photophysical properties and behaviour of Ru^{II} polypyridyl complexes, from initial photon capture to form the Franck-Condon state, through the onset of solvent dynamics and vibrational reorganization, and on to the formation of a thermally equilibrated excited state and/or to excited-state relaxation *via* any one of a number of available pathways.

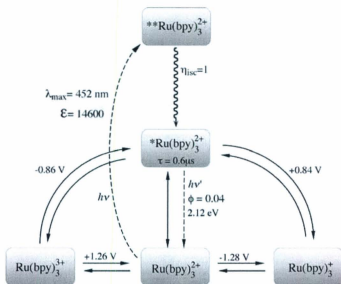


Figure 2.2 Summary of relevant species and molecular quantities associated with energy and electron transfer processes of $[\text{Ru}(\text{bpy})_3]^{2+}$ relative to the ground state. With kind permission from Springer Science+Business Media: Photochemistry and Photophysics of Coordination Compounds: Ruthenium, 2007, p. 129, Sebastiano Campagna, Fig. 10.

While a key highlight of Paris and Brandt's report was their early recognition that the transition of an electron from a Ru d orbital to an antibonding π^* orbital on a bipyridine ligand yields a broad absorption band due to the availability of a number of vibrationally excited π^* ligand states,¹ it is now more clearly known that the symmetry and apparent simplicity of the $[\text{Ru}(\text{bpy})_3]^{2+}$ ion belie the presence and mutual interaction of a complex manifold of closely-spaced, thermally-accessible excited states (Figure 2.3).¹³⁻¹⁶ The absorption spectrum of $[\text{Ru}(\text{bpy})_3]^{2+}$ is primarily characterized by a strong, sharp high energy band at ~ 285 nm and a broad absorbance centred at ~ 450 nm. The high energy

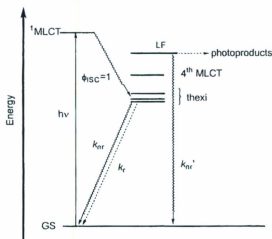


Figure 2.3 Jablonski diagram of $[\text{Ru}(\text{bpy})_3]^{2+}$ at room temperature. Adapted with permission from Qu *et al.*, *Langmuir* 2000, 16, 4662.¹⁶ © 2000 American Chemical Society.

transition is a ligand-centred (LC) band that arises from $\pi \rightarrow \pi^*$ transitions, while the characteristically broad absorption band results from promotion of a metal-centred $d\pi_{Ru}$ electron into one of several available ligand-based π_{bpy}^* states of predominantly singlet character ($(d\pi_{Ru})^6 \rightarrow [(d\pi_{Ru})^5(\pi_{bpy}^*)^1]$) and is known as a metal-ligand charge transfer (MLCT) transition (Figure 2.4).^{12,13} This $^1\text{MLCT}$ excited state is very weakly emissive and extremely short-lived with a decay lifetime of (15 ± 10) fs in H_2O ,¹⁷ and its formation is succeeded by an ultrafast non-radiative internal conversion from this state of mostly singlet character to a state of mostly triplet character ($^3\text{MLCT}$) in a process known as intersystem crossing (ISC). These are described as being states of “mostly” singlet and triplet character because the presence of the heavy Ru atom causes spin state mixing

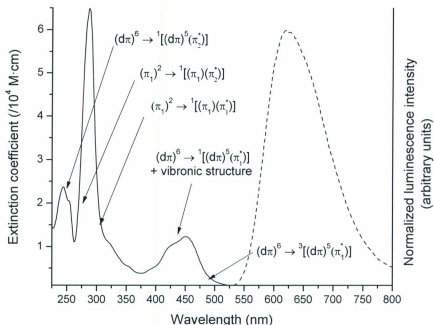


Figure 2.4 Absorbance (solid, with electronic transitions listed)^{12,18} and corrected luminescence (dashed) spectra ($\lambda_{exc} = 446$ nm) of $[\text{Ru}(\text{bpy})_3]^{2+}$ in CH_3CN ((298 ± 3) K, 1 atm N_2).

through spin-orbit coupling; thus, the use of spin labels is an approximation. This mixing of spin character facilitates ISC, and as a result $^3\text{MLCT}$ formation occurs with $\sim 100\%$ efficiency ($\phi_{\text{ISC}} \sim 1$) at $\lambda_{exc} = 300$ nm.¹⁹⁻²¹

The luminescent $^3\text{MLCT}$ state of Ru^{II} polypyridyl complexes is actually a superposition of several states; specifically in the case of $[\text{Ru}(\text{bpy})_3]^{2+}$, low-temperature studies have established the presence of three thermally-accessible states that lie 10 cm^{-1} and 60 cm^{-1} apart, along with a fourth state of largely singlet character^{22,23} that can be

found a further $\sim 600 \text{ cm}^{-1}$ higher in energy.^{13,24-29} The relatively long lifetime of this $^3\text{MLCT}$ state, along with its ability to function as a good energy donor, electron donor and electron acceptor,¹³ makes $[\text{Ru}(\text{bpy})_3]^{2+}$ an extremely versatile reagent. In contrast to the uncertainty and debate surrounding the ultrafast dynamics that lead to its formation the available relaxation pathways for the resultant $^3\text{MLCT}$ state are well-known: (1) cooling of the excited state as it dumps energy into the solvent through low frequency vibrational modes, resulting in relaxation *via* non-radiative decay to the ground state (GS); (2) $^3\text{MLCT} \rightarrow \text{GS}$ luminescence; or (3) ligand-loss photochemistry *via* population of thermally-accessible antibonding ligand field (LF), or dd, states ($d\pi^5 d\sigma^*$)^{14,30,31} (Figure 2.5). Despite these multiple potential outcomes, the $[\text{Ru}(\text{bpy})_3]^{2+}$ excited state nonetheless persists for a long period of time ($\tau = 0.58 \mu\text{s}$ in H_2O at 25°C)³² relative to the $^1\text{MLCT}$ state; however, since the quantum yield for radiative decay (k_r) is generally low in Ru^{II} metal complexes (e.g. $\phi_m = 0.042$ for $[\text{Ru}(\text{bpy})_3]^{2+}$ in H_2O), non-radiative decay (k_n) and deactivation *via* ligand-loss photochemistry are the dominant pathways for excited state relaxation.^{14,33,34} Population of the metal-centred ^3dd excited state has been found to lead to ligand dissociation, and though this state lies higher in energy (Figure 2.5) it is thermally accessible from the $^3\text{MLCT}$ state or readily populated by ISC from the $^1\text{MLCT}$ state.¹⁴

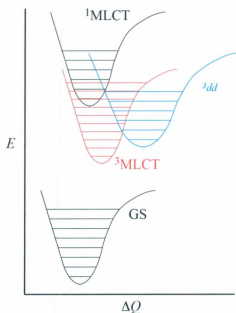


Figure 2.5 Illustration of the potential energy surfaces of the major metal-centred states of $[\text{Ru}(\text{bpy})_3]^{2+}$

2.1.2 The Role of Conformational Dynamics in Chromophoric System Design.

Recent research into the excited state dynamics of photoactive molecules is being carried out with the long-term goal of developing reliable, efficient, and inexpensive artificial photosynthetic devices. The elucidation of the mechanisms of charge and energy transfer in the excited state can lead to the rational design of chromophores or photoactive devices, with the aim of maximizing these useful properties and minimizing the effects of various types of disfavoured behavior, i.e. photodissociation. This is a non-trivial task as the mechanisms of excited state formation and relaxation are widely varied

due to the nature of the ligands and are very rapid, but considerable progress towards this goal has been achieved using synthetic modifications of the acceptor ligand.³⁴ Such control can be achieved in a number of ways, examples of which include: selecting appropriate ligands to produce a metal complex with non-zero absorbance across the whole visible range (a so-called "black" chromophore);³⁵ synthesis of a "panchromatic" sensitizer dye for use in dye-sensitized solar cells;³⁶ inhibition of dd state intervention and subsequent enhancement of radiative decay rates upon introduction of a Ru^{II} polypyridyl chromophore into a rigid matrix;³⁷ or influencing the excited state behaviour of a chromophore through synthetic means (such as by using steric hindrance to inhibit decay by an otherwise favourable pathway).³⁸

Designing systems with the intention of exploiting conformational dynamics as their mechanism of control is not a trivial endeavor, requiring careful and rational design to create a chromophore with the desired excited state properties. Efforts to study these effects by Wasielewski *et al.* relied on studying the mechanism for charge separation in different donor-acceptor pairs with increasingly-long oligo-*p*-phenylenevinylene bridges (Figure 2.6), where it was found that a distance-dependent superexchange charge transfer mechanism at short distances was superseded by a bridge-mediated hopping mechanism in longer chain lengths, and that conformational effects within the bridge attenuated electron transfer, impeding their utility in charge separation applications.³⁹

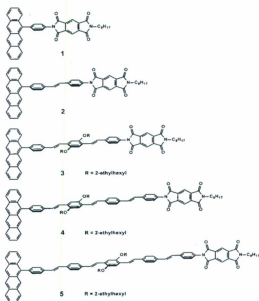


Figure 2.6 Use of increasingly long oligo-*p*-phenylenevinylene (OPV) bridges to separate a tetracene (TET) electron donor from a pyromellitimide (PI) electron acceptor.³⁹

More success was reported in research carried out by Damrauer's group that studied the rates of photoinduced electron transfer in $[\text{Ru}(\text{bpy})_2(\text{bpy}-\phi\text{-MV})](\text{PF}_6)_4$ and $[\text{Ru}(\text{tmb})_2(\text{bpy}-\phi\text{-MV})](\text{PF}_6)_4$ ($\text{tmb} = 4,4',5,5'$ -tetramethyl-2,2'-bipyridine, $\phi =$ phenylene spacer, MV = methyl viologen) (Figure 2.7), where the rate of electron transfer was found to be nearly identical for both complexes, despite there being a 100 mV increase in the driving force in the tmb-based complex, indicating that the forward transfer process was "barrierless" (Figure 2.8).

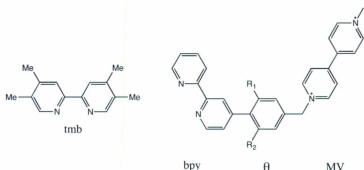


Figure 2.7 Structures of the ligands used in Damrauer's study. Three types of spacer were used ($R_1=R_2=H$, $R_1=R_2=CH_3$, $R_1=H$ and $R_2=CH_3$) to alter the degree of steric inhibition of planarization of the MV and bpy groups.³⁸

Following Marcus theory (see **Chapter 1**), the Gibbs energy for electron transfer (ΔG°) and the total reorganization energy (λ_e) must be in a regime where $\Delta G^\circ \sim \lambda_e$. Damrauer achieved this by excited-state electron delocalization in the ³MLCT states, which is a consequence of conformational changes in the ligands.³⁸ This was followed up by DFT studies by the same group, which found that the torsional angle between the bipyridine ligand and the pendant aryl substituent increases with the addition of steric bulk in the ground state in the gas-phase, but that upon formation of the excited state a significant reduction in the magnitude of torsional angle was observed. Once again, this scaled with increasing steric bulk in the chromophoric ligand and was due to the attempted planarization of the aryl group upon excited state delocalization. Interestingly, this forced quasi-planarization yields a state that is no longer in the ideal molecular or electronic configuration for back electron transfer. Reversal of this planarization is a necessary step

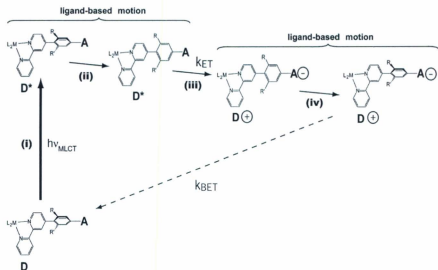


Figure 2.8 Conformational gating in an intramolecular donor-acceptor pair: charge trapping by using sterics to attenuate back-electron transfer.⁴⁰

to back electron transfer and relaxation to the ground state (Step (iv) in **Figure 2.8**) but it was found that increasingly bulky groups inhibit this process, leading to greatly enhanced forward/backward electron transfer rate ratios.⁴⁰ Ultimately, exploitation of this “conformational gating” effect manifested itself as an 8-fold increase in charge separation lifetime across the series of chromophores prepared through the systematic introduction of methyl groups to increase the overall steric bulk of the molecule, illustrating the potential versatility and utility that could be gained from careful consideration of these conformational dynamic effects.

Other research⁴¹ has confirmed the intuitive assumption that conformational changes can have a profound impact on excited state effects, such as intramolecular electron

transfer. The angle of rotation of 47° between two pyridyl rings of *N*-methyl-4,4'-bipyridinium cation (MQ⁺) in [(bpy)Re(CO)₃(MQ⁺)](PF₆)₂ creates a barrier to the favoured bpy-to-MQ⁺ excited state interligand electron transfer (ILCT) reaction, as excitation of the MQ⁺ ligand requires planarization of these rings to establish good electronic overlap and coupling. By freezing this complex in a glass the planarization is inhibited and the MQ⁺-based emission is no longer observed; excitation under the same conditions as in solution causes an ILCT between MQ⁺ and bpy (that is, the reverse of what is observed in solution) and ultimately results in bpy-based emission. Similar effects have also been reported in studies of solute-solvent interactions of a host of 5,5'-derivatized 2,2'-bipyridines.⁴²

2.2 Experimental Details.

2.2.1 Materials.

Acetonitrile (CH₃CN) (UV B&J Brand grade; Honeywell Burdick & Jackson), anhydrous ethanol (EtOH) (purchased from Commercial Alcohols Ltd.), butyronitrile (*n*-PrCN) and propionitrile (EtCN) (purum grade, $\geq 99.0\%$ by GC; Fluka), methanol (MeOH), methylene chloride (CH₂Cl₂), and chloroform (CHCl₃) (ACS grade; ACP) were used as supplied for all spectroscopic analyses. Poly(methyl methacrylate) (PMMA) (average molecular weight $\sim 966,000$ by GPC; Aldrich), coumarin-450 laser dye (99.9%; Exciton, Inc.), acetonitrile-*d*₃ and methylene chloride-*d*₂ ampoules (Cambridge Isotope Labs) were all used as received.

2.2.2 Synthesis.

The syntheses of the compounds studied in this work were accomplished at the American University in Beirut (AUB) by Dr. Tarek Ghaddar's research group using reported procedures.⁴³⁻⁴⁵ The dendritic poly(phenylenevinylene) aldehydes $G_n\text{-CHO}$ ($n = 0 - 3$),⁴³ 5,5'-bis(diethylmethylphosphonate)-2,2'-bipyridine,⁴⁴ and ruthenium bisbipyridine dichloride $(\text{Ru}(\text{bpy})_2\text{Cl}_2)^{44,46}$ were used to prepare the dendritic 5,5'-derivatized-2,2'-bipyridines ($G_n\text{-bpy}$, $n = 0 - 3$) and the resultant Ru^{II} polypyridyl complexes ($[\text{Ru}(\text{bpy})_2(\text{G}_n\text{-bpy})](\text{PF}_6)_2$ ($n = 0 - 3$), hereupon referred to as RuD_n) as delineated in Figures 2.9 - 2.12.

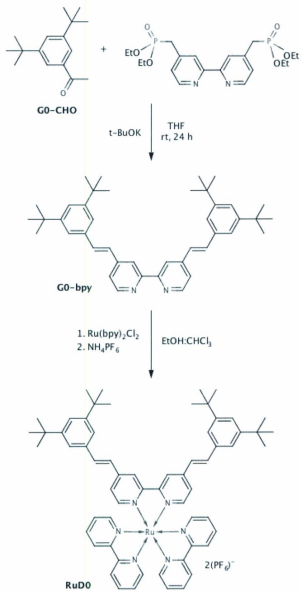


Figure 2.9 Syntheses of G0-bpy and RuD0.

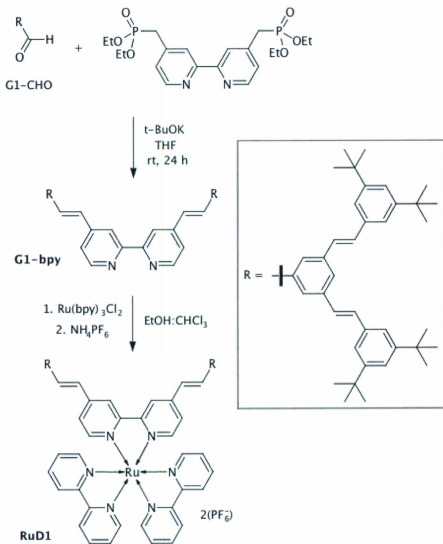


Figure 2.10 Syntheses of G1-bpy and RuD1.

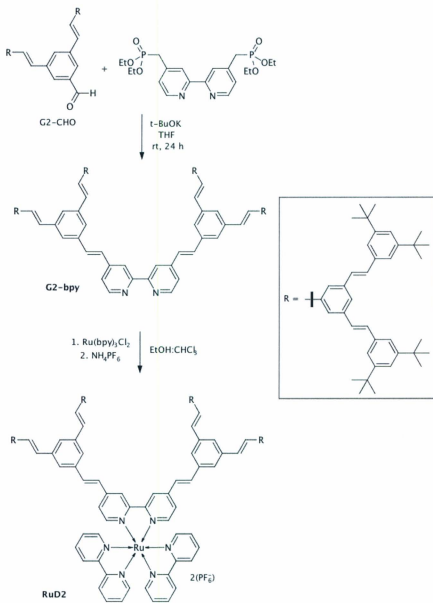


Figure 2.11 Syntheses of G2-bpy and RuD2.

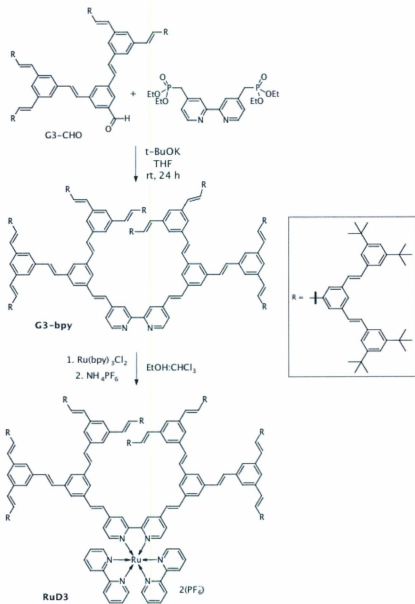


Figure 2.12 Syntheses of G3-bpy and RuD3.

2.2.3 Instrumentation and Methods.

Sample Preparation. For room temperature experiments, dendrimer sample solutions were prepared in 1.0 cm² Spectrosil quartz fluorometer cuvettes (supplied by Starna) in an appropriate solvent (either CHCl₃, CH₂Cl₂ or CH₃CN, as indicated) with absorbances below 0.15 at the excitation wavelength, unless otherwise stated. These solutions were sparged with N₂ for at least 20 minutes to reduce the concentration of dissolved O₂.

For temperature-dependent studies, sample solutions were prepared in ~1 cm pathlength rounded quartz tubes (~320 nm cutoff) of a local design. Solutions were prepared by adding the solid dendrimer compound to either 4:1 (v/v) EtOH/MeOH or 4:5 (v/v) *n*-PrCN/EtCN solutions until the appropriate concentration was reached.

Glass-supported films were prepared by dissolving 6 g of PMMA in 30 mL of CHCl₃ followed by 1 h of magnetic stirring. A pre-calculated amount of dendrimer was added to this solution to make a film with an absorbance of ~0.4 at 470 nm. These heterogeneous mixtures were poured onto a glass microscope slide and left for 24 h, drying to produce a thin film. Due to its slow rate of diffusion in PMMA ($D = 1 \times 10^{-8} \text{ cm}^2 \text{ s}^{-1}$), no precautions were taken to prevent excited-state quenching by O₂.⁴⁷⁻⁵¹

UV-Visible Absorbance Spectrophotometry. UV-Visible absorbance spectra were acquired using an Agilent HP8453A UV-Visible diode array spectrophotometer (190 - 1100 nm range, ± 0.5 nm precision). Spectra were collected and manipulated using Agilent's ChemStation software suite.

Luminescence Measurements. Steady-state luminescence spectra were measured using a Photon Technology International (PTI) QuantaMaster 6000 spectrofluorometer. The excitation light was provided by a 75 W Ushio xenon arc lamp, with wavelength selection provided by a Czerny-Turner $f/3.4$ grating monochromator. For fluid samples the excitation beam was directed into the front face of the cuvette through a variable slit (set at 4 nm) and the emitted light was measured at 90° to this incident beam, while for samples in a PMMA film the excitation was at a 60° angle to the surface of the film and was directed through the backside of the Pyrex support, as per Figure 2.13.

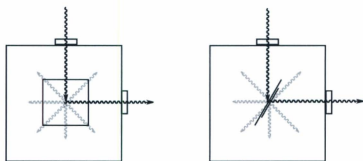


Figure 2.13 Illustration of 90° excitation of samples in solution (a, left) and 60° excitation of samples in Pyrex-supported films (b, right). Excitation of films was through the backside of the support to minimize scattering of the excitation source towards the detector.

The emitted light passed through a second 4 nm slit and Czerny-Turner $f/3.4$ grating monochromator, and was then detected by a Hamamatsu R-928 five-stage PMT (in photon-counting mode) in a PTI Model 814 PMT housing. This PMT accessory was enclosed in a Products For Research S600 PHOTOCOOL Peltier cooling device to

minimize contributions from dark current spectral artifacts. The emission spectra were corrected for instrument response and light loss using correction factors supplied by the manufacturer. Following fluorescence measurements, UV-Vis absorbance spectra were routinely acquired to monitor for spectral changes that would suggest that photochemical reactions had occurred over the course of the measurement. Spectra were acquired at a 1 nm spacing with an integration time of 1.0 s, but photosensitive compounds were analyzed using an integration time of 0.1 s with narrow excitation slit widths to minimize spectral changes.

Time-Resolved Emission Measurements. Excited state lifetimes were obtained using a PTI LaserStrobe TM-3 fluorescence lifetime spectrofluorometer that consists of a PTI GL-3300 N₂ laser with a PTI GL-302 dye laser module. The fundamental laser line ($\lambda = 337.2$ nm, 800 ps fwhm) generated from the N₂ laser was either used as the excitation source or was directed through two matched Spectrosil quartz laser dye fluorescence cuvettes mounted in the dye laser module, each containing 2.5 mM solutions of coumarin-450 in EtOH to generate the 446 nm excitation pulses. The laser was pulsed at a 10 Hz repetition rate and was directed into the sample chamber by a 40-foot fiber optic cable. Detection of the pulsed emitted radiation was at 90° to the excitation source. The signal was passed through a Czerny-Turner *f*/3.4 grating monochromator and detected by a Hamamatsu R-928 five-stage PMT in photon-counting mode.

The timings of both the laser pulse and data acquisition were controlled by a Stanford Research System Model DG535 four-channel digital delay pulse generator using a proprietary stroboscopic technique developed by PTI. The observed data is not the intrinsic fluorescence decay of the solution in question, but rather a convolution of the true fluorescence decay with the non-exponential signal produced in response to the finite temporal width of the excitation pulse. Determination of the true fluorescence decay is achieved by first acquiring the instrument response function (IRF) by use of a colloidal scattering solution. This IRF is then iteratively convoluted with a model exponential function until a satisfactory fit of the experimental data is achieved. Further analysis of deconvoluted experimental data was carried out using the data analysis software Origin Pro (OriginLab Corporation) or IGOR Pro (Wavemetrics, Inc.).

Laser Flash Photolysis. Laser flash photolysis experiments were performed using an Applied Photophysics LKS 60 laser flash photolysis spectrometer. Pulsed laser excitation was provided by a Quantel Big Sky Laser Brilliant B Nd:YAG laser ($\lambda_{exc} = 1064$ nm, 5.4 ns fwhm fundamental), using doubling and tripling non-linear optical crystals to generate 532 nm and 355 nm light. To prevent sample damage from the high intensity 532 nm light the second harmonic generator was detuned and a lens was used to defocus the excitation beam onto the sample. The sample was probed by 90° crossed-beam excitation from a monitoring beam produced from a Ushio 150 W pulsed xenon flash lamp, and the resultant transient absorption signal was directed into a variable slit-width Czerny-Turner

f/3.4 grating monochromator. Signal detection was achieved using a five-stage Hamamatsu R-928 PMT, and subsequent digitization of this signal provided by an Agilent Infiniium 54830B 600 MHz oscilloscope. The data was initially fit to an appropriate decay function using proprietary software provided by Applied Photophysics and then further analyzed using data analysis software packages. Absorption spectra were taken before and after excited state measurements to assess the photostability of the samples, which were routinely changed after minimal spectral changes were observed.

Variable Temperature Measurements. Temperature-dependent emission spectra, fluorescence decay traces and transient absorption decay traces and spectra were acquired using an Oxford Instruments Optistat DN (for solutions) or DN-V (for PMMA films) liquid nitrogen-cooled optical spectroscopy cryostat coupled to an Oxford Instruments ITC 503 Temperature Control Unit. Within the Optistat DN cryostat the fluid samples were kept in an atmosphere of N_2 inside an internal optical chamber, while the outside chamber was kept at ultrahigh vacuum ($<10^{-8}$ bar) using a Leybold BMH 70 Dry turbomolecular vacuum pump. Following each temperature change (usually in increments of 10-15 K), samples were typically allowed at least 15 minutes to thermally equilibrate. Two measurements were acquired at any given temperature following cooling as well as heating in order to monitor for hysteresis effects.

Kinetics. Kinetic analyses for samples prepared in fluid media at or near room temperature were carried out by fitting the raw data to appropriate single and/or biexponential decay functions (equations [2.1] and [2.2]). Samples prepared in a rigid medium and/or analyzed at low temperatures were initially fit using the empirical Williams-Watts/Kohlrausch (WWK) distribution function (equation [2.3])⁵²⁻⁵⁴ and biexponential decay functions,

$$I(t) = Ie^{-kt} \quad [2.1]$$

$$I(t) = I_1e^{-k_1t} + I_2e^{-k_2t} \quad [2.2]$$

$$I(t) = I_0e^{(-kt)^\beta} \quad [2.3]$$

where $I_1 + I_2 = 1$ for the biexponential decay function [2.2]. The WWK function is an empirical function used to model dielectric relaxation times in "disordered media". The underlying distribution, as reflected by the stretching exponent, β , empirically assesses the degree of distribution of states that arises from the nonexponential behaviour of MLCT states in a heterogeneous rigid medium.^{48,55-61} The average lifetime of a distribution $\langle \tau \rangle$ modeled by the WWK distribution function [2.3] is given as

$$\langle \tau \rangle = (k_1\beta)^{-1} \Gamma\left(\frac{1}{\beta}\right) \quad [2.4]$$

where the gamma function $\Gamma(n)$ is defined as

$$\Gamma(n) = \int_0^\infty x^{n-1} e^{-x} dx = \frac{1}{n} \prod_{m=1}^{n-1} \frac{\left(1 + \frac{1}{m}\right)^n}{1 + \frac{1}{m}} \quad [2.5]$$

All kinetic spectral data for RuD0 in CH₃CN and PMMA were analyzed using the ReactLab Kinetics program (Jplus Consulting). The global analysis fitting routine is based upon the method of Zuberbühler and Maeder.⁶² Briefly, this method reduces data sets of transient absorption decay traces to yield both the spectra of the individual components and rate constants for conversion between these components in accordance with a kinetics model developed by the user.^{48,63} A fitting algorithm assesses the difference between the data predicted by the model and the real data (the residual square sum) and attempts to minimize this with successive iterations. Using a form of the Levenberg-Marquardt algorithm (a method of minimizing a non-linear function across a field of parameters), this iterative process manipulates the free parameters of the kinetics model and then adjusts the calculated spectra of the coloured components to reduce the residual square sum.⁶⁴

Emission Spectral Fitting. Analysis of the MLCT spectral profiles of the dendrimer samples were carried out using a single average mode Franck-Condon line shape analysis by the following procedure.^{48,65-67} Emission spectra were converted from a scale of arbitrary counts vs. wavelength to one of quanta emitted per unit of energy by the method of Parker and Rees.⁶⁸ First, an emission data set (λ_i, y_i) (where λ_i is in nm and y_i is in arbitrary units) with an emission maximum λ_{\max} and minimum λ_{\min} is converted from an abscissa of wavelength to one of wavenumbers by:

$$\left(\frac{1}{\lambda}\right) \times 10^7 \quad [2.6]$$

The spectrum is then corrected for baseline by

$$y_i' = y_i - y_{\min} \quad [2.7]$$

The intensity of emission is also corrected for losses in signal due to slit width effects, which are proportional to the square of the wavelength:

$$y_i^c = y_i' \times \lambda_i^2 \quad [2.8]$$

Room temperature spectra were fit by a one-mode Franck-Condon analysis with a least squares program based on a Simplex algorithm written by J. P. Claude.⁶⁹ Room temperature emission spectra were modeled by the one-mode fitting equation [2.9]⁷⁰⁻⁷²:

$$I(\bar{\nu}) = \frac{I_v(\bar{\nu})}{I_0} = \sum_{v_M=0}^5 \left\{ \left(\frac{E_0 - v_M \hbar \omega_M}{E_0} \right)^3 \left(\frac{S_M^{v_M}}{v_M!} \right) \exp \left[-4 \ln(2) \left(\frac{\bar{\nu} - E_0 + v_M \hbar \omega_M}{\Delta \bar{\nu}_{0,1/2}} \right)^2 \right] \right\} \quad [2.9]$$

where $I(\bar{\nu})$ is the intensity of emission at the energy $\bar{\nu}$ in cm^{-1} relative to the intensity of the $v' = 0 \rightarrow v = 0$ transition, $\bar{\nu}$ is the energy abscissa in wavenumbers, E_0 is the energy gap between the zeroth vibrational levels of the ground and excited states, v_M is the vibrational quantum number and $\hbar \omega_M$ is the quantum spacing of averaged coupled vibrational modes of medium frequency; $\Delta \bar{\nu}_{0,1/2}$, the full width for individual vibronic lines at half-maximum height, includes contributions from solvent and low-frequency

vibrational modes, treated classically as per equation [2.10],

$$(\Delta v_{e,1/2})^2 = (\Delta v_o)^2 + \lambda_o 16k_o T \ln 2 \quad [2.10]$$

S_M , the Huang-Rhys factor (equation [2.11]), is a unitless parameter that reflects the geometric distortion along averaged medium-frequency quantum modes,

$$S_M = \frac{M\omega}{2\hbar}(\Delta Q)^2 \quad [2.11]$$

where M is the reduced mass of the vibrating system, ω is the frequency of vibration and ΔQ is the nuclear displacement.

The procedure for one-mode spectral fitting of room temperature data uses a fixed value of $\hbar\omega$ to yield values for S_M , E_0 and $\Delta\bar{v}_{1/2}$. In the fits, $\hbar\omega$ was fixed at 1300 cm^{-1} (based on $\hbar\omega$ for $[\text{Ru}(\text{bpy})_3]^{2+}$) while E_0 , S_M , and $\Delta\bar{v}_{1/2}$ were allowed to vary until a minimum was found in the squared sum of the residuals. Using these optimized values for E_0 , S_M , and $\Delta\bar{v}_{1/2}$, additional fits were run while varying the value of $\hbar\omega_M$ until the squared sum of the residuals was again minimized. After having determined an optimal value for $\hbar\omega$ a number of different initial values of E_0 , S_M , and $\Delta\bar{v}_{1/2}$ were used to check the uniqueness of fit and avoid a local minimum on the error surface.

Experimental Details for AUB. NMR spectra acquired by Dr. Ghaddar's group at AUB were carried out on a Bruker AM 300 MHz spectrometer. MALDI-TOF measurements were carried out at Georgia Tech Research Corporation (Atlanta, GA, USA) in positive ion mode with a concentration of 10 mg/mL, using α -cyanohydroxycinnamic acid (CHCA, 10 mg/mL) as the matrix. UV-Visible spectra were acquired on a Jasco V-570 UV-Vis/NIR spectrophotometer, while luminescence spectra were recorded on a Jobin Yvon Horiba Fluorolog-3 spectrofluorometer.

2.3 Results.

2.3.1 Absorbance Spectra of Gn -bpy ($n = 0 - 3$).

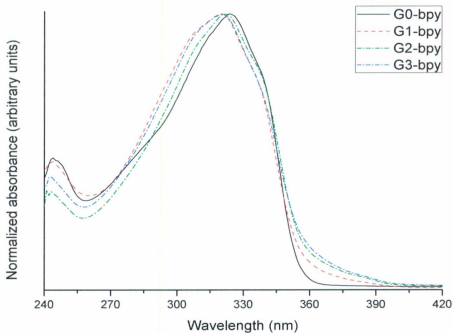


Figure 2.14 Absorbance of Gn -bpy ($n = 0 - 3$) in CHCl_3 ((298 ± 3) K, 1 atm N_2). Spectra were normalized relative to their wavelength of maximum absorbance.

The absorption spectra of the Gn -bpy dendrimers in CHCl_3 are shown in Figure 2.14, while the wavelengths of maximum absorbance in CHCl_3 and CH_2Cl_2 (CH_2Cl_2 data acquired at AUB) are listed in Table 2.1. With increasing dendrimer generation n there is an increase in the apparent extinction coefficient and a shift of λ_{max} towards the higher energy in accordance with an exponential increase in the number of stilbenoid moieties,

which scales by $(2^{(n-1)})!$ (i.e. 2, 6, 14, 30). G0-bpy in CHCl_3 exhibits a strong $\pi \rightarrow \pi^*$ absorbance at $\lambda_{\text{max}} = 323 \text{ nm}$ ($31,000 \text{ cm}^{-1}$) with shoulders at 280 nm ($35,700 \text{ cm}^{-1}$) and 345 nm ($29,000 \text{ cm}^{-1}$), while the remaining dendrimers show $\lambda_{\text{max}} = 320 - 321 \text{ nm}$ ($31,300 - 31,200 \text{ cm}^{-1}$).

Table 2.1 Absorbance data for G*n*-bpy in CHCl_3 and CH_2Cl_2 .

	$\lambda_{\text{max}}^{\text{abs}}, \text{nm}$ ($E_{\text{abs}}, \text{cm}^{-1}$)	
	CHCl_3	CH_2Cl_2
G0-bpy	323 (31,960)	-
G1-bpy	320 (31,250)	322 (31,060)
G2-bpy	321 (31,150)	320 (31,250)
G3-bpy	320 (31,250)	318 (31,450)

2.3.2 Absorbance Spectra of RuD*n* ($n = 0 - 3$) in Fluid Media.

The absorption spectra of RuD*n* ($n = 0 - 2$) in CH_3CN are shown in Figure 2.15. Distinctive features can be observed at $\lambda = 290, 317, \sim 355$ and 464 nm ($34,500, 31,500, \sim 28,200$ and $21,600 \text{ cm}^{-1}$) for RuD1 and RuD2. The smallest dendrimer RuD0 lacks a prominent absorbance band at 317 nm, but exhibits a peak at 344 nm ($29,100 \text{ cm}^{-1}$) that is only detectable as a low-energy shoulder in the larger dendrimers. The absorbance at 317 nm that is absent in RuD0 grows quickly with increasing generation relative to the other bands, allowing the assignment of this transition as a dendritic ligand-based $\pi \rightarrow \pi^*$ band. The peak at 290 nm is ascribed to a bipyridine-localized [$\pi_1 \rightarrow \pi_2^*$] transition, while the 464 nm feature is assigned to a $[(d\pi)^{\delta} \rightarrow {}^1[(d\pi)^{\delta}(\pi_1^*)^{\delta}]]$ ¹MLCT transition. The band at 344 nm is tentatively assigned (in comparison to $[\text{Ru}(\text{bpy})_3]^{2+}$) as a higher-lying

$[(d\pi)^6] \rightarrow {}^1[(d\pi)^5(\pi_2^*)^1]$ absorbance band, while the small peaks at 244 and 255 nm ($41,000$ and $39,200$ cm^{-1}) are tentatively assigned as high energy MLCT absorbances.¹² These bands experience some solvatochromism (Table 2.2), and the relative intensities of these absorbances are also solvent dependent (Figure 2.16); these features are briefly addressed in Section 2.5.2.

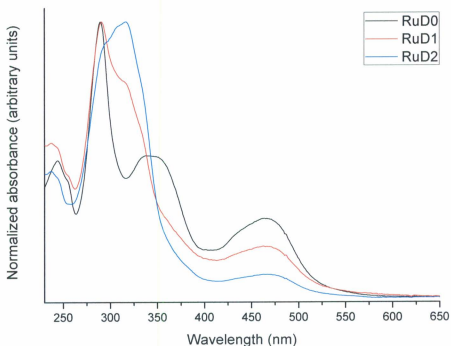


Figure 2.15 Absorption spectra of RuD0 – RuD2 in CH_3CN ((298 ± 3) K, 1 atm N_2). Spectra were normalized relative to their wavelength of maximum absorbance.

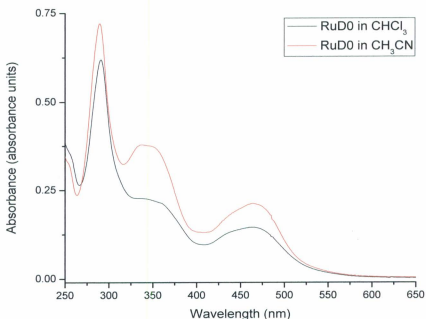


Figure 2.16 Absorbance spectra of RuD0 in CHCl_3 (black) and CH_3CN (red) (298 ± 3 K, 1 atm N_2). Spectra were normalized relative to their wavelength of maximum absorbance.

2.3.3 Absorbance Spectra of RuD n ($n = 0 - 3$) in a Rigid Medium.

The absorption spectra of RuD n ($n = 0 - 3$) in PMMA are shown in Figure 2.17, normalized to the maximum of the $(d\pi_{Ru})^{\delta} \rightarrow [(d\pi_{Ru})^{\delta}(\pi^*_{Dpp})^{\delta}]$ absorbance band. The greater concentrations of dendrimer complexes used in the preparation of these films yields the strong absorbance extending up to ~ 375 nm ($26,700 \text{ cm}^{-1}$) in RuD0-RuD2 and up to ~ 400 nm ($25,000 \text{ cm}^{-1}$) in RuD3. As listed in Table 2.2, the wavelengths of maximum absorbance of these dendrimers show the same relative insensitivity to the solvent medium in a rigid PMMA matrix as in fluid solution.

Table 2.2 Absorbance data for RuDn in CH₂Cl₂, CHCl₃, CH₃CN, and PMMA.

	$\lambda_{\text{max}}^{\text{abs}}, \text{nm} (E_{\text{abs}}, \text{cm}^{-1})$			
	CH ₂ Cl ₂ ¹	CHCl ₃	CH ₃ CN	PMMA
RuD0	-	291 (34,360) 336 (29,760) 361 (27,700) 463 (21,600)	290 (34,480) 337 (29,670) 352 (28,410) 465 (21,510)	345 (28,990) 467 (21,410)
RuD1	294 (34,010) 320 (31,250) 470 (21,280)	290 (34,480) 318 (31,450) 366 (27,320) 468 (21,370)	291 (34,360) 313 (31,950) 332 (30,120) 355 (28,170) 464 (21,550)	464 (21,550)
RuD2	294 (34,010) 320 (31,250) 470 (21,280)	-	297 (33,670) 317 (31,550) 331 (30,210) 414 (24,150) 466 (21,460)	462 (21,650)
RuD3	320 (31,250) 470 (21,280)	322 (31,060) 429 (23,310)	-	466 (21,460)

¹ Data acquired at AUB.

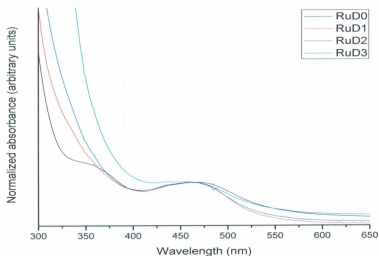


Figure 2.17 Absorbance spectra of RuDn ($n = 0 - 3$) in PMMA ((298 ± 3) K, 1 atm N₂). Spectra were normalized relative to $\lambda_{\text{max}}^{\text{abs}}$ at ~ 465 nm.

2.4 Excited States.

2.4.1 Photochemistry.

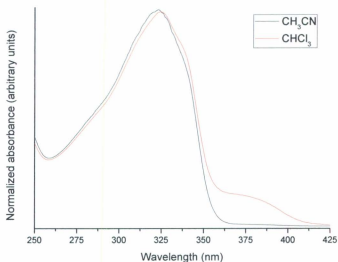


Figure 2.18 Comparison of absorbance spectra of G0-bpy in CH₃CN and CHCl₃ ((298 ± 3) K, 1 atm N₂). The transition at ~375 nm is assigned to *cis*-G0-bpy. See text for details.

The intensity of a small band at ~375 nm in the absorbance spectrum of G0-bpy was found to be dependent upon the exposure of the sample to light prior to measurement. This peak is more prominent in the larger *Gn*-bpy dendrimers. In CH₃CN the absorbance spectrum of G0-bpy shows rather little difference from that in CHCl₃ ($\lambda_{max} = 323$ nm ($E_{abs} = 31,000$ cm⁻¹)) though the small absorbance at 375 nm is no longer present (see Figure 2.18). Sustained irradiation of the major absorbance band of the *Gn*-bpy dendrimers yields rapid “quasi-reversible” changes in the absorbance spectra, depleting the primary absorbance band while causing growth of this 375 nm feature (Figure 2.19).

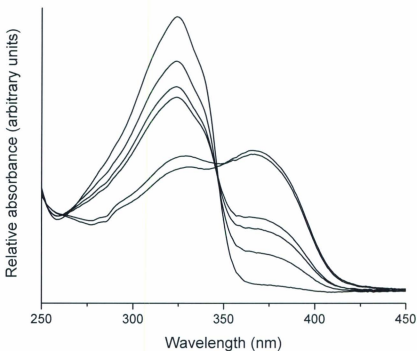


Figure 2.19 Changes in absorption of G0-bpy in CHCl_3 upon extended photolysis ($\lambda_{exc} = 355 \text{ nm}$) using an Nd:YAG laser source ($(298 \pm 3) \text{ K}$, 1 atm N_2). (In decreasing order at 325 nm: G0-bpy in CHCl_3 ; 1, 2, 6, 17 and 27 laser shots.)

In order to assess the reversibility of these spectral changes, the absorbance spectrum of a freshly prepared and sparged solution of G3-bpy in CHCl_3 was acquired prior to this solution being subjected to repeated and prolonged 322 nm ($31,100 \text{ cm}^{-1}$) excitations. This compound was stored in the dark overnight, and the absorbance spectrum was reacquired after 15 minutes of sparging on the following day (Figure 2.20). Prolonged photolysis times led to a general loss of absorbance at 322 nm, a much stronger

absorbance at 250 – 280 nm ($40,000 - 35,700 \text{ cm}^{-1}$), and increased baseline absorbance at longer wavelengths relative to the fresh G3-bpy solution. Changes were observed in the absorbance band envelope, where the slight shoulder peaks at 310 nm ($32,300 \text{ cm}^{-1}$) and 335 nm ($29,900 \text{ cm}^{-1}$) are more prominent due to a decrease in the relative intensity of the λ_{max} peak of 322 nm, which is slightly blue-shifted to 319 nm ($31,300 \text{ cm}^{-1}$) in the aged solution.

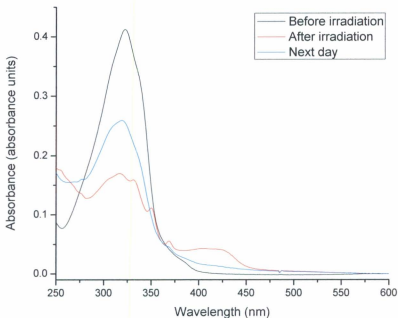


Figure 2.20 Absorption spectra of G3-bpy in CHCl_3 ($(298 \pm 3) \text{ K}$, 1 atm N_2). Black line: Fresh solution. Red line: Spectrum following prolonged 322 nm excitations. Blue line: After storage for 24 hours in the dark.

As the first photoinduced conversion is facile, it seems reasonable to assume that the inconsistent detection of this 375 nm band was due to the method of preparation, handling and storage, and "freshness" of the dendrimer solution. These spectral changes are made up of two distinct processes as indicated by the observation of two isosbestic points; one at ~350 nm and another at ~355 nm. The loss of the first isosbestic point at 350 nm and appearance of the second point at ~355 nm occurred only following sustained irradiation, suggesting that a new photochemical process (addressed in the Discussion) is responsible for the irreversible changes. These observations were not further investigated.

2.4.2 Emission Spectra.

2.4.2.1 Fluorescence of *Gn*-bpy in Fluid Media.

Excitation of the $^1[\pi \rightarrow \pi^*]$ absorption band of the *Gn*-bpy dendrimers in CHCl_3 results in singlet fluorescence as shown in Figure 2.21, while the wavelengths of maximum emission intensity in CHCl_3 and CH_2Cl_2 are summarized in Table 2.3. In contrast to the increase in extinction coefficients with increasing dendrimer generation, the fluorescence quantum yield in CH_2Cl_2 was qualitatively found to decrease, while $\lambda_{\text{max}}^{\text{em}}$ became slightly blue-shifted from *G1*-bpy to *G3*-bpy. The fluorescence bands of *G2*-bpy and *G3*-bpy also show two peaks, versus the one peak seen in *G0*-bpy and *G1*-bpy.

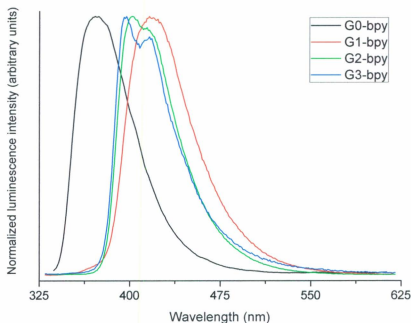


Figure 2.21 Normalized and corrected fluorescence spectra of the G_n -bpy ($n = 0 - 3$) dendrimers in CHCl_3 ((298 ± 3) K, 1 atm N_2).

Table 2.3 Luminescence data for G_n -bpy in CHCl_3 , CH_2Cl_2 and 4:5 (v/v) n -PrCN/EtCN.

	$\lambda_{\text{max}}^{\text{em}}$, nm (E_{em} , cm^{-1})		$\lambda_{\text{max}}^{\text{em}}$, nm (E_{em} , cm^{-1})
	CHCl_3	CH_2Cl_2	4:5 (v/v) n -PrCN/ EtCN + 10% EtI
G0-bpy	372 (26,880)	-	-
G1-bpy	417 (23,980)	420 (23,810)	594 (16,840)
			654 (15,290)
G2-bpy	402 (24,880)	400 (25,000)	600 (16,670)
			639 (15,650)
			664 (15,060)
G3-bpy	396 (25,250)	394 (25,380)	604 (16,560)
			642 (15,580)
			666 (15,020)

The emission spectra were normalized to account for photoinstability of these compounds in the solution phase; accordingly, their quantum yields were not measured. Initial changes in the emission spectra upon irradiation were quite pronounced but still reversible, though with sustained irradiation some irreversible changes were detected. The presence of isoemissive points and reversible spectral changes suggest that photoisomerization occurs, while the irreversible changes indicate that a slow second reaction pathway takes place. Time-resolved fluorescence of **G0-bpy** in degassed CH_2Cl_2 solution showed biphasic kinetics, where a rapid initial component with an observed lifetime of $\tau_{1,\text{obs}} \sim 15$ s was followed by a much slower ($\tau_{2,\text{obs}} \sim 1$ h) decay (Figure 2.22).

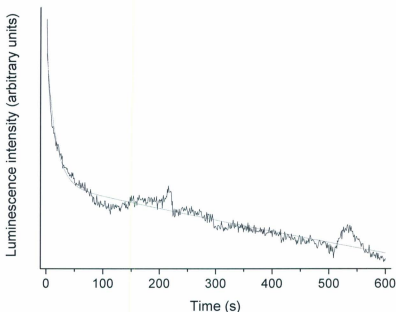


Figure 2.22 Luminescence decay of **G0-bpy** in CH_2Cl_2 upon sustained 363 nm irradiation ((298 ± 3) K, 1 atm N_2). ($\tau_1 \sim 15$ s, $\tau_2 \sim 1$ h).

2.4.2.2 Variable Temperature Phosphorescence Spectra.

Experiments carried out at AUB demonstrated that the *G_n-bpy* chromophores do not phosphoresce at 77 K in 4:5 (v/v) *n*-PrCN/EtCN. However, the introduction of EtI enhances the rate constant for intersystem crossing, leading to weak phosphorescence (Figure 2.23).⁷³ In contrast to the blue-shift in the room-temperature fluorescence spectra, the phosphorescence of the *G_n-bpy* dendrons was observed to red-shift with increasing generation (summarized in Table 2.3). To the best of our knowledge, this is the first known observation of phosphorescence in poly(phenylenevinylene) dendrimers.

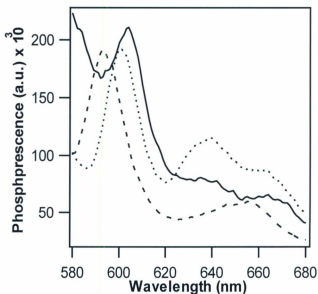


Figure 2.23 Phosphorescence spectra of: (dashed) *G*₁-bpy, (dotted) *G*₂-bpy and (solid) *G*₃-bpy in 10% EtI in 4:5 (v/v) *n*-PrCN/EtCN at 77 K ($\lambda_{exc} = 320$ nm). Figure provided by Dr. Tarek Ghaddar at AUB.

2.4.2.3 Luminescence Spectra of RuDn (n = 0 – 3) in CH₃CN at Room Temperature.

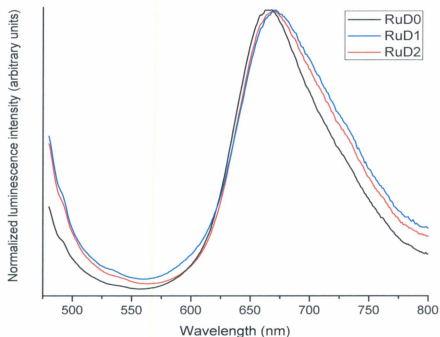


Figure 2.24 Corrected luminescence spectra of RuDn ($n = 0 - 2$) in CH₃CN upon excitation of $\lambda_{\text{max}}^{\text{abs}}$ of the $[(d\pi)^6] \rightarrow {}^1[(d\pi)^5(\pi^*)^1]$ absorbance bands (see Table 2.2) ((298 ± 3) K, 1 atm N₂).

Steady-state luminescence spectra of RuDn ($n = 0 - 2$) in CH₃CN are shown in Figure 2.24, demonstrating that the luminescence of these compounds is virtually invariant with increasing dendrimer generation. Excitation into each of the bpy-based $[\pi \rightarrow \pi^*]$, stilbene-based $[\pi \rightarrow \pi^*]$ or $[(d\pi)^6] \rightarrow {}^1[(d\pi)^5(\pi^*)^1]$ absorption bands yields varying degrees of ³MLCT emission (Figure 2.25), indicating that ligand-centred excitation initially leads to sensitization of the ¹MLCT state and then, following

intersystem crossing, population of the $^3\text{MLCT}$ state. Interestingly, some degree of ligand-based emission is also visible at ~ 385 nm, suggesting that RuD0 is a weak dual emitter (this ligand-based emission was not investigated in the larger dendrimers). $^3\text{MLCT}$ emission is quenched in these dendrimers relative to the intensity of fluorescence of the free ligand, as shown in the luminescence of G1-bpy and RuD1 in CH_2Cl_2 in Figure 2.26.

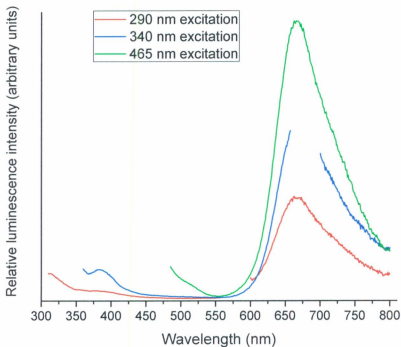


Figure 2.25 Corrected luminescence spectra of RuD0 in CHCl_3 upon 290, 340 and 465 nm excitations ((298 ± 3) K, 1 atm N_2). The break in the spectrum from $\lambda_{\text{em}} = 660 - 700$ nm is due to the second harmonic of the excitation light ($\lambda_{\text{exc}} = 340$ nm).

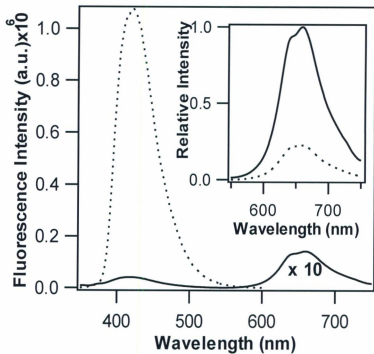


Figure 2.26 Steady state luminescence of G1-bpy and RuD1 in CH₂Cl₂ upon 320 nm excitation. RuD1 (solid) emission magnified 10x relative to G1-bpy (dotted). Inset: Relative luminescence intensity of RuD1 in CH₂Cl₂ upon 320 nm (dotted) and 470 nm (solid) excitation. Figure provided by Dr. Tarek Ghaddar at AUB.

2.4.2.4 Luminescence Spectra of RuD n ($n = 0 - 3$) in PMMA at Room Temperature.

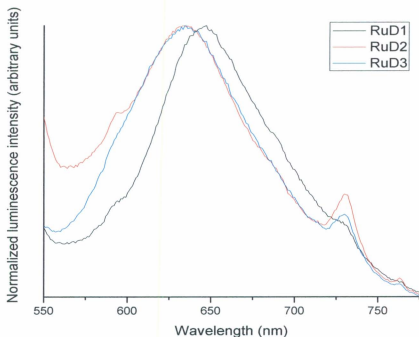


Figure 2.27 Corrected luminescence spectra of RuD n ($n = 1 - 3$) in PMMA upon excitation of $\lambda_{\text{max}}^{\text{abs}}$ of the $[(d\pi)^0] \rightarrow {}^1[(d\pi)^2(\pi^*)^1]$ absorbance bands (see Table 2.2) ((298 ± 3) K, 1 atm N $_2$).

Normalized luminescence spectra of RuD n ($n = 1 - 3$) in PMMA resulting from 464 nm excitation are shown in Figure 2.27. Whereas the luminescence maxima were found to be rather invariant with respect to dendrimer generation in both CHCl $_3$ and CH $_3$ CN (Table 2.4), in a rigid medium the spectra of RuD2 and RuD3 are blue-shifted by 290 cm $^{-1}$ (12 nm) relative to RuD1. Care must be taken to ensure that the fluorescence of the dendrimers is not convoluted with that of the PMMA matrix at $\lambda_{\text{em}} = 482$ nm. The

Table 2.4 Luminescence data for RuD*n* in CH₂Cl₂, CH₃CN and PMMA.

	$\lambda_{\text{max}}^{\text{em}}, \text{nm} (E_{\text{em}}, \text{cm}^{-1})$		
	CH ₂ Cl ₂	CH ₃ CN	PMMA
RuD0	654 (15,290)	667 (14,990)	
RuD1	652 (15,340)	671 (14,900)	647 (15,460)
RuD2	652 (15,340)	670 (14,930)	635 (15,750)
RuD3	652 (15,340)	-	635 (15,750)

emission spectra in PMMA are somewhat blue-shifted compared to those spectra acquired in CH₂Cl₂ (between 120 – 410 cm⁻¹) and significantly blue-shifted relative to those in CH₃CN (between 560 – 820 cm⁻¹).

While the RuD*n* dendrimers are more resistant to the photodegradative changes observed in the free ligands in solution, this effect becomes less pronounced with increasing dendrimer generation (that is, as the complex becomes more “ligand-like”). This reactivity also appears to be medium dependent, as the absorbance and luminescence of RuD0 remain rather constant with prolonged irradiation in CH₃CN but are susceptible to changes under the same conditions in CHCl₃. However, encasing these molecules in the rigid plastic matrix PMMA prevents these changes altogether.

2.4.3 Emission Spectral Fitting.

Table 2.5 Emission spectral fitting parameters, Franck-Condon factors and reorganization energies for $[\text{Ru}(\text{bpy})_3](\text{PF}_6)_2$ in CH_3CN and PMMA, and $\text{RuD}n$ ($n = 0 - 2$) in CH_3CN ($(298 \pm 3) \text{ K}$).^a

	$[\text{Ru}(\text{bpy})_3](\text{PF}_6)_2^c$		RuD0	RuD1	RuD2
	CH_3CN	PMMA	CH_3CN	CH_3CN	CH_3CN
$\hbar\omega_M$ (cm^{-1})	1350	1350	1325	1325	1325
E_0 (cm^{-1})	16,320	16,950	$15,111 \pm 2$	$15,020 \pm 6$	$15,060 \pm 40$
S_m	1.1	1.14	0.497 ± 0.004	0.460 ± 0.01	0.46 ± 0.06
$\Delta\bar{\nu}_{1/2}$ (cm^{-1})	1750	1498	1476 ± 6	1620 ± 10	1520 ± 70
$\ln[F(\text{calc})]$	-18.63	-19.67	-25.53	-25.37	-25.33
E_{em} (cm^{-1})	16,080	16,950	15,060	14,936	14,993
D_i	36.2	3.6	36.2	36.2	36.2
D_{op}	1.81	2.22	1.81	1.81	1.81
λ_i^{MLCT} (cm^{-1}) ^b	1490	1540	658	609	603
λ_o^{MLCT} (cm^{-1})	1300	980			
μ_{ES}	14.1	14.1			
$\lambda_{0,j}$ (cm^{-1})	940	360			

^a Averaged values from fits carried out with $\hbar\omega_M = 1300$ and 1350 cm^{-1} .

^b Calculated from $\lambda_i^{MLCT} = S_M \hbar\omega_M$.⁴⁸ ^c From reference 46.

The emission spectra of $\text{RuD}n$ ($n = 0 - 2$) were analyzed by the single, average-mode Franck-Condon line shape analysis (see Section 2.2.3). The physical parameters generated by this fitting routine can be found in Table 2.5, along with those calculated for $[\text{Ru}(\text{bpy})_3]\text{Cl}_2$ in both CH_3CN and PMMA.⁴⁸ These parameters were then used to calculate the vibrational overlap factors for non-radiative decay, $F(\text{calc})$, which is displayed in logarithmic form in equation [2.12],

$$\ln[F(\text{calc})] = -\frac{1}{2} \ln \left[\frac{\hbar\omega_M E_0}{(1000\text{cm}^{-1})^2} \right] - S - \left(\frac{\gamma E_0}{\hbar\omega_M} \right) + \frac{(\gamma+1)^2 \left(\frac{\Delta\bar{\nu}_{1/2}}{\hbar\omega_M} \right)^2}{16 \ln 2} \quad [2.12]$$

where the factor of 1000 cm⁻¹ is an arbitrary scaling factor to make the logarithmic term unitless, E_0 , $\hbar\omega_M$ and $\Delta\bar{\nu}_{1/2}$ are in cm⁻¹, and γ is given in equation [2.13],⁷⁴

$$\gamma = \left(\frac{E_0}{S_M \hbar\omega_M} \right) - 1 \quad [2.13]$$

This formalism is valid in the weak coupling ($E_0 \gg S_M \hbar\omega_M$), low-temperature limit ($\hbar\omega_M \gg k_B T$), and assumes equal quantum spacings in the ground and excited states, i.e. $\hbar\omega = \hbar\omega'$. For polypyridyl complexes, S_M and $\hbar\omega_M$ are average values based on contributions from a number of mainly C=C- and C=N-based symmetrical ν_{ppy} stretching modes, while $\Delta\bar{\nu}_{1/2}$ contains the solvent reorganization and the Ru-N modes, treated classically.^{48,75,76} Initial fitting of the RuD0 ³MLCT emission spectrum yielded satisfactory results, though the calculated data did not properly represent the experimental data at higher energies. This discrepancy was surprising given the general quality of the fit, and an examination of the residual data in RuD0 showed the presence of a second low-intensity emissive contribution that was being masked by the strong ³MLCT emission (Figure 2.28, top). The shape and λ_{max} of this band were reminiscent of a Ru polypyridyl ³MLCT band, leading to the hypothesis that this emission arose from either (a) an emissive impurity or (b) a second, competitive emissive ³MLCT state. The

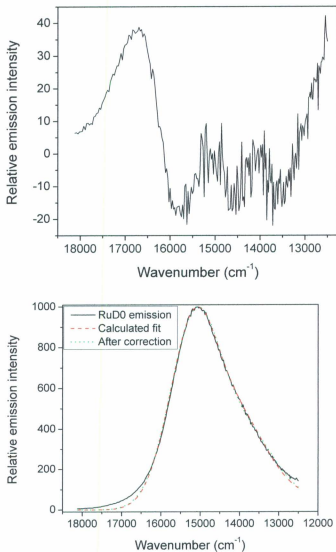


Figure 2.28 (top) Residual data from the initial fitting procedure. (bottom) Comparison of spectral fitting results of RuD0 in CH₃CN before and after spectral subtraction (procedure described in text).

$^3\text{MLCT}$ emission spectrum of $[\text{Ru}(\text{bpy})_3]^{2+}$ was appropriately scaled and subtracted from the RuD0 $^3\text{MLCT}$ emission spectrum and the resultant modified spectrum was then subjected to the spectral fitting routine, resulting in almost no change in the calculated spectral fit but a much better representation of the experimental data (Figure 2.28, bottom) as quantified by visual estimation and a reduction in both root-mean-squared deviation and in the degree of correlation between spectral fitting parameters S_M , $\Delta\bar{V}_{1/2}$ and E_0 .

2.4.4 Time-Resolved Luminescence Decay of the RuD n Dendrimers.

The luminescence decay of the $^3\text{MLCT}$ state of the RuD n dendrimers upon 446 nm excitation was assessed at multiple temperatures and in both fluid and rigid media.

2.4.4.1 Luminescence Decay in Fluid Media at Room Temperature.

The luminescence decay of RuD n in solution and rigid media at room temperature upon 446 nm excitation is summarized in Table 2.6. $^3\text{MLCT}$ luminescence decay of RuD0 in CH_3CN (Figure 2.29) shows biphasic kinetics, where a short risetime ($k_1 = (9.1 \pm 0.5) \times 10^7 \text{ s}^{-1}$, $\tau_1 = (11 \pm 2) \text{ ns}$) is followed by a longer monoexponential decay ($k_2 = (3.6 \pm 0.1) \times 10^6 \text{ s}^{-1}$, $\tau_2 = (280 \pm 10) \text{ ns}$). Similar kinetics are also found in dendrimer generations $n = 1$ and 2 (Figure 2.29), where the values for k_1 and k_2 are greater for RuD2 relative to RuD0 and greater again for RuD1 relative to RuD0.

Table 2.6 Summary of luminescence decay data from biexponential and WWK fits of RuD*n* in several solvents.

Dendrimer	Solvent		
	CH ₃ CN	4:1 (v/v) EtOH/MeOH (77 K)	PMMA
RuD0	$\tau_1 = (11 \pm 2)$ ns $\tau_2 = (280 \pm 10)$ ns	$\tau_1 = (0.22 \pm 0.17)$ μ s $\tau_2 = (15.1 \pm 1.2)$ μ s	$\beta = 0.313 \pm 0.008$
			$A_1 = 0.45 \pm 0.01$
			$\tau_1 = (0.36 \pm 0.06)$ μ s
			$A_2 = 0.55 \pm 0.02$
RuD1	$\tau_1 = (21 \pm 6)$ ns $\tau_2 = (290 \pm 10)$ ns	-	$\beta = 0.44 \pm 0.02$
			$A_1 = 0.45 \pm 0.06$
			$\tau_1 = (0.25 \pm 0.04)$ μ s
			$A_2 = 0.55 \pm 0.01$
RuD2	$\tau_1 = (19 \pm 2)$ ns $\tau_2 = (268 \pm 5)$ ns	-	$\beta = 0.37 \pm 0.02$
			$A_1 = (0.48 \pm 0.04)$
			$\tau_1 = (0.31 \pm 0.05)$ μ s
			$A_2 = (0.52 \pm 0.03)$
RuD3	-	-	$\beta = 0.30 \pm 0.01$
			$A_1 = (0.62 \pm 0.03)$
			$\tau_1 = (0.22 \pm 0.02)$ μ s
			$A_2 = (0.38 \pm 0.01)$
RuD3	-	-	$\tau_2 = (1.7 \pm 0.1)$ μ s

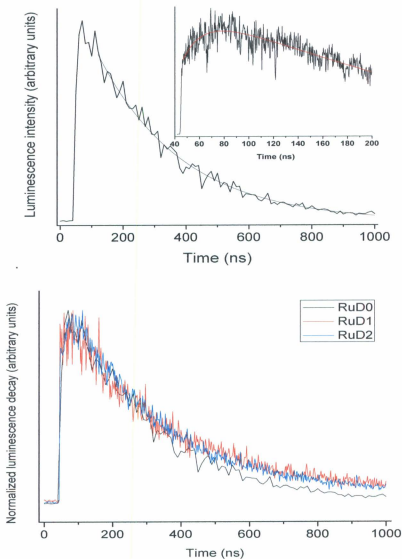


Figure 2.29 (top) Luminescence decay of RuD0 in CH₃CN (0-1000 ns timescale). **Inset:** Luminescence decay from 40-200 ns for emphasis of risetime ($\tau = (11 \pm 2)$ ns). (bottom) Luminescence decay of RuD_n ($n = 0 - 2$) in CH₃CN. All spectra acquired at (298 ± 3) K under 1 atm N₂.

2.4.4.2 Luminescence Decay in a Frozen Medium at 77 K.

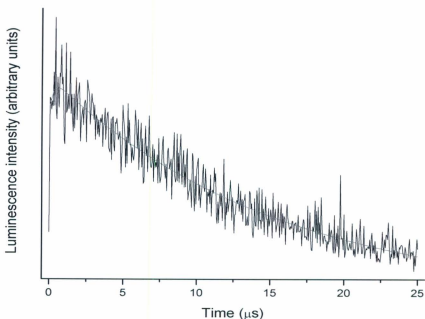


Figure 2.30 Luminescence decay of RuD0 in 4:1 (v/v) EtOH/MeOH at 655 nm upon 446 nm excitation at 77 K under 1 atm N₂.

Luminescence decay of RuD0 was acquired in 4:1 EtOH/MeOH solution at 77 K (Figure 2.30), where a dramatic enhancement of excited state lifetime ($\tau_2 = (15.1 \pm 1.2)$ μs) was observed relative to that in fluid solution at room temperature (Table 2.6), along with a 20-fold increase in the lifetime of the rapid growth kinetics ($\tau_1 = (220 \pm 17)$ ns).

2.4.4.3 Luminescence Decay in a Rigid Medium at Room Temperature.

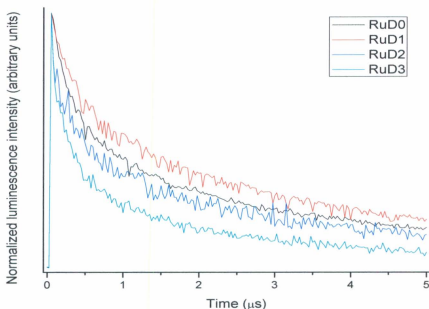


Figure 2.31 Luminescence decay of RuD_n ($n = 0 - 3$) in PMMA at 640 nm ($\lambda_{\text{exc}} = 446$ nm) ((298 ± 3) K, 1 atm N_2).

The luminescence decay of RuD_n ($n = 0 - 3$) in rigid PMMA films is displayed in Figure 2.31. Satisfactory fits of the data were achieved using both a biexponential decay model and a WWK treatment (see Experimental in Section 2.2.3), the results of which are listed in Table 2.6. The relative merits of these approaches are addressed in the Discussion. In both cases, there is a trend towards decreasing decay lifetimes and decreasing β values with dendrimer generation in the order $\text{RuD1} > \text{RuD2} > \text{RuD3}$, while RuD0 stands apart.

2.4.5 Laser Flash Photolysis.

2.4.5.1 RuD0 in a Fluid Medium at Room Temperature.

Transient absorption decay traces of RuD0 in CH₃CN upon 355 nm excitation were acquired at 5 nm intervals from 365 – 650 nm (data in Appendix B; a representative sample is shown in Figure 2.32), and the resultant time-resolved transient absorption spectra can be found in Figure 2.33. An increase in absorbance was seen from 380 – 400 nm, 500 – 580 nm, and 615 – 650 nm, which were assigned as $\pi \rightarrow \pi^*$ transitions of the bpy and dendron groups, $d\pi^* \rightarrow \pi^*$ MLCT transitions, and dendrimer-based $\pi^*-\pi^*$ transitions, respectively.⁷⁷ Losses of absorbance were observed at 445 – 495 nm and at 580 – 615 nm, due to bleaching of the ground state absorbance and to ³MLCT emission,

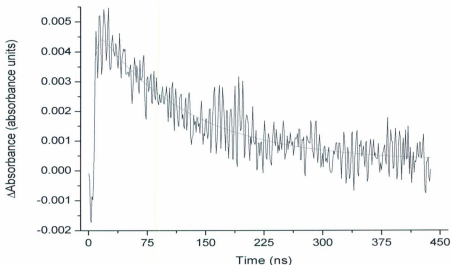


Figure 2.32 Transient absorption decay trace of RuD0 in CH₃CN at 385 nm ($\lambda_{exc} = 355$ nm) ((298 ± 3) K, 1 atm N₂).

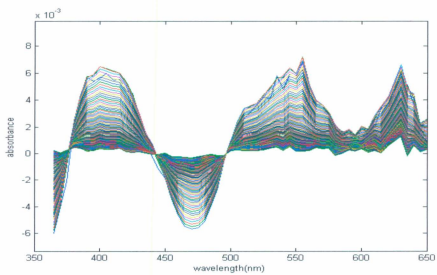
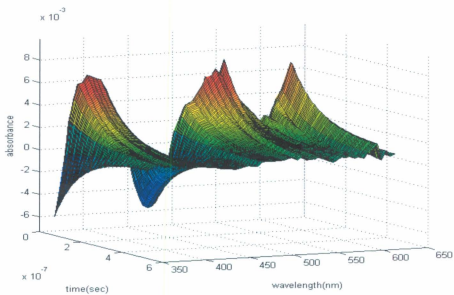


Figure 2.33 3D (top) and 2D (bottom) transient absorption spectra of RuD0 in CH_3CN ($\lambda_{\text{exc}} = 355 \text{ nm}$) ($(298 \pm 3) \text{ K}$, 1 atm N_2).

respectively. All of the transient absorbance decay traces exhibited a monoexponential decay component with a lifetime in the $\sim 110 - 150$ ns time regime, but the kinetics were wavelength dependent on short timescales. The positive absorbance decay traces at 380 – 400 nm and 500 – 650 nm also showed a fast rise time component that was reminiscent of the risetime dynamics measured in the fluorescence decay measurements; preliminary results from nonlinear curve fitting routines yielded a decay lifetime of $\tau \sim 10$ ns for this rapid component. Isosbestic points were found at 375, 440, and 495 nm, but the fact that these points lie on the $\Delta A = 0$ line indicates that isomerization or other such processes do not contribute to the observed excited state decay dynamics. A more rigorous analysis of the data was carried out by the global kinetic analysis procedure, as described in the Discussion.

2.4.5.2 RuD0 in a Rigid Medium at Room Temperature.

Transient absorption decay traces resulting from 355 nm excitation of RuD0 in PMMA were collected from 400 – 690 nm in 10 nm increments (data in Appendix B; a representative sample is shown in Figure 2.34) and the resultant time-resolved transient absorption spectra can be found in Figures 2.35a-b. The kinetics in PMMA were rather more complex than those observed in CH₃CN solution, with three separate kinetic phases observed on the nanosecond-to-microsecond timescale of this experiment.

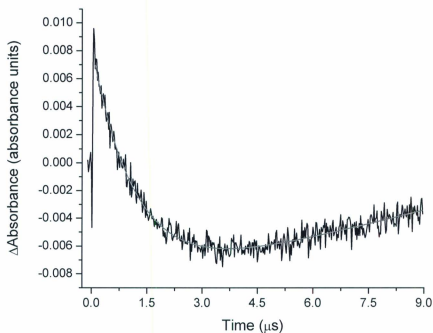


Figure 2.34 Transient absorption decay trace of RuD0 in PMMA at 400 nm ($\lambda_{exc} = 355$ nm) ((298 ± 3) K, 1 atm N_2).

As with the results acquired in CH_3CN at room temperature, an initial absorbance at 400 nm (Figure 2.34) is attributed to a $\pi \rightarrow \pi^*$ transition on a reduced bpy ligand. However, there was no prompt risetime observed at this or at any other wavelength. This absorbance feature nonetheless exhibited biphasic kinetics, with an initial decay of $\tau_1 \sim (1.19 \pm 0.03)$ μs that was succeeded by a long-lived bleach whose lifetime extends well beyond the temporal limits of the experiment. The $\pi \rightarrow \pi^*$ absorbance of the dendrimer ligand was again observed between 500 – 650 nm, showing exponential kinetics ($\tau \sim 3$ μs) with a long-lived component. The bleach of ground state MLCT absorbance exhibiting

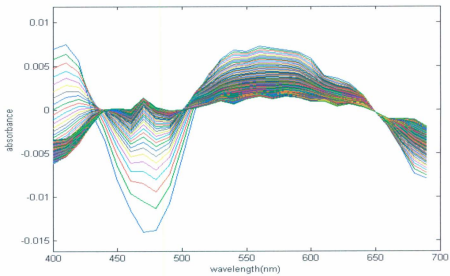
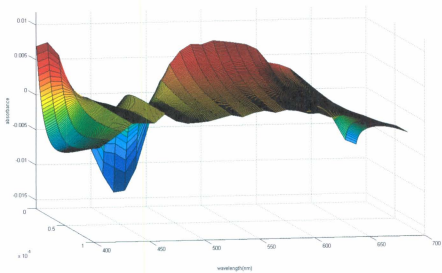


Figure 2.35 3D (top) and 2D (bottom) transient absorption spectra of RuD0 in PMMA ($\lambda_{exc} = 355$ nm) ((298 ± 3) K, 1 atm N_2).

biphasic kinetics was detected from 440 – 500 nm, with an initial component of $\tau_1 \sim 200$ – 300 ns and a second component with $\tau_2 \sim 1.0$ – 1.5 μ s.

The TA spectra in Figures 2.35a-b show a pair of isosbestic points at 440 and 500 nm that lie on the $\Delta A = 0$ line on either side of the MLCT bleach. These points are prominent at medium and longer timebases but are absent at earlier times. There is a dynamic shift in the breadth of this negative absorbance band shortly following excitation, resulting in a narrowing from ~ 430 – 510 nm to ~ 440 – 500 nm in >1 μ s. However, a third isosbestic point is observed at 650 nm that is static for the duration of the LFP experiment and that resides on the $\Delta A = 0$ line, confirming that the dynamic changes seen in the MLCT bleach are intrinsic to the sample and are not due to a photodegradative process.

2.5 Discussion.

2.5.1 Spectral Properties and Photochemistry of the *G_n*-bpy Dendrimers.

The absorption and room temperature emission spectra of the *G_n*-bpy dendrimers are unique relative to those of other previously-reported poly(phenylenevinylene) dendrimers, in that the spectral band shapes for the *G_n*-bpy dendrimers show changes as a function of dendrimer generation, while previous results showed little to no changes with dendrimer generation.^{43,78} For example, the optical properties of stilbene-containing dendrimers with a tris(styrylbenzyl)amine core demonstrate insensitivity to increasing chain length, ostensibly due to the cross-conjugation that arises from the 1,3,5-substitution pattern of

these polymers, which inhibits delocalization and causes electronic isolation of the individual stilbenoid units.⁷⁹⁻⁸² In the case of the *Gn*-bpy dendrimers, the increase in extinction coefficient with increasing dendrimer generation is merely a statistical effect, initially suggesting little evidence of electronic communication between the stilbenoid moieties of the dendrimer arms or with the bipyridine core in the ground state.

However, other results provide some evidence of electronic communication in these dendrimers, as a decrease in fluorescence energy of 2900 cm⁻¹ was observed in going from G0-bpy to G1-bpy in CHCl₃ followed by a trend towards slightly higher energies with increasing dendrimer generations. Though this seems incongruous, excluding the seemingly anomalous photophysical properties of G0-bpy from the comparison is sensible based on the fact that it has no branching stilbene moieties and has a fundamentally different structure from the first-, second- and third-generation dendrimers. This trend towards higher energies with increasing generation (above G1) has previously been observed in rigid perylene-terminated poly(phenylacetylene) dendrimers and was attributed to the enhancement of non-radiative decay with increasing size in these systems.⁸³ The initial decrease in absorbance energy is often ascribed to a stabilizing effect from some degree of excited state delocalization in G1-bpy relative to G0-bpy, but if this is correct then its decreasing prominence with increasing generation suggests that this is a short-range phenomenon that rapidly diminishes in influence as the dendrimer size increases with each successive generation. An alternative explanation for the reduction in absorbance energy is the reduction in ΔQ by equation [2.11] as the dendron becomes

more electronically delocalized, resulting in a smaller reorganization energy upon excitation relative to a less delocalized excited state that experiences more distortions (as reflected in S_M and ΔQ).

The spectroscopy of the G_n -bpy dendrimers is dictated by their sensitivity to photoinduced spectral changes, ostensibly due to *trans*-to-*cis* isomerization about the numerous stilbene moieties in these molecules. Largely reversible spectral changes with isosbestic points that slowly become irreversible with continuous irradiation (Figures 2.19 and 2.36) suggest that *cis/trans* isomerization of the stilbenoid moieties is a prominent photophysical process in these dendrimers. Decreased fluorescence intensity, changes in spectral band shapes and the observation of irreversible photochemistry are all consistent with photoconversion of the emissive *trans*-stilbene isomer to the short-lived *cis*-stilbene isomer from which photochemical side products are known to accrue (Figure 2.37).⁸⁴

Irradiation of the absorbance band at 322 nm of G3-bpy in CHCl_3 (Figure 2.36) results in pronounced photoisomerization of many of the stilbenoid groups as indicated by the thorough depletion of this band, yielding isosbestic points corresponding to the aforementioned reversible and irreversible processes. That these spectral changes are detected at all in the largest dendrimer seems to confirm the model discussed in Section 1.5.6.1; namely, that the conventional one-bond flip mechanism becomes secondary to the hula twist (HT) mechanism in increasingly bulky or rigid environments.

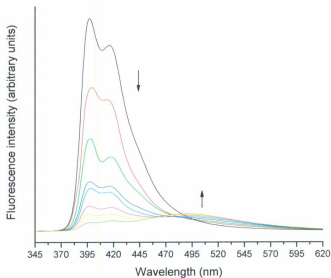


Figure 2.36 Isomerization of G3-bpy in CHCl_3 upon prolonged irradiation ($\lambda_{\text{irr}} = 322$ nm) as evidenced by changes in the corrected fluorescence spectra acquired periodically during the irradiation ((298 ± 3) K, 1 atm N_2).

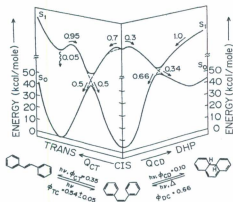


Figure 2.37 Illustration of branching ratios along the S_1 and S_0 potential energy surfaces of stilbene.⁸⁴ Reprinted with permission from Sensen *et al.*, *J. Chem. Phys.* 1993, 98, 6291. © 1993, American Institute of Physics.

2.5.2 Ground State Photophysics of the RuD n Dendrimers.

The absorbance spectral envelope of the RuD n species are superimposable in the MLCT region from one to another, beyond an increasingly significant contribution from the stilbene groups with increasing dendrimer generation, leading to larger extinction coefficients in concert with the increasing number of chromophores per molecule, akin to a dilution of the chromophores. These changes are the most pronounced for the shorter chain length dendrimers, where the significant bipyridine-localized [$\pi \rightarrow \pi^*$] transition of RuD0 in CH₃CN ($\lambda_{\text{max}}(\text{abs}) = 290 \text{ nm}$) quickly becomes overwhelmed by the growth of the stilbene-based [$\pi \rightarrow \pi^*$] band in RuD1 ($\lambda_{\text{max}}(\text{abs}) = 313 \text{ nm}$) and RuD2 ($\lambda_{\text{max}}(\text{abs}) = 318 \text{ nm}$). However, in all cases $\lambda_{\text{max}}(\text{abs})$ for the individual transitions is virtually unchanged with increasing dendrimer number.

As absorbance spectra are typically composed of many separate transitions, the composition of the absorbance spectrum of RuD0 in CH₃CN can be determined by deconvoluting the spectral envelope into a series of Gaussian peaks as shown in Figure 2.38, while the spectral characteristics of these bands and their assignments can be found in Table 2.7. With the exception of the most intense absorbance band centred at 34520 cm⁻¹ (290 nm), the remaining absorbances at ~41,050/39,250 cm⁻¹ (244/255 nm), 30,360/27,430 cm⁻¹ (330/365 nm), and 22,700/20,860 cm⁻¹ (441/479 nm) each appear to be composed of two Gaussian peaks, ostensibly due to the differing absorbances of the substituted and non-substituted bipyridine chromophores. The locations of these peaks roughly correspond with those found in the absorbance spectrum of [Ru(bpy)₃]²⁺ in

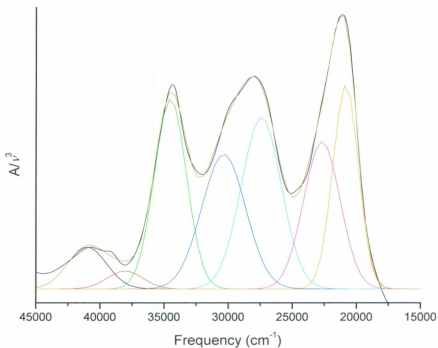


Figure 2.38 Gaussian deconvolution of the absorbance spectrum of RuD0 in CH₃CN (dark yellow line shows cumulative fit from individual peaks).

Table 2.7 Spectral characteristics of peaks determined from Gaussian deconvolution of the absorbance spectrum of RuD0 in CH₃CN.

Assignment	$E_{\text{abs}}, \text{cm}^{-1}$ ($\lambda_{\text{abs}}, [\text{nm}]$)	fwhm [cm^{-1}]	Relative Intensity ($\times 10^{-14}$)
$(d\pi)^6 \rightarrow {}^1[(d\pi)^5(\pi_2^*)]$	41,050 (244) ^a	ϵ	ϵ
$(d\pi)^6 \rightarrow {}^1[(d\pi)^5(\pi_1^*)]$	39,250 (255) ^a	ϵ	ϵ
$\pi \rightarrow \pi^*$ (bpy)	34,520 (290)	2940	2.76
$[\pi \rightarrow \pi^*] + [(d\pi)^6 \rightarrow (d\pi)^5\pi^*]$ ^a	30,360 (330)	4020	1.96
$[\pi \rightarrow \pi^*] + [(d\pi)^6 \rightarrow (d\pi)^5\pi^*]$ ^a	27,430 (365)	3670	2.50
$(d\pi)^6 \rightarrow {}^1[(d\pi)^5(\pi_1^*)]$ (bpy)	22,700 (441)	3330	2.14
$(d\pi)^6 \rightarrow {}^1[(d\pi)^5(\pi_1^*)]$ (D0)	20,860 (479)	2330	2.97

^a Tentatively assigned as overlapping ligand-based and metal centre-based transitions.

^b Determined from 1st and 2nd derivative plots. ϵ Fixed to improve fitting procedure.

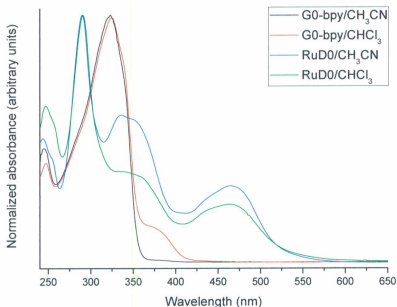


Figure 2.39 Normalized absorbance of G0-bpy and RuD0 in CHCl₃ and CH₃CN ((298 ± 3) K, 1 atm N₂).

CH₃CN, with the exception of the 30,360/27,430 cm⁻¹ absorbance, which is found in both G*n*-bpy and RuD*n* absorbance spectra. This supports the assignment of the absorbances at 243 and 255 nm as MLCT-based transitions, while the 290 nm absorbance is likely associated with the bpy ligands, as the dendrimer chains absorb at lower energies in both G*n*-bpy and RuD*n* (*n* = 1 – 3).

Normalized absorption spectra of RuD0 and G0-bpy in CH₃CN and CH₂Cl₂ are shown in Figure 2.39. The relative absorbance intensities of the ¹MLCT bands at 335 and 466 nm show an apparent solvent dependence, increasing in relative intensity in

CH₃CN relative to CHCl₃. The enhancement of the band at 344 nm relative to that at 464 nm is greater in CH₃CN than in CH₂Cl₂. It is difficult to ascertain the microscopic origin of these intensity differences from normalized spectra, but some general statements can be made. It is likely that the observed changes are due to a combination of (a) a small amount of solvatochromism of the $(d\pi)^6 \rightarrow {}^1[(d\pi)^5(\pi^*)]$ bands, and (b) changes in extinction coefficient due to the effect of changing solvent dielectric constants on excited state dipole moments, as per equations [2.14-2.15]^{48,85,86}:

$$\lambda_o = \frac{(\Delta\bar{\mu})^2}{a^3} \left[\frac{D_s - 1}{2D_s + 1} - \frac{D_{op} - 1}{2D_{op} + 1} \right] \quad [2.14]$$

$$f_{osc} = \int e(\bar{\nu}) d\bar{\nu} = \frac{4\pi N_A \nu}{3000 c n \hbar \ln 10} |\bar{M}|^2 \quad [2.15]$$

where D_s and D_{op} are the static and optical dielectric constants, respectively; a is the radius of a spherical cavity enclosing the molecule; [2.15] is the oscillator strength of an absorption band as a function of the integrated absorptivity, $\int e(\bar{\nu}) d\bar{\nu}$; c is the speed of light, n is the refractive index of the solvent; and \bar{M} is the transition moment. The large static dielectric constant of CH₃CN ($D_s = 36.3$) reflects the ability of this solvent to tolerate larger dipole moments and charge densities relative to CH₂Cl₂ ($D_s = 8.9$).⁸⁷ Thus, there is a drive towards planarization and delocalization of charge in CH₂Cl₂, while CH₃CN can accommodate a broad distribution of conformations and, thus, ³MLCT states. Starting in Section 2.5.3, these effects are described in greater detail.

The RuD_n complexes show a reduction in the quantity of isomerization relative to the free ligands, and the smallest RuD0 species is stable to repeated and prolonged excitations in CH_3CN ; however, in CHCl_3 or with increasing dendrimer size decreased spectral stability is seen. Interestingly, despite the potential availability of the HT mechanism there is nonetheless a dramatic rigid medium stabilization effect that causes attenuation of photoinduced spectral changes, both reversible and irreversible, of the RuD_n dendrimers in PMMA films. This behaviour was previously observed where an increased activation barrier to isomerization was reported in "frictional" or viscous environments relative to non-frictional environments.^{84,88,89} It has also been reported that isomerization of stilbenes in fluid solution is also dependent on the polarity of the solvent, as polar solvents reduce both the lifetime of the stilbene excited state and the quantity of side product formation by stabilizing the $^1p^*$ state;^{88,90} this accounts for the stability of RuD0 and RuD1 in CH_3CN relative to CHCl_3 . Not only does this stabilization effect enhance the rate of relaxation of the twisted intermediate state - partitioning itself into a ~1:1 distribution of *cis* and *trans* ground state geometries - but it also increases the height of the thermal barrier to $^1c^*$ state population and, thus, decreases the rate of dihydrophenanthrene (DHP) formation by the $^1c^* \rightarrow ^3\text{DHP}^*$ pathway (as previously seen in Section 1.5.6 and Figure 2.37).

2.5.3 Excited State Photophysics of the RuDn Dendrimers.

2.5.3.1 Emission Spectra.

As with their absorbance spectra, the luminescence spectra of RuDn are insensitive to increasing dendrimer generation. Interestingly, the RuDn dendrimers do demonstrate a great deal of variability in their degree of photostability as a function of solvent; for example, whereas there are some spectral changes upon irradiation of RuD0 in CHCl₃, very little change is detected when the solvent medium is CH₃CN. As mentioned in the discussion of the Gn-bpy dendrimers, studies on the fate of the excited state of stilbene have revealed an attenuation of both excited state lifetimes and of rate of DHP side product formation with increasing solvent polarity, which has been ascribed to improved stabilization of the charge-localized ¹p* twisted intermediate state in polar solvents.^{88,90} This may suggest that there is a distance-dependent energy transfer from the poly(phenylenevinylene) chromophores to the core for dendrimers of an intermediate size, which is supported by literature reports that dendron-to-core energy transfer proceeds *via* a Förster E_NT mechanism.⁸¹

While it is unclear if this ¹p* stabilization effect is also present in dendrimers constructed from a series of stilbenoid units, the aforementioned cross-conjugation of the poly(phenylenevinylene) structure may cause these dendrimer chains to behave less like a polymer and more like a collection of monomers, and the minimal spectroscopic changes observed with larger dendrimer generations relative to smaller generations suggest that this inference may have some validity. Also, the absorption spectral changes are consistent

with those observed in the photoinduced *trans-cis* reactions of other stilbene-based compounds.⁹¹ On the other hand, the absorption spectra of free and complexed dendritic ligands are rather different, indicating that there is significant electronic communication between the metal centre and the ligand states in all generations. For example, excitation into the higher energy absorbance bands of **RuD0** causes IL \rightarrow MLCT sensitization and intense emission, and so it is likely that this pathway plays a significant role in the observed reduction in the yield of isomerization and cyclization products for the **RuD n** species relative to the free ligands in solution.

Despite this communication between the ligands and the metal centre, excitation of the ligand-based absorption bands nonetheless gives rise to ligand fluorescence as well as ³MLCT luminescence. That these two relaxation pathways are both available may indicate that the dendrimer side chains are only weakly coupled, due to cross-conjugation.

2.5.3.2 Emission Spectral Fitting.

Emission spectral fitting of the steady-state luminescence of **RuD n** in CH₃CN uncovered a very weak secondary emission band that is thought to originate from a secondary emissive bpy-based ³MLCT state, based on the similarity of the shape and emission wavelength of maximum intensity of this band with that of [Ru(bpy)₃]²⁺. Subtraction of this [Ru(bpy)₃]²⁺-like band from the original emission spectrum, followed by emission spectral fitting of the resulting ³MLCT luminescence, revealed surprisingly small values of S_M and $\Delta\bar{\nu}_{1/2}$ for **RuD n** in CH₃CN relative to [Ru(bpy)₃](PF₆)₂ in the

same solvent. As discussed in the **Experimental** section, the Huang-Rhys factor S_M is related to the degree of geometric distortion in the excited state relative to the ground state, and so a small value of S_M means that the degree of distortion of the excited state geometry of **RuDn** (relative to its ground state geometry) is less than that for the excited and ground states of $[\text{Ru}(\text{bpy})_3](\text{PF}_6)_2$. As $\Delta\bar{\nu}_{1/2}$ is a measurement of the width of the emission band at half-height, a small value of $\Delta\bar{\nu}_{1/2}$ describes an emission band that is more narrow (and, therefore, less strongly coupled with the solvent) than expected, relative to $[\text{Ru}(\text{bpy})_3]^{2+}$. While placing $[\text{Ru}(\text{bpy})_3]^{2+}$ in a rigid PMMA matrix yields no change in S_M (1.14, from 1.1 in CH_3CN) but causes a dramatic lowering of $\Delta\bar{\nu}_{1/2}$ from 1750 cm^{-1} to 1498 cm^{-1} , it is interesting to note that the values of $\Delta\bar{\nu}_{1/2}$ for **RuDn** (and especially **RuD0**) in fluid media are comparable with or even smaller than that for $[\text{Ru}(\text{bpy})_3]^{2+}$ in a rigid PMMA matrix, clearly indicating that the $^3\text{MLCT}$ excited state of these compounds does not interact strongly with the surrounding solvent medium.

The observed reduction of both S_M and $\Delta\bar{\nu}_{1/2}$ could be caused by a delocalized $^3\text{MLCT}$ state, which would distribute the excited state charge density and the geometric distortions produced by excited state formation over a larger framework than would a localized excited state, reducing both inner- and outer-sphere reorganization energies in the **RuDn** complexes. The invariance of **RuDn** $^3\text{MLCT}$ absorbance and luminescence with increasing dendrimer generation does not appear to agree with this analysis, as we might expect delocalization over larger and larger frameworks to yield changes in both the

energy and shape of these spectra. On the other hand, $S_M = 0.47$ for both **RuD1** and **RuD2** while $\Delta\bar{\nu}_{1/2}$ falls from 1600 to 1500 cm^{-1} on moving from **RuD1** to **RuD2**. These data, combined with the invariant $^3\text{MLCT}$ absorbance and luminescence peaks, describe an excited state that is indeed delocalized, but over a relatively short distance. In light of the spectral data it seems reasonable to assume that the delocalization occurs over the entirety of the dendritic arms of **RuD0**, but once we move to **RuD1** the extension of this delocalization is inhibited by cross-conjugation. For this reason, **RuD1** and **RuD2** exhibit similar values of S_M as their excited states are distributed over a very similar framework. For **RuD0**, the slightly higher S_M (0.52) and E_0 (15,060 cm^{-1} , vs. ~14,947 and 15,993 cm^{-1} for **RuD1** and **RuD2**) are ostensibly due to a slightly shorter delocalization length, while the lower value of $\Delta\bar{\nu}_{1/2}$ (1498 cm^{-1}) is due to the diminished interaction of the delocalized excited state (which encompasses the whole dendritic structure of the ligand) with the solvent. Thus, the principal effect of increasing dendrimer generation in **RuD n** is not increased delocalization length, but rather decreased coupling between the solvent and the excited state due to the increased steric bulk of the larger dendrimer. There appears to be a trade-off between the electronic isolation due to delocalization seen in **RuD0** and the occlusion of solvent due to increasing steric bulk around the metal complex seen in **RuD2**, resulting in a higher value of $\Delta\bar{\nu}_{1/2}$ for the intermediate case of **RuD1**.

2.5.3.3 Time-Resolved Luminescence Decay.

Luminescence decay measurements of the RuD_n dendrimers in CH_3CN at room temperature yielded biphasic kinetics, where monoexponential decay with $\tau_2 = 270 - 280$ ns was preceded by a brief risetime which had a lifetime of ~ 11 ns in RuD0 and ~ 20 ns in RuD1 and RuD2 . Though it is impossible at this point in the Discussion to determine what is causing this risetime, this result may suggest that the interpretation of the anomalous residual signal in the emission spectral fitting data as being a weak emission band may be correct. These biphasic kinetics persist in the luminescence decay of RuD0 at 77 K in a 4:1 EtOH/MeOH glass, where enhancement of both decay lifetimes was seen relative to those measured at room temperature, but excitation of RuD_n encapsulated in rigid PMMA matrices yielded rather different excited state dynamics.

The decay traces for RuD_n ($n = 0 - 3$) were all successfully fit to biexponential decay functions to yield the data in Table 2.6, where an initial decay of $\tau_1 = 220 - 310$ ns is followed by a long-lived monoexponential decay of $\tau_2 = 1.7 - 2.5$ μs . By once again considering RuD0 as a being in a class of its own, the lifetime of the long-lived exponential process decreases from 2.5 to 2.3 to 1.7 μs from $\text{RuD1} - \text{RuD3}$, while $\tau_2 = 2.3$ μs for RuD0 , the same as RuD2 . Interestingly, the solution phase data seem to exhibit a similar trend, showing that the lifetimes of RuD0 and RuD2 are within experimental error of each other, while the lifetime of RuD1 is slightly greater. However, evidence for a discernable trend in the first exponential is quite a bit more scant.

The decay traces were also fit to a WWK stretched exponential distribution function in order to assess the degree of nonexponentiality of the data arising from the heterogeneity of the rigid PMMA matrix. In this analysis it was found that β ranges from 0.44 to 0.37 to 0.30 for RuD1-RuD3 and 0.31 for RuD0, indicating that the RuD n chromophores are contained within a highly heterogeneous solvent environment as a consequence of the plastic film casting process; the nonexponential behaviour of MLCT states in rigid media is a well-known phenomenon.⁴⁸

2.5.3.4 Laser Flash Photolysis and Global Analysis.

The transient absorption data of RuD0 in CH₃CN were prepared for processing using the global kinetic analysis routine that was outlined in the Experimental section, by fitting the individual decay traces to appropriate exponential functions by non-linear curve fitting routines. The resultant functions were compiled into a transient absorption spectrum to reduce contributions to the global fitting results from shot noise, which result from random source/detector variability (Figures 2.32 – 2.35). In order to minimize contributions to the risetime component from the instrument response due to the 5.4 ns laser pulse width, all transient absorption decay data up to $t = 8.55$ ns (the point in time at which the contribution to the decay traces was judged to be negligible relative to the intensity of the transient absorption signal) was excluded from the curve fitting analyses.

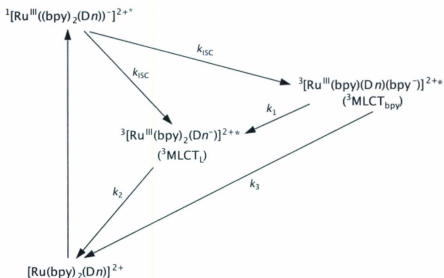


Figure 2.40 Proposed 3-step kinetic model (the “dual emission model”) for global analysis of laser flash photolysis data acquired for RuD0 in CH₃CN.

Initially the data was fit to a kinetic model of dual emissive ³MLCT states, where one weakly emissive, higher-lying ³MLCT_{bpy} state was dynamically coupled with a second lower-lying ³MLCT_L state (Figure 2.40),



This hypothesis was predicated upon the discovery of a weak secondary emission in the spectral fitting analysis and on the observation of prompt luminescence and transient

absorption risetimes. In the proposed model, population of the $^1\text{MLCT}$ state is followed by rapid population of both bpy-localized ($^3\text{MLCT}_{\text{bpy}}$) and dendrimer-localized ($^3\text{MLCT}_{\text{L}}$) states. A central assumption of this 3-step model is that the unusually small values of S_M and $\Delta\bar{\nu}_{1/2}$ inhibit the normally rapid interligand charge transfer (ILCT) process, slowing this kinetic process (k_1 in Figure 2.40) sufficiently to permit its observation on a nanosecond timescale. Initial values of $k_1 = 1/(10 \text{ ns})$ and $k_2 = 1/(150 \text{ ns})$ were approximated from fits of individual transient absorption decay traces, while a value of $k_3 = (900 \text{ ns})^{-1}$ was chosen based on the observation of a $[\text{Ru}(\text{bpy})_3]^{2+}$ -like signal in the $^3\text{MLCT}$ luminescence spectrum. Unfortunately this model appeared to be unsatisfactory, as the fitting routine failed to converge and no value for k_3 could be determined.

Analysis of the data was successful upon removal of the third step from the global analysis fitting procedure; thus, the transient absorption spectrum was fit to a two-step reaction model (Figure 2.41).



where $^3\text{MLCT}_1$, $^3\text{MLCT}_2$, and GS represent the short-lived, weakly emissive intermediate, the thermally-equilibrated excited state, and the ground state, respectively.

Rather than invoke a weakly emitting bpy-based $^3\text{MLCT}$ state, this model attributes the early timescale kinetics to the conversion of a short-lived conformer of the dendrimer to the geometry required for formation of its thermally-equilibrated state. The driving force for this geometric reorganization is ascribed to planarization of the

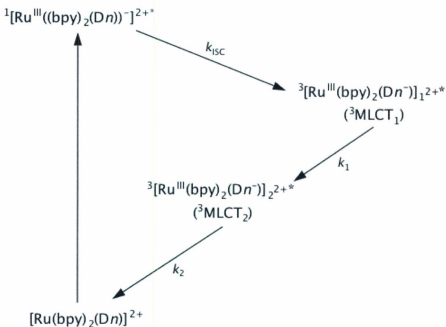


Figure 2.41 Proposed 2-step kinetic model (the “conformational dynamics model”) for global analysis of laser flash photolysis data acquired for RuD0 in CH₃CN.

poly(phenylenevinylene) chains that is required for subsequent delocalization of the ³MLCT spin density and, ultimately, stabilization of the thermally-equilibrated ³MLCT state. This fitting procedure yielded $k_1 = (9.2 \pm 0.3) \times 10^7 \text{ s}^{-1}$ ($\tau_1 = (10.6 \pm 0.4) \text{ ns}$) and $k_2 = (7.36 \pm 0.02) \times 10^8 \text{ s}^{-1}$ ($\tau_2 = (135.8 \pm 0.4) \text{ ns}$) (see Figure 2.42), values that are in good agreement with those measured by analysis of individual transient absorption decay measurements, as previously discussed. Also, the value of k_1 is also in good agreement with that determined from luminescence decay curve fitting.

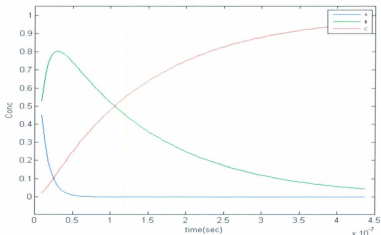


Figure 2.42 Concentration profiles of ${}^3\text{MLCT}_{\text{bpy}}$ (A, blue), ${}^3\text{MLCT}_{\text{L}}$ (B, green), and ground states of RuD0 in CH_3CN as determined from global analysis of laser flash photolysis data.

A similar approach was taken with the transient absorption spectrum of RuD0 in PMMA but the kinetics have yet to be modeled successfully. Nonetheless, this data is interesting and may prove useful in understanding the unusual behaviour of these dendritic metal complexes. Of particular interest is the observation of wavelength-dependent kinetics in the ${}^3\text{MLCT}$ bleach on early timescales that gradually become wavelength-independent, as a result of the formation of isosbestic points at 440 and 500 nm. There is clearly a dynamic process taking place that involves the ${}^3\text{MLCT}$ state of RuD0 that results in a narrowing of the negative absorption band at longer timescales, suggesting that either (a) an initial short-lived ${}^3\text{MLCT}$ intermediate state undergoes an interligand transfer to yield the thermally-equilibrated excited state, or (b) the observed spectral changes are due to an intramolecular reorganization of the dendritic ligand.

2.5.4 Elucidation of the Origin of Dual Emission and Growth Kinetics in Luminescence and Transient Absorption of the RuD n Dendrimers.

2.5.4.1 Luminescence of Impurities or Ligand-Based States.

As introduced in Section 2.4.3, spectral fitting of steady-state luminescence of the RuD n dendrimers in CH₃CN uncovered a small secondary emission band that was thought to originate from an emissive bpy-based ³MLCT state, a ligand-based IL state or an emissive impurity. Spectral artifacts originating from a impurity can be difficult to definitively isolate and identify; however, while MALDI-TOF and NMR data indicate that there were no foreign species present,⁹² the strongest indication that these photophysics are intrinsic to the molecule comes from the observation of similar growth kinetics and monoexponential decay from excitation into different absorbance bands (MLCT excitation at 446 nm in luminescence decay and a mix of metal- and ligand-based excitation at 355 nm in transient absorption decay measurements). The intensity of the fluorescence and transient absorption growth kinetics relative to the primary monoexponential decay are quite significant (e.g. ~20% of the fluorescence decay intensity of RuD2 in CH₃CN) and too great to be attributed to an otherwise high-on-undetectable trace impurity. Also, the intensity of the secondary emission and of the risetimes is similar in RuD0, RuD1 and RuD2 despite the vastly different molecular weights of these compounds; given that these signals scale with increasing dendrimer size it is highly unlikely that they are due to contaminants.

Transient absorption decay traces and spectra were acquired from the excitation of an absorption band that is likely to contain both dendrimer and metal centre character (at 355 nm), whereas luminescence decay traces of the $^3\text{MLCT}$ state of RuD_n complexes accrue from excitation of the $[(d\pi)^6 \rightarrow {}^1(d\pi)^5(\pi)^*]$ band using 446 nm light. As previously stated, risetimes of approximately $\tau \sim 10$ ns were observed in both transient absorption and fluorescence measurements, followed by monoexponential transient absorption decay lifetimes of $\tau \sim 110 - 150$ ns and fluorescence decay of $\tau = 280$ ns. These data indicate that population of either ligand- or metal-based states ultimately results in a brief risetime followed by luminescence from the $^3\text{MLCT}$ state, suggesting that formation of the ligand-based ^1IL state by laser flash photolysis quickly leads to sensitization of the $^3\text{MLCT}$ state, possibly *via* either the $^1\text{IL} \rightarrow {}^3\text{IL} \rightarrow {}^3\text{MLCT}$ or $^1\text{IL} \rightarrow {}^1\text{MLCT} \rightarrow {}^3\text{MLCT}$ pathways. Steady-state luminescence of RuD0 demonstrates that excitation of ligand-based states yields both $^3\text{MLCT}$ and (a small amount of) ligand-based emission.

The question of whether ligand-based states are responsible for these atypical kinetics was briefly thought to have been addressed by Arai *et al.* who reported³⁹³ that the rate of photoisomerization in certain stilbene-containing dendrimers was dependent on the singlet excited state lifetime, which was found to be $\tau = 10$ ns (i.e. the same as the lifetime for the risetime kinetics of RuD_n). However, this ~ 10 ns lifetime was only observed in dendrimers with molecular weights above $M = 6000 \text{ g mol}^{-1}$ and the luminescence decay risetime observed in this work is very similar for both RuD0 ($\tau = (11 \pm 2)$ ns, $M = 1288.24 \text{ g mol}^{-1}$) and RuD2 ($\tau = (19 \pm 2)$ ns, $M = 2930.78 \text{ g mol}^{-1}$); therefore, these data

seem to suggest that Arai's result is not pertinent to these compounds. Furthermore, if the observed risetime in the laser flash photolysis experiments is indeed due to sensitization of the $^3\text{MLCT}$ state originating from a ligand-based ^1IL state, then there should be no observable risetime in the fluorescence decay experiments where excitation is into a metal-centred absorption band and the ligand states are avoided altogether, as is the case in the fluorescence decay measurements of $\text{RuD}n$.

This analysis does not discount the participation of ligand-based states in the excited state behaviour of the $\text{RuD}n$ dendrimers as a whole, but it does suggest that the short-lived risetime is indeed due to metal-centred dynamics. Attempts to rationalize the observed photophysics led to the development of two separate models: (a) the conformational gating model (i.e. the 2-step kinetic model introduced in Section 2.5.3.4) and (b) the attenuated interligand charge transfer model (the 3-step model).

2.5.4.2 The Role of Conformational Gating in the Dynamics and Spectroscopy of a Non-Thermally-Equilibrated $^3\text{MLCT}$ State.

Global analysis of laser flash photolysis data of RuD0 in CH_3CN favoured a kinetic model involving transfer from a non-emissive $^3\text{MLCT}_1$ state to the thermally-equilibrated $^3\text{MLCT}_2$ state, as opposed to the dual emitting $^3\text{MLCT}$ states model that is discussed in Section 2.5.4.3. In either case, it is apparent that there are two distinct excited state processes involved, where population of the thermally-equilibrated $^3\text{MLCT}$ state first occurs through a separate MLCT state. While the latter model favours a transfer between discrete $^3\text{MLCT}$ states from different ligands in the metal complex, the conformational

gating model invokes a more fluid and dynamic picture of the nature of the $^3\text{MLCT}$ state of these complexes, one where the dendrimer side chains play a non-innocent role in the mechanism of formation of these states.

The growth kinetics can theoretically be explained by dynamic intraligand reorganization of the $^3\text{MLCT}$ state on a nanosecond timescale. Formation of a $^1\text{MLCT}$ state and subsequent ISC of RuD_n in CH_3CN occurs on an ultrafast timescale, initially leading to a vibrationally and energetically hot $^3\text{MLCT}_1$ excited state that is localized on the bipyridine molecule^{94,95} of the derivatized ligand. The dendrimer side chains are randomly oriented as they share no $^3\text{MLCT}$ spin density on this early timescale. With time, this $^3\text{MLCT}_1$ state begins to stabilize by delocalization of the excited state spin density onto these side chains, a process that is aided by the fact that the first stilbenoid moiety is indeed fully conjugated with the bipyridine molecule, as the aforementioned cross-conjugation of subsequent poly(phenylenevinylene) groups occurs only at branching points further along the polymer chains (Figure 2.43). As previously discussed, it is also likely that this limited conjugation length is the cause of the invariance of RuD_n $^3\text{MLCT}$ absorbance and luminescence to increasing dendrimer size. In this manner, delocalization stabilizes the $^3\text{MLCT}_1$ state by reducing the magnitude of structural perturbations in the molecule, enforcing planarity and rigidity in the dendritic side chains and thereby decreasing S_M and $\Delta\bar{\nu}_{1/2}$ in the nascent $^3\text{MLCT}_2$ state. Thus, the $^3\text{MLCT}_1$ and $^3\text{MLCT}_2$ excited states represent not discrete, wholly-independent species, but rather two ends of a continuum. This conformational change is a relatively slow process, as the observation of

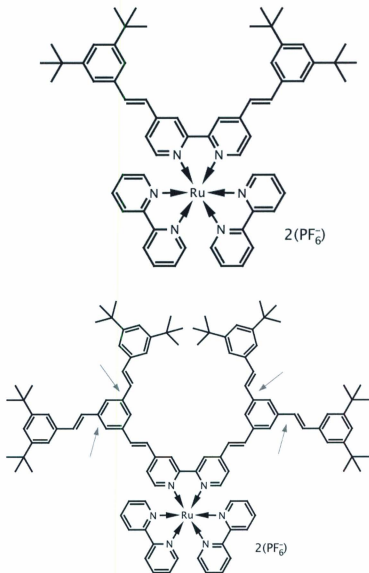


Figure 2.43 Illustration of the lack of cross-conjugation in RuD0 (top) relative to RuD1 (bottom), where cross-linked sites are denoted by arrows.

a risetime in the emission and transient absorption decay traces demonstrates that the $^3\text{MLCT}_1$ and $^3\text{MLCT}_2$ states are not in equilibrium with one another.

A comparison of transient absorption spectra of **RuD0** in both CH_3CN and PMMA may lend further support to this model of dynamic conformational change, specifically with regard to differences in the position and nature of the isosbestic points straddling the negative transient absorbance band centred at ~ 470 nm. The evolution in time of the TA spectra of **RuD0** in CH_3CN result in clearly defined isosbestic points at 440 and 495 nm, whereas the analogous points in PMMA are not as clearly defined at early times. The negative absorbance band found in the PMMA TA data is initially broader and more intense than that found in fluid solution and becomes progressively narrower, spanning from 430 – 510 nm at early times to 440 – 500 nm. This narrowing is a spectral manifestation of the observation of reduced values of S_M and $\Delta\bar{\nu}_{1/2}$ in particular, given that the latter parameter dictates bandwidth. The current model would explain this observation as being due to the rigid matrix causing attenuation of the dynamic side chain motion that permits excited state delocalization, slowing the conversion of the $[\text{Ru}(\text{bpy})_3]^{2+}$ -like $^3\text{MLCT}_1$ state to the rigid and constrained delocalized $^3\text{MLCT}_2$ state.

2.5.4.3 Attenuation of ILCT Between Dual Emissive $^3\text{MLCT}$ States.

A second reaction model was proposed in Section 2.5.3.4 wherein the unique physical and electronic properties of **RuDn** in CH_3CN result in the establishment of a barrier to interligand charge transfer from the two 2,2'-bipyridine groups to the dendritic ligand,

attenuating the rate of ${}^3\text{MLCT}_{\text{bpy}}$ -to- ${}^3\text{MLCT}_{\text{L}}$ transfer sufficiently for radiative decay from the ${}^3\text{MLCT}_{\text{bpy}}$ to become a competitive process on a nanosecond timescale. This hypothesis was initially predicated upon the results of room temperature emission spectral fitting, as it was observed that the weak luminescence seen in the residual data was strongly suggestive of a $[\text{Ru}(\text{bpy})_3]^{2+}$ -like ${}^3\text{MLCT}$ state, both in energy and in shape.

Excitation into the $[(d\pi)^6 \rightarrow {}^1[(d\pi)^5(\pi^*)^1]]$ absorption band of RuDn quickly populates the dendritic thermally-equilibrated ${}^3\text{MLCT}$ state, but there are also two bpy ligands present that will readily form a ${}^3\text{MLCT}$ excited state under these conditions. Typically, heteroleptic complexes such as these exhibit luminescence from only one excited state in accordance with Kasha's rule,⁹⁶ which states that all non-equilibrated excited states of a chromophore naturally cascade down to the lowest-lying state, and it is this state from which all observed photophysics will accrue. However, the observation of a second weak emission at higher energy coupled with the growth kinetics led to the assumption that the usual unsubstituted bpy-to-dendritic bpy interligand transfer was being attenuated by some unknown factor, allowing the observation of the typically ultrafast interligand transfer on a nanosecond timescale and providing the opportunity for a small portion of the ${}^3\text{MLCT}_{\text{bpy}}$ population to relax by other pathways (e.g. luminescence).

Examination of the potential energy (PE) surfaces and emission spectral fitting results lends some insight into a possible origin for the attenuation of this IL transfer. Not only do the small S_M values determined from emission spectral fitting of RuDn in CH_3CN inform that the ${}^3\text{MLCT}_{\text{L}}$ state in these compounds is rather nested relative to its ground

state, it also reports a value for $\Delta\bar{\nu}_{1/2}$ that indicates that the ${}^3\text{MLCT}_L$ PE surface is more narrow than that of $[\text{Ru}(\text{bpy})_3]^{2+}$ in CH_3CN and similar or nearly identical to that of $[\text{Ru}(\text{bpy})_3]^{2+}$ in a PMMA film. The reduced magnitude of $\Delta\bar{\nu}_{1/2}$ suggests that the excited state of **RuDN** does not associate as strongly with its environment and thus has a narrower PE surface than $[\text{Ru}(\text{bpy})_3]^{2+}$ in CH_3CN or, for that matter, than a ${}^3\text{MLCT}_{\text{bpy}}$ state that is very similar to the ${}^3\text{MLCT}$ state of $[\text{Ru}(\text{bpy})_3]^{2+}$. While the ${}^3\text{MLCT}_L$ state has relatively small values for S_M and $\Delta\bar{\nu}_{1/2}$ and lies above the ground state PE surface in a semi-nested manner, the ${}^3\text{MLCT}_{\text{bpy}}$ state is broader and lies at a higher energy. Thus, as illustrated in Figure 2.44, while E_0 for the ${}^3\text{MLCT}_{\text{bpy}}$ state is sufficiently large to enable facile bpy-to-dendrimer interligand transfer, the unusually small values of S_M and $\Delta\bar{\nu}_{1/2}$ for the ${}^3\text{MLCT}_L$ state result in the establishment of an activation barrier to the putative room temperature ${}^3\text{MLCT}_{\text{bpy}}\text{-to-}{}^3\text{MLCT}_L$ PE surface crossing proposed by this model. This additional energetic demand attenuates the observed rate for interligand crossing sufficiently to allow a small portion of the ${}^3\text{MLCT}_{\text{bpy}}$ population to relax by radiative decay, resulting in (a) the observation of nanosecond risetime kinetics and (b) the appearance of weak luminescence from the ${}^3\text{MLCT}_{\text{bpy}}$ state.

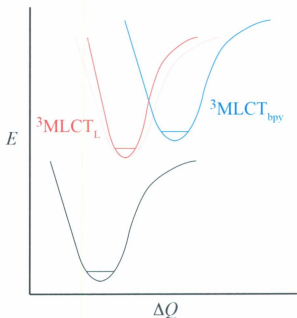


Figure 2.44 Illustration of the effect of small S_M and $\Delta\bar{\nu}_{1/2}$ values on ${}^3\text{MLCT}$ potential energy surfaces. Note the higher energy of the point of intersection between ${}^3\text{MLCT}_{\text{bpy}}$ and ${}^3\text{MLCT}_L$ (red) versus a more typical ${}^3\text{MLCT}$ PE surface (pale red), inhibiting ILCT without changing the driving force for this reaction.

2.5.4.4 Comparison of Models.

The mechanism of intramolecular reorganization was introduced in response to the failure of the dual emissive state model during the global analysis fitting procedure. The very unusual nanosecond emission and transient absorption risetimes suggested that some rather surprising excited state dynamics were occurring in these molecules, as the kinetics that lead to formation of thermally-equilibrated ${}^3\text{MLCT}$ states in Ru^{II} polypyridyl

complexes typically occur on ultrafast timescales that far surpass the resolution of the equipment used in the experiments described in this Dissertation. The results from global analysis support the mechanism presented by the conformational dynamics model, whereby ISC from the $^1\text{MLCT}$ state populates a $^3\text{MLCT}_1$ state on a non-planar dendritic ligand, followed by stabilization of the ligand through planarization and subsequent delocalization to yield the thermally-equilibrated $^3\text{MLCT}_2$ state. However, while emission spectral fitting demonstrated the presence of a weak emission with very similar characteristics to those of $[\text{Ru}(\text{bpy})_3]^{2+}$, this sequential two-step global analysis model precludes the existence of a second emissive state.

While this was initially of concern, one must consider that spectral fitting determined that the underlying structure of this secondary emission band is very similar to the structure of bpy-based $^3\text{MLCT}$ emission of $[\text{Ru}(\text{bpy})_3]^{2+}$, and $^3\text{MLCT}$ luminescence from a 5,5'-derivatized 2,2'-bipyridine should not have the same spectral characteristics as the luminescence of $[\text{Ru}(\text{bpy})_3]^{2+}$, no matter how ordered or disordered its side chains are. For example, λ_{max} for $[\text{Ru}(\text{bpy})_3](\text{PF}_6)_2$, $[\text{Ru}(\text{dmb})_3](\text{PF}_6)_2$ and $[\text{Ru}(\text{dmb})_2(\text{vbpy})](\text{PF}_6)_2$ (Figure 2.45) in CH_3CN are 622, 642 and 670 nm,^{48,77} demonstrating that even simple methylation of the 5 and 5' positions causes a significant red-shift of λ_{max} for Ru^{II} polypyridyl complexes. It is highly unlikely that the 5,5'-derivatized dendritic ligands employed in this work could be responsible for the secondary emission, which then suggests that the 2,2'-bpy ligands are the origin of this signal.

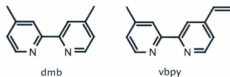


Figure 2.45. Structures of dmb and vbpy ligands from references 46 and 91.

Dual emission has been previously reported for Ru^{II} polypyridyl complexes at low temperatures,⁹⁷⁻¹⁰⁰ which reduces the rate of any interligand electron transfer process that would depopulate a competing, secondary emissive ³MLCT state, but there are precious few reports of dual emission occurring in mononuclear Ru^{II} complexes at room temperature.¹⁰¹⁻¹⁰³ On the other hand, the results presented in this document suggest that it may be difficult to determine whether this is truly an unusual event, or whether it occurs more frequently than expected but that researchers fail to recognize this.¹⁰⁴

The failure of global analysis to yield a model that accommodates the weak secondary fluorescence is somewhat less surprising when one considers that the intensity of the signal that was discovered by spectral fitting is only ~4% of that of the primary ³MLCT fluorescence, so it is quite likely that this signal is too weak to be detected by the rather less sensitive technique of laser flash photolysis (which yields the data processed by global analysis to yield the hypothetical 2- and 3-step mechanisms). Furthermore, the lifetime of fluorescence decay of RuD0 in CH₃CN at 600 nm ($\lambda_{exc} = 446$ nm) was found to be $\tau = (98 \pm 7)$ ns, indicating that this 2,2'-bipyridine-based ³MLCT state is strongly quenched;

this would make its detection by nanosecond laser flash photolysis rather less likely. While it is hardly an unprecedented phenomenon, simultaneous emission from competing $^3\text{MLCT}$ states is nonetheless not recognized as being particularly common in Ru^{II} polypyridyl complexes.

Fitting luminescence decay traces of RuD_n ($n = 0 - 2$) in PMMA to both biexponential decay and WWK distribution functions yielded fits of very high quality. In assessing the nonexponential kinetics of these systems, it can be reasoned that the large distribution of local free volumes in the rigid plastic matrix⁴⁸ should constrain the poly(phenylenevinylene) chains of the dendritic ligands in many different conformations, ostensibly permitting varying degrees of $^3\text{MLCT}$ delocalization and, consequently, widely varying rate constants for luminescence decay from this state. While population of the "twisted" $^3\text{MLCT}$ state is followed by planarization in fluid solution, this process is inhibited in PMMA to a sufficiently thorough degree that it can no longer be observed spectroscopically on a nanosecond timescale. Instead, it is likely that this process has been inhibited to such a degree that radiative decay becomes a more feasible relaxation pathway, resulting in a broad distribution of fluorescence decay rates as determined by the extremely small β values produced by the WWK analysis. In contrast to the behaviour in PMMA, luminescence decay at 77 K in a 4:1 (v/v) EtOH/MeOH glass (a much more constrained environment than a PMMA matrix, which doesn't so much surround the chromophores as much as it encapsulates them within its relatively large internal free volumes) seems to show a 20-fold lengthening of the lifetime of this risetime. However,

whereas PMMA is a rigid plastic, this EtOH/MeOH glass is a frozen solvent, and the energies associated with formation of the excited state and its resultant reorganizations are sufficient to cause microscopic melting. It is still possible to observe the fluorescence risetime in this environment because while the duration of the kinetic process that produces the risetime is increased, so too is the lifetime of the thermally-equilibrated excited state and, thus, the fluorescence decay. It is nonetheless unclear why the smallest generation dendrimer **RuD0** should have such a small value of β (suggesting a broader distribution of excited states) relative to the much larger **RuD1** and **RuD2**.

The development of the models was largely based on (a) global analysis results and (b) the observation of a weak secondary emission and a risetime in the fluorescence decay traces. In light of the above arguments, it is apparent that the assumption that both emission signals in (b) were directly due to the same kinetic process was erroneous, and the debate of whether the 2-step or 3-step mechanism is more appropriate is somewhat irrelevant. Instead, a picture is emerging of a system that exhibits both dual emission and conformational dynamics.

2.5.5 Re-Evaluation of the Model of Excited State Dynamics of RuDn.

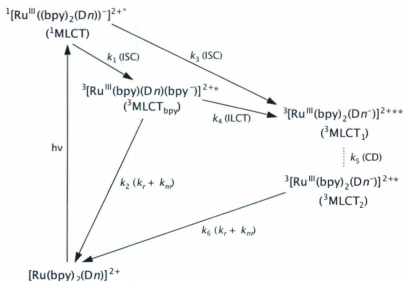


Figure 2.46 Summary of excited state dynamics of the RuDn dendrimers, demonstrating the interplay of conformational dynamics and ILCT. See text for details.

The complex picture of the excited state kinetics of RuDn dendrimers presented in Figure 2.46 is more readily understood by monitoring the evolution through time of (a) emission and ILCT from a bpy-based ($^3\text{MLCT}_{\text{bpy}}$) state, and (b) the impact of conformational dynamics in dendrimer-based ($^3\text{MLCT}_1$ / $^3\text{MLCT}_2$) states on ILCT. The kinetics of formation and relaxation of the bpy-based $^3\text{MLCT}_{\text{bpy}}$ are shown in equation [2.19]. Excitation of ground state RuDn yields a $^1\text{MLCT}$ excited state, followed by ISC to yield $^3\text{MLCT}_{\text{bpy}}$ (k_1) and $^3\text{MLCT}_1$ (k_3) states. Due to the presence of an activation

$$\frac{d[{}^3\text{MLCT}_{\text{bpy}}]}{dt} = k_1[{}^1\text{MLCT}] - (k_2 + k_4)[{}^3\text{MLCT}_{\text{bpy}}] \quad [2.19]$$

$$\frac{d[{}^3\text{MLCT}_1]}{dt} = k_3[{}^1\text{MLCT}] + k_4[{}^3\text{MLCT}_{\text{bpy}}] - k_5[{}^3\text{MLCT}_1] \quad [2.20]$$

$$\frac{d[{}^3\text{MLCT}_2]}{dt} = k_5[{}^3\text{MLCT}_1] - k_6[{}^3\text{MLCT}_2] \quad [2.21]$$

barrier to bpy-to-dendron ILCT (k_4) (Figure 2.44), a small amount of the ${}^3\text{MLCT}_{\text{bpy}}$ state persists long enough to decay directly to the ground state by k_2 (note that $k_2 = (k_r + k_w)$). This is the origin of the weak secondary signal detected by emission spectral fitting.

The kinetics of the vibrationally-hot dendritic ligand-based ${}^3\text{MLCT}_1$ state are summarized by equation [2.20]. ISC from the ${}^1\text{MLCT}$ state (k_3) initially yields ${}^3\text{MLCT}$ states that are localized upon the 2,2-bipyridine moiety of the dendritic ligand.^{94,95} With time, conformational dynamics within these dendritic ${}^3\text{MLCT}$ states (k_5) start to enforce planarization of the dendron backbone, improving intramolecular electronic overlap between the bpy donor and dendritic acceptor and enhancing the extent of delocalization until the energy-minimized, thermally-equilibrated ${}^3\text{MLCT}_2$ configuration is reached (equation [2.21]). Due to a combination of all these factors, the ${}^3\text{MLCT}_1$ and ${}^3\text{MLCT}_2$ (and all the configurations in between) states are not in equilibrium on the nanosecond timescale, thereby producing the risetime kinetics presented in this Dissertation.

2.5.6 The Origin of Ultrafast Excited State Dynamics of the RuD n Dendrimers.

This Discussion has thus far concerned itself with determination of the mechanism by which these dendrimers yield such unusual luminescence and transient absorption kinetics, so it is now necessary to attempt to explain why the excited state dynamics of these compounds are so atypical relative to other such heteroleptic Ru^{II} polypyridyl complexes.

An investigation into the rate constants for interligand electron transfer between excited states was carried out using equation [2.22], where k is the observed rate constant for the process in question; k_0 is the diffusion-limited rate constant ($k_0 = 10^{12} \text{ s}^{-1}$); ΔG° is the driving force for the electron transfer process (irrespective of the magnitude of the activation barrier for that process) and is defined as the difference between the $\nu' = 0 \rightarrow \nu = 0$ energy gaps of both the initial (E_0^I) and final (E_0^F) states as demonstrated in equation [2.23]; k_B is the Boltzmann constant (expressed in units of $\text{cm}^{-1} \text{ K}^{-1}$).

$$k = k_0 \exp \left[\frac{-(\Delta G^\circ + \bar{\lambda}_r)^2}{4\bar{\lambda}_r k_B T} \right] \quad [2.22]$$

$\bar{\lambda}_r$ is the total reorganization energy of the system, expressed in equation [2.24] as the sum of outer-sphere ($\bar{\lambda}_o$) and vibrational ($\bar{\lambda}_v$) reorganization energies averaged between the initial and final states, where $\bar{\lambda}_o$ and $\bar{\lambda}_v$ are defined in equations [2.25] and [2.26], respectively:^{48,85}

$$\Delta G^0 = E_0^i - E_0^f \quad [2.23]$$

$$\bar{\lambda}_T = \bar{\lambda}_V + \bar{\lambda}_{V0} \quad [2.24]$$

$$S_M = \frac{\bar{\lambda}_V}{\hbar\omega_M} \quad [2.25]$$

$$(\Delta\bar{v}_{1/2})^2 = (\Delta\bar{v}_{0,1/2})^2 + 16\lambda_V k_B T \ln 2 \quad [2.26]$$

Using the results of emission spectral fitting, a lower limit of $\tau \sim 670$ ps can be calculated for the lifetime for bpy \rightarrow L interligand transfer from equations [2.22] – [2.26], which differs by an order of magnitude from the lifetime of $\tau \sim 11$ ns determined for the risetime that was observed in the transient absorption and luminescence decay experiments. There are two major assumptions being made in this calculation, which are that (a) the spectral fitting parameters determined for the ${}^3\text{MLCT}$ state of $[\text{Ru}(\text{bpy})_3](\text{PF}_6)_2$ in CH_3CN are closely representative of those of the bpy-like state in RuDn in CH_3CN , and (b) the electronic and geometric configuration of the thermally-equilibrated ${}^3\text{MLCT}_2$ state accurately represent the active state of RuDn at the moment of interligand electron transfer. Given that the $[\text{Ru}(\text{bpy})_3]^{2+}$ -like contribution to the ${}^3\text{MLCT}$ luminescence spectra of RuDn was initially detected by spectral fitting routines, as well as the successful subtraction of a scaled $[\text{Ru}(\text{bpy})_3]^{2+}$ luminescence spectrum from that of RuD0 , it is likely that the spectral fitting parameters of the ${}^3\text{MLCT}_{\text{bpy}}$ state are sufficiently similar for the purposes of this calculation. On the other hand, it is unlikely that the second assumption is valid, as the spectral fitting parameters determined from the planar, delocalized conformation ostensibly adopted by the thermally-equilibrated ${}^3\text{MLCT}_2$ state do not accurately represent the nature of the acceptor in the ILCT process.

A review of the $[\text{Ru}(\text{bpy})_3]^{2+}$ literature with regards to the dynamics of formation of the $^3\text{MLCT}$ state reveals that there is a long-standing debate about the instantaneous dynamics of formation of this state. Specifically, a great deal of research has attempted to determine whether this state is delocalized over all three bpy ligands or localized upon a single bpy ligand following femtosecond ISC from the $^1\text{MLCT}$ state. The seemingly contradictory data may be reconciled by current efforts in our research group towards the introduction of a new model for ultrafast formation of $^3\text{MLCT}$ states in such d^6 polypyridyl complexes. Briefly, this model ascribes the ultrafast excited state dynamics to rapid electron hopping and coupled electron hole transfer between the three degenerate $^3\text{MLCT}$ states *via* low-frequency vibrational modes, producing a rotating dipole that - on the timescales before the onset of nuclear motion - is insensitive to the solvent environment. At longer timescales, the solvent begins to reorient itself in response to this transient polarization, in turn causing the rotational motion of the dipole moment to slow and allowing for increasing degrees of population of excited states on both derivatized and non-derivatized 2,2'-bpy ligands. In the work reported in this Chapter, it is this rotational mechanism that permits the onset of excited state dynamics from $^3\text{MLCT}_{\text{bpy}}$ and nonequilibrated $^3\text{MLCT}_1$ and $^3\text{MLCT}_2$ states, gradually populating the $^3\text{MLCT}$ states of all three ligands for longer and longer periods and ultimately culminating in the delocalization of the excited state spin density onto the poly(phenylenevinylene) arms to yield the final thermally-equilibrated $^3\text{MLCT}_2$ state. Thus, given that it is expected that the acceptor state will have different values for S_M , $\Delta\bar{\nu}_{1/2}$, and E_0 than those of the

thermally-equilibrated state, the discrepancy between observed and expected ILCT rates is unsurprising given the fact that these latter values were used in equations [2.21] – [2.25] to determine the 670 ps lifetime for ILCT. In summary, while the energetics of the $^3\text{MLCT}_{\text{bpy}}$ and $^3\text{MLCT}_2$ states favour a rapid ILCT event, conformational dynamics of the dendritic ligand impose an activation barrier to this process, ultimately slowing this process down to a nanosecond timescale.

The mechanism for disappearance of the prompt risetime in the luminescence decay traces of $\text{RuD}n$ ($n = 0 - 2$) in PMMA is interpreted as inhibition of conformational changes that allow planarization of the dendritic acceptor. Incorporation of the chromophores in a rigid PMMA matrix should "freeze" the dendron arms into a number of conformations, resulting in a broad distribution of fluorescence decay lifetimes (observed as extremely small β values) as well as by attenuating or preventing the $^3\text{MLCT}_1 \rightarrow ^3\text{MLCT}_2$ process from occurring. The origin of these differences may lie in the mechanics of dipole rotation in fluid or frozen media vs. a rigid plastic, as the slowing of this rotation is initiated by the interaction of the dipole moment of the excited state with surrounding solvent. The rotating dipole could be expected to have an even weaker solvent polarizing effect within the distribution of large free volumes of the rigid PMMA matrix. In this manner, the distribution of solvent microenvironments causes both attenuation of and broad variability in the rate constants for $^3\text{MLCT}_{\text{bpy}}$ emission, bpy-to-dendrimer ILCT, $^3\text{MLCT}_1 \rightarrow ^3\text{MLCT}_2$ conversion, and $^3\text{MLCT}_2$ emission.

2.6 Conclusions and Future Work.

Poly(phenylenevinylene) dendrimers are quite susceptible to both reversible and irreversible changes upon absorption of light, demonstrating that they may be of questionable utility in chromophoric applications. Incorporation of these structures into a ruthenium polypyridyl coordination complex leads to stabilization of these side chains by quenching their photoactivity through the formation of MLCT states, and some sensitization of the metal centre can be observed following excitation of ligand-based $\pi \rightarrow \pi^*$ states. However, the results acquired in this research suggest that this stabilization effect is imperfect, as it is limited to polar solvents of high dielectric constant and becomes less useful as the size of the dendritic ligand increases.

The determination of unusually small values of S_M and $\Delta\bar{\nu}_{1/2}$ along with the detection of a secondary weak emission signal from emission spectral fitting demonstrated that the RuD_n dendrimers exhibit emission from their thermally-equilibrated dendrimer-based $^3\text{MLCT}$ state, as well as a weak signal from a higher-lying bpy-based $^3\text{MLCT}$ state for which luminescence competes with interligand charge transfer to the lower-lying dendritic ligand. This model was developed from the observation of a rapid risetime preceding the decay of the thermally-equilibrated $^3\text{MLCT}_L$ state, as determined by time-resolved luminescence decay and laser flash photolysis measurements.

The considerable amount of thought and research effort directed towards determining whether the excited state dynamics are driven by either ILCT or conformational dynamics models appears to have yielded a mechanism of $^3\text{MLCT}$ formation and decay

that includes aspects of both models. Nonetheless, the primary origin for the unusual growth kinetics and dual emission in the **RuDn** dendrimers is the inhibition of interligand charge transfer between unsubstituted 2,2'-bipyridine ligands and the lowest-lying 5,5'-derivatized dendritic 2,2'-bipyridine ligand, arising as a consequence of the unusually constrained and isolated nature of the acceptor ligand as quantified by emission spectral fitting parameters such as S_M and $\Delta\bar{\nu}_{1/2}$.

Further examination of the photophysics of these dendritic complexes in a variety of fluid and rigid media is required for a proper assessment of the ligand stabilization effect. Similarly, the importance of sterics and electronic communication could be investigated in a study into the consequences of modification of the poly(phenylenevinylene) chains. Specifically, examining a series of dendrimers with increasing degrees of steric crowding around the phenyl rings (in a similar manner to that studied by Damrauer's group^{38,40,105}) will extend our understanding of the roles that planarization and ³MLCT delocalization play in the excited state properties of this class of dendritic coordination compounds. Effects of this nature may be used as part of molecular switches, wherein conformational dynamics and sterics can impart an "on/off" functionality to a molecule or could provide the opportunity for selection of a particular reaction pathway, with the mechanism of discrimination being provided by an appropriate wavelength of excitation, perhaps within a particular temperature range and in the presence or absence of additional reagents.

2.7 References.

- (1) Paris, J. P.; Brandt, W. W. *J. Am. Chem. Soc.* **1959**, *81*, 5001.
- (2) O'Regan, B.; Grätzel, M. *Nature* **1991**, *353*, 737.
- (3) Chang, Z.; Zhou, J.; Zhao, K.; Zhu, N.; He, P.; Fang, Y. *Electrochim. Acta* **2006**, *52*, 575.
- (4) Fancy, D.; Kodadek, T. *Proc. Natl. Acad. Sci. U.S.A.* **1999**, *96*, 6020.
- (5) Kim, J. S.; Rieter, W. J.; Taylor, K. M. L.; An, H.; Lin, W.; Lin, W. *J. Am. Chem. Soc.* **2007**, *129*, 8962.
- (6) Ma, D.-L.; Che, C.-M.; Siu, F.-M.; Yang, M.; Wong, K.-Y. *Inorg. Chem.* **2007**, *46*, 740.
- (7) Mishra, L.; Sinha, R.; Itokawa, H.; Bastow, K.; Tachibana, Y.; Nakanishi, Y.; Kilgore, N.; Lee, K. *Bioorg. Med. Chem.* **2001**, *9*, 1667.
- (8) Rieter, W. J.; Kim, J. S.; Taylor, K. M. L.; An, H.; Lin, W.; Tarrant, T.; Lin, W. *Angew. Chem. Int. Ed.* **2007**, *46*, 3680.
- (9) Draxler, S.; Lippitsch, M.; Klimant, I.; Kraus, H.; Wolfbeis, O. *J. Phys. Chem.* **1995**, *99*, 3162.
- (10) Concepcion, J. J.; Jurss, J. W.; Templeton, J. L.; Meyer, T. J. *Proc. Natl. Acad. Sci. USA* **2008**, *105*, 17632.
- (11) Concepcion, J. J.; Jurss, J. W.; Brennaman, M. K.; Hoertz, P. G.; Patrocinio, A. O. T.; Murakami Iha, N. Y.; Templeton, J. L.; Meyer, T. J. *Acc. Chem. Res.* **2009**, *42*, 1954.
- (12) Campagna, S.; Puntoriero, F.; Nastasi, F.; Bergamini, G.; Balzani, V. *Top. Curr. Chem.* **2007**, *280*, 117.
- (13) Meyer, T. J. *Pure Appl. Chem.* **1986**, *58*, 1193.
- (14) Thompson, D. W.; Wishart, J.; Brunschwig, B.; Sutin, N. *J. Phys. Chem. A* **2001**, *105*, 8117.
- (15) Harriman, A.; Izzet, G.; Goeb, S.; Nicola, A. D.; Ziessel, R. *Inorg. Chem.* **2006**, *45*, 9729.

- (16) Qu, P.; Thompson, D. W.; Meyer, G. J. *Langmuir* **2000**, *16*, 4662.
- (17) Cannizzo, A.; van Mourik, F.; Gawelda, W.; Zgrablic, G.; Bressler, C.; Chergui, M. *Angew. Chem. Int. Ed.* **2006**, *45*, 3174.
- (18) Daul, C.; Baerends, E. J.; Vernooijs, P. *Inorg. Chem.* **1994**, *33*, 3538.
- (19) Lytle, F. E.; Hercules, D. M. *J. Am. Chem. Soc.* **1969**, *91*, 253.
- (20) Crosby, G. A.; Demas, J. N. *J. Am. Chem. Soc.* **1971**, *93*, 2841.
- (21) Yoon, S.; Kukura, P.; Mathies, R. A.; Stuart, C. M. *Mol. Phys.* **2006**, *104*, 1275.
- (22) Kober, E. M.; Meyer, T. J. *Inorg. Chem.* **1984**, *23*, 3877.
- (23) Sykora, M.; Kincaid, J. *Inorg. Chem.* **1995**, *34*, 5852.
- (24) Crosby, G. A. *Acc. Chem. Res.* **1975**, *8*, 231.
- (25) Harrigan, R. W.; Crosby, G. A. *J. Chem. Phys.* **1973**, *59*, 3468.
- (26) Hager, G. D.; Crosby, G. A. *J. Am. Chem. Soc.* **1975**, *97*, 7031.
- (27) Hager, G. D.; Watts, R. J.; Crosby, G. A. *J. Am. Chem. Soc.* **1975**, *97*, 7037.
- (28) Hipps, K. W.; Crosby, G. A. *J. Am. Chem. Soc.* **1975**, *97*, 7042.
- (29) Crosby, G. A.; Elfring, W. H. *J. Phys. Chem.* **1976**, *80*, 2206.
- (30) Rillema, D.; Blanton, C.; Shaver, R.; Jackman, D.; Boldaji, M.; Bundy, S.; Worl, L.; Meyer, T. J. *Inorg. Chem.* **1992**, *31*, 1600.
- (31) Tachiyashiki, S.; Ikezawa, H.; Mizumachi, K. *Inorg. Chem.* **1994**, *33*, 623.
- (32) Van Houten, J.; Watts, R. *J. Am. Chem. Soc.* **1976**, *98*, 4853.
- (33) Islam, A.; Ikeda, N.; Yoshimura, A.; Ohno, T. *Inorg. Chem.* **1998**, *37*, 3093.
- (34) Barqawi, K.; Llobet, A.; Meyer, T. J. *J. Am. Chem. Soc.* **1988**, *110*, 7751.
- (35) Anderson, P.; Strouse, G. F.; Treadway, J. A.; Keene, F.; Meyer, T. J. *Inorg. Chem.* **1994**, *33*, 3863.
- (36) Kolemen, S.; Bozdemir, O. A.; Cakmak, Y.; Barin, G.; Erten-Ela, S.; Marszalek, M.; Yum, J.-H.; Zakeeruddin, S. M.; Nazeeruddin, M. K.; Grätzel, M.; Akkaya, E. U. *Chem. Sci.* **2011**, *2*, 949.
- (37) Thompson, D. W.; Fleming, C. N.; Myron, B. D. B.; Meyer, T. J. *J. Phys. Chem. B* **2007**, *111*, 6930.

- (38) Meylemans, H.; Lei, C.-F.; Damrauer, N. H. *Inorg. Chem.* **2008**, *47*, 4060.
- (39) Davis, W. B.; Ratner, M. A.; Wasielewski, M. R. *J. Am. Chem. Soc.* **2001**, *123*, 7877.
- (40) Meylemans, H. A.; Damrauer, N. H. *Inorg. Chem.* **2009**, *48*, 11161.
- (41) Chen, P.; Curry, M.; Meyer, T. J. *Inorg. Chem.* **1989**, *28*, 2271.
- (42) Damrauer, N. H.; McCusker, J. K. *Inorg. Chem.* **1999**, *38*, 4268.
- (43) Deb, S.; Maddux, T.; Yu, L. *J. Am. Chem. Soc.* **1997**, *119*, 9079.
- (44) Gillaizeau-Gauthier, I.; Odobel, F.; Alebbi, M.; Argazzi, R.; Costa, E.; Bignozzi, C.; Qu, P.; Meyer, G. *Inorg. Chem.* **2001**, *40*, 6073.
- (45) Sullivan, B. P.; Salmon, D. J.; Meyer, T. J. *Inorg. Chem.* **1978**, *17*, 3334.
- (46) Sullivan, B. P.; Salmon, D. J.; Meyer, T. J. *Inorg. Chem.* **1978**, *17*, 3334.
- (47) *Polymer Handbook*; 3rd ed.; Brandrup, J. I.; Immergut, E. H., Eds.; Wiley and Sons: New York, 1989.
- (48) Thompson, D. W.; Fleming, C. N.; Myron, B.; Meyer, T. J. *J. Phys. Chem. B* **2007**, *111*, 6930.
- (49) Victor, J. G.; Torkelson, J. M. *Macromolecules* **1987**, *20*, 2241.
- (50) Naito, T.; Horie, K.; Mita, I. *Macromolecules* **1991**, *24*, 2907.
- (51) Tanabe, Y.; Müller, N.; Fischer, E. W. *Polymer Journal* **1984**, *16*, 445.
- (52) Williams, G.; Watts, D. C.; Dev, S. B.; North, A. M. *Trans. Faraday Soc.* **1971**, *67*, 1323.
- (53) Williams, G.; Watts, D. C. *Trans. Faraday Soc.* **1970**, *66*, 80.
- (54) Devenney, M.; Worl, L. A.; Gould, S.; Guadalupe, A.; Sullivan, B. P.; Caspar, J. V.; Leasure, R. L.; Gardner, J. R.; Meyer, T. J. *J. Phys. Chem. A* **1997**, *101*, 4535.
- (55) Hecker, C. R.; Fanwick, P. E.; McMillin, D. R. *Inorg. Chem.* **1991**, *30*, 659.
- (56) Kincaid, J. R. *Chem. Eur. J.* **2000**, *6*, 4055.
- (57) Campagna, S.; Bartolotta, A.; Di Marco, G. *Chem. Phys. Lett.* **1993**, *206*, 30.
- (58) Masschelein, A.; Mesmaeker, A.; Willsher, C.; Wilkinson, F. *J. Chem. Soc., Faraday Trans.* **1991**, *87*, 259.

- (59) Mongey, K.; Vos, J.; MacCraith, B.; McDonagh, C. *Coord. Chem. Rev.* **1999**, *185-186*, 417.
- (60) Jones, W. A.; Chen, P.; Meyer, T. J. *J. Am. Chem. Soc.* **1992**, *114*, 387.
- (61) Pfennig, B. W.; Chen, P.; Meyer, T. J. *Inorg. Chem.* **1996**, *35*, 2898.
- (62) Maeder, M.; Zuberbühler, A. D. *Anal. Chem.* **1990**, *62*, 2220.
- (63) Stultz, L. K.; Binstead, R. A.; Reynolds, M. S.; Meyer, T. J. *J. Am. Chem. Soc.* **1995**, *117*, 2520.
- (64) ReactLab Kinetics User Manual, JPlus Consulting Pty. Ltd.
- (65) Claude, J. P.; Omberg, K.; Williams, D.; Meyer, T. J. *J. Phys. Chem. A* **2002**, *106*, 7795.
- (66) Kestell, J.; Williams, Z.; Stultz, L.; Claude, J. P. *J. Phys. Chem. A* **2002**, *106*, 5768.
- (67) Claude, J. P.; Williams, D.; Meyer, T. J. *J. Am. Chem. Soc.* **1996**, *118*, 9782.
- (68) Parker, C. A.; Rees, W. T. *The Analyst* **1960**, *85*, 587.
- (69) Claude, J. P. Ph.D. Dissertation, University of North Carolina at Chapel Hill, 1995.
- (70) Caspar, J. V.; Meyer, T. J. *Inorg. Chem.* **1983**, *22*, 2444.
- (71) Caspar, J. V.; Meyer, T. J. *J. Am. Chem. Soc.* **1983**, *105*, 5583.
- (72) Kober, E. M.; Caspar, J. V.; Lumpkin, R. S.; Meyer, T. J. *J. Phys. Chem.* **1986**, *90*, 3722.
- (73) Ikeyama, T.; Azumi, T. *J. Phys. Chem.* **1985**, *89*, 5332.
- (74) Kober, E. M.; Sullivan, B. P.; Meyer, T. J. *Inorg. Chem.* **1984**, *23*, 2098.
- (75) Caspar, J. V.; Westmoreland, T. D.; Allen, G. H.; Bradley, P. G.; Meyer, T. J.; Woodruff, W. H. *J. Am. Chem. Soc.* **1984**, *106*, 3492.
- (76) Kober, E. M.; Caspar, J.; Lumpkin, R. S.; Meyer, T. J. *J. Phys. Chem.* **1986**, *90*, 3722.
- (77) Strouse, G. F.; Schoonover, J.; Duesing, R.; Boyde, S.; Jones, W. A.; Meyer, T. J. *Inorg. Chem.* **1995**, *34*, 473.
- (78) Halim, M.; Pillow, J.; Samuel, I.; Burn, P. *Synth. Met.* **1999**, *102*, 922.

- (79) Díez-Barra, E.; García-Martínez, J.; Merino, S.; del Rey, R.; Rodríguez-López, J.; Sánchez-Verdú, P.; Tejada, J. *J. Org. Chem.* **2001**, *66*, 5664.
- (80) Halim, M.; Pillow, J.; Samuel, I.; Burn, P. *Adv. Mater.* **1999**, *11*, 371.
- (81) Juris, A. *Annu. Rep. Prog. Chem., Sect. C* **2003**, *99*, 177.
- (82) Pálsson, L.-O.; Beavington, R.; Frampton, M. J.; Lupton, J. M.; Magennis, S. W.; Markham, J. P. J.; Pillow, J. N. G.; Burn, P. L.; Samuel, I. D. W. *Macromolecules* **2002**, *35*, 7891.
- (83) Devadoss, C.; Bharathi, P.; Moore, J. S. *J. Am. Chem. Soc.* **1996**, *118*, 9635.
- (84) Sension, R. J.; Repinec, S. T.; Szarka, A. Z.; Hochstrasser, R. M. *J. Chem. Phys.* **1993**, *98*, 6291.
- (85) Chen, P.; Meyer, T. J. *Chem. Rev.* **1998**, *98*, 1439.
- (86) Dattelbaum, D. M.; Kober, E. M.; Papanikolas, J. M.; Meyer, T. J. *Chem. Phys.* **2006**, *326*, 71.
- (87) Kober, E. M.; Sullivan, B. P.; Meyer, T. J. *Inorg. Chem.* **1984**, *23*, 2098.
- (88) Waldeck, D. H. *Chem. Rev.* **1991**, *91*, 415.
- (89) Fuß, W.; Kosmidis, C.; Schmid, W. E.; Trushin, S. A. *Angew. Chem. Int. Ed.* **2004**, *43*, 4178.
- (90) Dou, Y.; Wu, W.; Tang, H.; Allen, R. *Chem. Phys.* **2008**, *353*, 104.
- (91) Yam, V. W.; Yang, Y.; Zhang, J.; Chu, B. W.; Zhu, N. *Organometallics* **2001**, *20*, 4911.
- (92) Houjeiry, T. I.; Ghaddar, T. H. *Chem. Phys. Lett.* **2008**, *460*, 543.
- (93) Mizutani, T.; Ikegami, M.; Nagahata, R.; Arai, T. *Chem. Lett.* **2001**, *30*, 1014.
- (94) Oh, D. H.; Boxer, S. G. *J. Am. Chem. Soc.* **1989**, *111*, 1130.
- (95) Oh, D. H.; Sano, M.; Boxer, S. G. *J. Am. Chem. Soc.* **1991**, *113*, 6880.
- (96) Kasha, M. *Discuss. Faraday Soc.* **1950**, *9*, 14.
- (97) Keyes, T. E.; O'Connor, C.; Vos, J. G. *Chem. Commun.* **1998**, 889.
- (98) Keyes, T. E.; O'Connor, C. M.; O'Dwyer, U.; Coates, C. G.; Callaghan, P.; McGarvey, J. J.; Vos, J. G. *J. Phys. Chem. A* **1999**, *103*, 8915.

- (99) Song, L.-Q.; Feng, J.; Wang, X.-S.; Yu, J.-H.; Hou, Y.-J.; Xie, P.-H.; Zhang, B.-W.; Xiang, J.-F.; Ai, X.-C.; Zhang, J.-P. *Inorg. Chem.* **2003**, *42*, 3393.
- (100) Tyson, D. S.; Luman, C. R.; Zhou, X.; Castellano, F. N. *Inorg. Chem.* **2001**, *40*, 4063.
- (101) Baba, A. I.; Ensley, H. E.; Schmechl, R. H. *Inorg. Chem.* **1995**, *34*, 1198.
- (102) Zambrana, J. L.; Ferloni, E. X.; Colis, J. C.; Gafney, H. D. *Inorg. Chem.* **2008**, *47*, 2.
- (103) Glazer, E. C.; Magde, D.; Tor, Y. *J. Am. Chem. Soc.* **2005**, *127*, 4190.
- (104) Glazer, E.; Magde, D.; Tor, Y. *J. Am. Chem. Soc.* **2007**, *129*, 8544.
- (105) Meylemans, H.; Hewitt, J.; Abdelhaq, M.; Vallett, P.; Damrauer, N. H. *J. Am. Chem. Soc.* **2010**, *132*, 11464.

Chapter 3. Long-Lived Excited States in Benzyl- and Naphthyl-capped Fréchet-type Dendrimers with a Tris(Methyl Viologen) Core.

3.1 Introduction.

An investigation into the photophysical properties of two families of benzyl- and naphthyl-capped Fréchet-type dendrimers with a tris(methyl viologen) core revealed that these structures undergo rapid electron transfer from the dendron arms to the dendrimer core. Radical trapping by a strongly electron accepting methyl viologen unit yields a long-lived charge separated state in the absence of O_2 . In this Chapter, the physical and electronic properties of these dendrimers are discussed within the context of Energy Gap Law to account for these anomalously long-lived charge separated states.

3.1.1 Ground and Excited State Electronic Properties of Methyl Viologen.

1,1'-dimethyl-4,4'-bipyridinium ion, also known as methyl viologen (MV^{2+} , Figure 3.1), is most commonly (and infamously) known for its widespread use as the herbicide Paraquat. However, in the field of chemistry this compound is viewed rather differently and is employed in a broad array of applications and systems, such as for solar energy conversion, in optical and optoelectronic devices, as the key reactive species in the catalytic generation of hydrogen from cleavage of water, and as an important probe in electron transfer studies.¹⁻³ The versatility of MV^{2+} in these and other applications is a direct result of its unique electronic properties, as it not only has strong electron accepting character in the ground state but also has an extremely high excited-state reduction

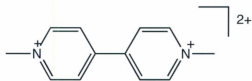


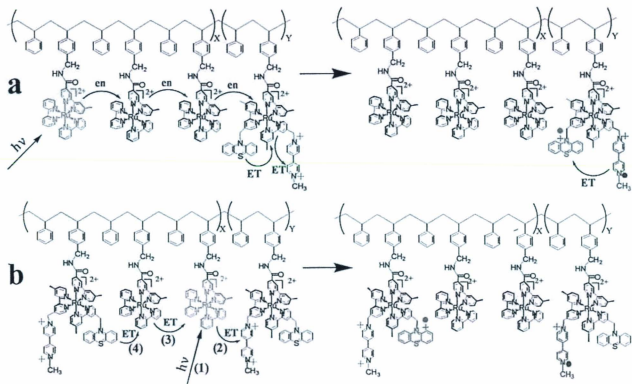
Figure 3.1 Structure of methyl viologen.

potential of $E^{\circ} (MV^{2+}/MV^{\bullet+}) = +3.65$ V following 266 nm excitation.¹ As a consequence, excited state MV^{2+*} is extremely reactive and is quenched by any species with a gas-phase ionization potential of 10.84 eV or less. This was demonstrated by femtosecond laser flash photolysis, whereby 265 nm excitation yielded the monoreduced cation radical form of methyl viologen ($MV^{\bullet+}$) by rapid excited state quenching by MeOH (gas-phase IP = 10.84 eV) within the ~180 fs resolution of the spectrometer.¹ Furthermore, due to the large electron affinity ($E_s = 1.24$ eV)⁵ of this compound, $MV^{\bullet+}$ is extremely stable and can persist in inert oxygen-free solvents for hours,⁶ though back E_LT occurs within 430 fs in MeOH. In the appropriate conditions MV^{2+} also acts as a two-electron acceptor.⁷ While MV^{2+} is non-emissive in solution, sterically-hindered derivatives of MV^{2+} have exhibited fluorescence, ostensibly by inhibiting rotational freedom about the C-C bond that interconnects the two pyridyl rings.^{8,9} The potent electron accepting nature of MV^{2+} is the origin of its herbicidal activity, as Paraquat acts by intercepting electrons from the plant's photosynthetic apparatus to yield $MV^{\bullet+}$ and then shunting them to molecular oxygen to yield the destructive superoxide radical anion (O_2^-), regenerating the dicationic MV^{2+} state in the process.¹⁰

3.1.2 MV^{2+} as an Electron Acceptor.

The potent electron acceptor character of methyl viologen makes it desirable for incorporation into systems designed for the study of electron transfer and/or electron capture. A succinct description of the utility of MV^{2+} as an acceptor site in polymeric structures was reported in laser flash photolysis studies of a polystyrene polymer derivatized with $[Ru(bpy)_2(bpy-CONH-)]^{2+}$ units for the purpose of mimicking the electron and energy transfer steps of photosynthesis. In this model system, the inclusion of electron donating phenothiazine (PTZ) and electron accepting MV^{2+} units on modified Ru^{II} polypyridyl chromophores was found to drive both electron ($E_L T$) and energy transfer ($E_N T$) in two separate but simultaneous kinetic processes.

First (as summarized in **Figure 3.2a**), excitation of a bound chromophoric $[Ru(bpy)_2(bpy-CONH-)](PF_6)_2$ unit in the polymer yields a highly energetic 3MLCT excited state (2.13 eV) that can sensitize a neighbouring chromophore through self-exchange $E_N T$ steps. This causes a propagation of this energy along the polymer by sequential $E_N T$ events, ultimately terminating in the "reaction centre model", a modified version of the aforementioned Ru^{II} polypyridyl chromophores that also contains one PTZ and one MV^{2+} group. Migration of energy to this site initiates $E_L T$ from the metal centre to the MV^{2+} , along with $E_L T$ to the metal centre from the PTZ unit. This reaction pathway is terminated by the eventual return of the electron from $MV^{\bullet+}$ to $PTZ^{\bullet+}$ by an intramolecular $E_L T$ which occurs in ~ 160 ns at 298 K in CH_3CN .



Scheme 3.2 Kinetic schemes describing (a) E_Nt and (b) E_Lt in a Ru^{II} polypyridyl-derivatized polymer, wherein both processes involve electron transfer to a MV^{2+} acceptor.⁴ Copyright © 2000, The National Academy of Sciences.

A second reaction pathway (Figure 3.2b) is also available under the same experimental conditions, wherein an $E_L T$ mechanism is responsible for forming an extremely long-lived ($\tau = 20.8$ ms) redox separated state. In this case, excitation of a chromophore (which yields a strongly reducing 3MLCT state) results in $E_L T$ to the electron accepting MV^{2+} unit of a neighbouring reaction centre model, followed by a second $E_L T$ process from an adjacent Ru^{II} polypyridyl centre to fill the hole on the oxidized Ru^{III} polypyridyl chromophore. In this way, the electron hole migrates away from the electron localized on the methyl viologen by sequential $Ru^{II} \rightarrow Ru^{III}$ self-exchange $E_L T$ steps, until such a time as it reaches a PTZ unit. At this point, $E_L T$ takes place from this potent electron donor and ultimately yields a long-lived charge separated state, with the electron and hole localized on isolated $MV^{\bullet+}$ and $PTZ^{\bullet+}$ groups, respectively. Intramolecular back electron transfer in this case is quite slow, and so charge recombination is instead mediated by diffusion, resulting in electron transfer between adjacent polymer chains.

3.1.3 MV^{2+} in Dendrimers.

Methyl viologen units are often used in dendritic polymers as well, and while examples do exist of their incorporation into the dendritic arms themselves,^{3,11,12} the potent electron accepting character of MV^{2+} makes it a common choice to serve as part of the central core of dendrimers capable of photoinduced electron transfer.^{7,13-17} Notably, while dendrimers derivatized with a redox-active core commonly show an inverse relationship between rates of electron transfer and molecular weight (and, thus, dendrimer size),^{15,18,19} dendrimers

employing MV^{2+} as the redox-active unit (such as in Figure 3.3) do not appear to experience the same attenuation of $E_L T$ due to isolation of the core with increasing dendrimer generation as is seen in other systems.¹⁴⁻¹⁶ While it has been theorized that the core of dendrimers containing MV^{2+} units are not as isolated as other such structures (suggesting that the effect does not manifest itself in these dendrimers simply because of inadequate dendron folding about the core),¹⁸ these rapid and electron transfer rates have nonetheless been observed in systems where folding of the dendrons about the core raises the reduction potential of the MV^{2+} acceptor to a less negative value.¹⁴

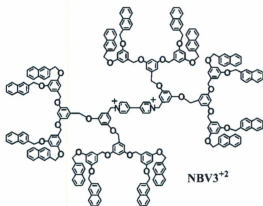


Figure 3.3 NBV3²⁺: an example of a 3rd generation, Fréchet-type MV^{2+} -cored dendrimer with naphthalene capping groups.⁷

Research into methyl viologen-cored, Fréchet-type dendrimers (as in Figure 3.3) with naphthalene terminal groups has revealed unusual transient absorption dynamics, wherein the appearance of growth kinetics and a long-lived transient species were found to be dependent on the laser power of the excitation source (Figure 3.4a).⁷ These results were

attributed to back electron transfer from a doubly-reduced methyl viologen core to a 1,3-dimethyleneoxybenzene group to yield strongly absorbing $MV^{\bullet+}$, as the absorption of multiple photons by the dendrons that is required for two-electron reduction of the MV^{2+} core is dependent on laser power (Figure 3.4b). This is an important result, as while it is known that a central MV^{2+} unit can accept two electrons *via* sequential one-electron injections,^{12,20} this is the first demonstration of simultaneous two-electron injection in this application, thus demonstrating the potential for using such systems to act as redox centres for multielectron reactions, such as those required for realizing the lofty goal of developing a device capable of carrying out artificial photosynthesis.^{21,22}

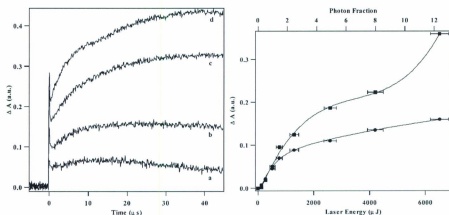


Figure 3.4 (left) Transient absorption decay of $NB3V^{2+}$ in CH_2Cl_2 at 600 nm following 266 nm excitation. The increase in ΔA from a – d corresponds to increasing laser power intensities (270 μJ , 520 μJ , 765 μJ , and 1.3 mJ, respectively.) (right) Plot of ΔA vs. laser power for $NB3V^{2+}$ at 600 nm, taken after (circles) 10 ns and (squares) 20 ns.⁷ Adapted with permission from ref 7. Copyright © 2002 American Chemical Society.

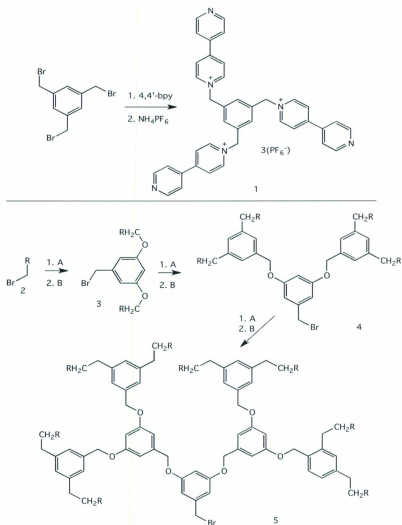
3.2 Experimental Details.

3.2.1 Materials.

CHCl_3 (ACP) and CH_3CN (ACS grade, ACP; UV B&J Brand grade, Honeywell Burdick & Jackson) were used as received.

3.2.2 Synthesis.

All compounds were synthesized by Dr. Ghaddar's research group at AUB by the procedures described in Figures 3.5 – 3.7. The products of these syntheses are systematically named by the general scheme XB_nV^{6+} , where X determines the terminal group (B = benzene, N = naphthalene), B denotes 1,3-bis(methyleneoxy)benzene, the type of monomer used to prepare the body of the dendrimer; n corresponds to the dendrimer generation, ranging from 0 to 3; and V^{6+} represents the tris(methyl viologen) core unit (three MV^{2+} units = 6+ total charge).



A = 3,5-dihydroxybenzyl alcohol, K_2CO_3 in dry acetone
 B = CBr_4 and PPh_3 in dry THF. R = Ph for BBnV^{6+} , Np for NBnV^{6+}

Figure 3.5 Synthesis of the tris(methyl viologen) core (1) and of the dendron arms for dendrimer generations 0 – 3 (structures 2 – 5).

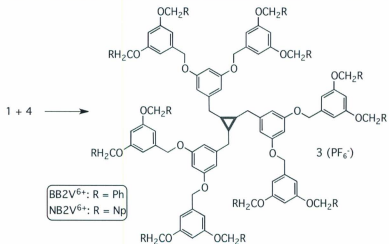
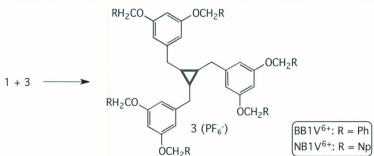
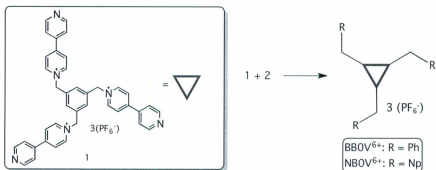


Figure 3.6 Synthesis of BB n V⁶⁺ and NB n V⁶⁺ ($n = 0 - 2$).

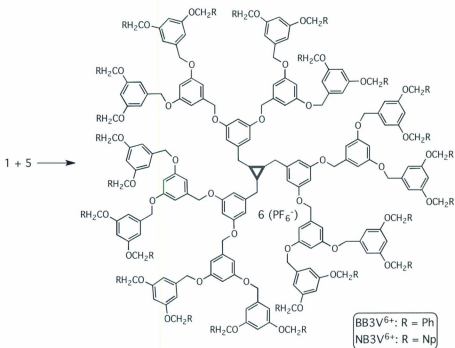


Figure 3.7 Synthesis of BB3V⁶⁺ and NB3V⁶⁺.

3.2.3 Instrumentation and Methods.

Details of instrumentation and sample preparation are as stated in Chapter 2, unless otherwise listed here.

Sample Preparation. Dendrimer solutions were prepared in a higher concentration than usual at the excitation wavelength ($A @ 266 \text{ nm} \sim 1$, versus a typical absorbance of 0.15) due to signal-to-noise concerns.

Laser flash photolysis. Laser flash photolysis of dilute solutions of BB0V^{6+} , BB2V^{6+} , and $\text{NB}n\text{V}^{6+}$ ($n = 0 - 2$) in CH_3CN and NB3V^{6+} in CHCl_3 was carried out using a spectrometer that was configured for collinear excitation by a 266 nm excitation source. The excitation line was produced from the fundamental laser line ($\lambda_{\text{exc}} = 1064 \text{ nm}$) of the Nd:YAG laser described in Chapter 2, using a combination of second and fourth harmonic generating crystals. The excitation beam passed through a prism that redirected the incident laser light such that it was collinear with the xenon arc lamp output, which has the effect of exciting more molecules that lie in the path of the probe beam and thereby increasing the ΔA signal relative to that acquired in a traditional perpendicular pump-probe alignment.

3.3 Results

3.3.1 Absorbance Spectra.

Table 3.1 Absorbance data of BB_nV^{6+} ($n = 0, 2$) and NB_nV^{6+} ($n = 0 - 2$) in CH_3CN .

$\lambda_{\text{max}}^{\text{abs}}, \text{nm} (E_{\text{abs}}, \text{cm}^{-1})$				
BB0V^{6+}	BB2V^{6+}	NB0V^{6+}	NB1V^{6+}	NB2V^{6+}
261 (38,310)	207 (48,310)	217 (46,080)	217 (46,080)	210 (47,620)
	230 (43,480)	222 (45,050)	225 (44,440)	225 (44,440)
	261 (38,310)	262 (38,170)	266 (37,590)	254 (39,370)
	275 (36,360)	275 (36,360)	273 (36,630)	264 (37,880)
				274 (36,500)

The absorbance spectra of BB_nV^{6+} and NB_nV^{6+} in CH_3CN are shown in Figure 3.8 and their wavelengths and energies of maximum absorbance are summarized in Table 3.1. Both sets of spectra are characterized by a benzene or naphthalene $\pi \rightarrow \pi^*$ transition at ~ 200 nm, a 1,3-bis(methyleneoxy)benzene $\pi \rightarrow \pi^*$ band at ~ 220 nm and a broad methyl viologen $\pi \rightarrow \pi^*$ absorbance centred at ~ 260 nm. Small differences in the wavelengths at which these bands are evident from generation to generation, and are likely due to a solvational effect arising from the varying conformational degrees of freedom of the dendrimer. The tris(methyl viologen) core is unchanged from generation to generation, and this is reflected in the MV^{2+} absorbance bands that are largely invariant (with the exception of a slight bathochromic shift) with increasing generation; however, the benzyl/naphthyl and 1,3-bis(methyleneoxy)benzene bands do indeed scale with the growth in dendrimer size and complexity. The spectra showed little photoinduced change upon irradiation by either a Xe arc lamp or 266 nm

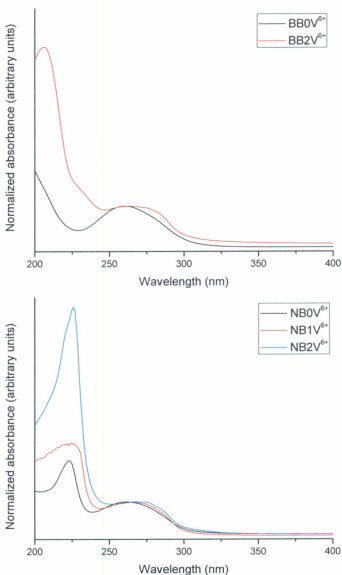


Figure 3.8 UV-Visible absorbance spectra of $BBnV^{6+}$ ($n = 0, 2$) (top) and $NBnV^{6+}$ ($n = 0 - 2$) (bottom) in CH_3CN at (298 ± 3) K. Spectra were normalized to the maximum absorbance of the MV^{2+} -based band centred at ~ 260 nm.

Nd:YAG laser excitation source. Those changes that were observed are addressed in detail in the **Discussion**. These bands did not yield an appreciable amount of fluorescence in either the $\text{BB}n\text{V}^{6+}$ or the $\text{NB}n\text{V}^{6+}$ compounds, as ascertained by a steady-state spectrofluorometer. However, some emission is observed in nanosecond fluorescence decay and laser flash photolysis experiments, indicating that excitation into these $\pi \rightarrow \pi^*$ transitions leads to emission with very small quantum yields.

3.3.2 Laser Flash Photolysis.

Table 3.2 Transient absorption decay lifetimes¹ for $\text{BB}n\text{V}^{6+}$ and $\text{NB}n\text{V}^{6+}$ dendrimers.

		400 nm	590 nm
BB0V^{6+}	τ_1	$(13.2 \pm 0.4) \mu\text{s}$	See footnote 2
	τ_2	-	-
BB2V^{6+}	τ_1	$(22 \pm 21) \text{ ns}$	$(34 \pm 12) \text{ ns}$
	τ_2	$(190 \pm 70) \text{ ns}$	$(220 \pm 50) \text{ ns}$
NB0V^{6+}	τ_1	$(39 \pm 7) \text{ ns}$	$(110 \pm 20) \text{ ns}$
	τ_2	$(370 \pm 40) \text{ ns}$	-
NB1V^{6+}	τ_1	$(33 \pm 3) \text{ ns}$	$(47 \pm 6) \text{ ns}$
	τ_2	$(330 \pm 40) \text{ ns}$	$(1.25 \pm 0.81) \mu\text{s}$
NB2V^{6+}	τ_1	$(190 \pm 140) \text{ ns}^3$	$(140 \pm 20) \text{ ns}^3$
	τ_2	$(2.1 \pm 4.3) \mu\text{s}^3$	-
NB3V^{6+} (in CHCl_3)	τ_1	$(84 \pm 5) \text{ ns}$	$(90 \pm 14) \text{ ns}$
	τ_2	$(480 \pm 50) \text{ ns}$	$(630 \pm 290) \text{ ns}$

¹ All reported lifetimes at 400 and 590 nm preceded a long-lived transient absorption that exceeded the time resolution capabilities of the spectrometer.

² No decay process observed. ³ Poor signal strength resulted in questionable data.

All compounds showed biphasic transient absorption decay behaviour upon 266 nm excitation. At 400 nm in the NB0V⁶⁺ and NB1V⁶⁺ dendrimers, transient absorption kinetics were biphasic with a short-lived component and a long-lived transient that exceeded the detection limits of the spectrometer (Table 3.2). This biphasic decay was quite prominent at both 400 nm and 590 nm (Figure 3.9), but the intensity of the transient absorption signal was observed to increase at 400 nm and decrease at 590 nm with dendrimer generation. The TA decay behaviour of BB2V⁶⁺ in Men (Figure 3.10) was similar to that of the NB n V⁶⁺ dendrimers, at least within the margins of error. Unfortunately, the small ΔA and large signal-to-noise ratios in the transient absorption data were endemic throughout these experiments, leading to larger-than-expected margins of error. As mentioned in the **Experimental**, solutions were prepared with relatively high concentrations and collinear excitation was employed to overcome this obstacle. Furthermore, the experiments were complicated by a long-lived transient that did not return to pre-excitation levels using the lowest repetition rate available on the spectrometer. Therefore, the kinetic data were acquired with one laser shot at a time (that is, without averaging), yielding poor signal-to-noise ratios. With these facts in mind the interpretation of these results was carried out on a primarily qualitative basis. A solution of the largest dendrimer NB3V⁶⁺ was prepared in CHCl₃ (see Figure 3.9 for a representative TA decay trace) due to its insolubility in CH₃CN, but for this reason it was not investigated at length.

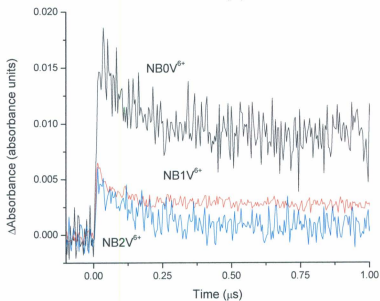
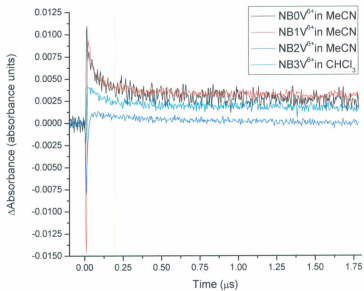


Figure 3.9 Transient absorption decay of $\text{NB}n\text{V}^{6+}$ in CH_3CN at 400 nm (top) and 590 nm (bottom) upon 266 nm collinear excitation at (298 ± 3) K.

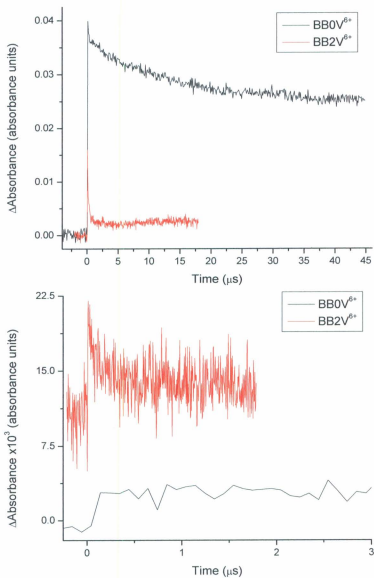


Figure 3.10 Transient absorption decay of BB0V⁶⁺ and BB2V⁶⁺ in CH₃CN at 400 nm (top) and 590 nm (bottom) upon 266 nm collinear excitation ((298 ± 3) K, 1 atm N₂).

Initially, no fluorescence was detected from any of the dendrimers as determined by steady-state emission spectrum measurements. However, laser flash photolysis of the $\text{NB}n\text{V}^{6+}$ ($n = 1 - 3$) dendrimers at 400 nm upon 266 nm excitation shows an extremely short-lived fluorescence that is convoluted with the excitation pulse and that precedes the previously reported biphasic transient absorption results (Figure 3.11). This observation is addressed in more detail in the Discussion.

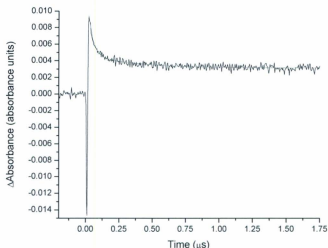


Figure 3.11 Laser flash photolysis of NB1V^{6+} in CH_3CN at 400 nm upon 266 nm collinear excitation at (298 ± 3) K.

The excited state dynamics of BB0V^{6+} in CH_3CN (Figure 3.10) differ from that of the other dendrimers in several ways. First, while this compound also demonstrated a long-lived absorption signal at 590 nm, there was no initial observable decay process like those observed for the larger dendrimers in the transient absorption decay trace; second, the TA

decay trace collected at 400 nm had a lengthy exponential decay ($\tau = 1.32 \times 10^{-5}$ s) that preceded the long-lived transient signal; and third, the transient absorption signal of this compound was observed to be increasing upon multiple excitation pulses.

3.4 Discussion.

3.4.1 Spectroscopy of $BBnV^{6+}$ and $NBnV^{6+}$.

3.4.1.1 Laser Flash Photolysis of $BB2V^{6+}$ and $NBnV^{6+}$ ($n = 0 - 2$) in CH_3CN .

Broadly speaking, the results of the laser flash photolysis experiments are quite similar for both the benzene- and naphthalene-capped dendrimers studied, with the exception of $BB0V^{6+}$. The $BB2V^{6+}$ and $NBnV^{6+}$ ($n = 0 - 3$) dendrimers all exhibit biphasic kinetics on surprisingly long timescales. As previously discussed, the longevity of these excited states, along with their weak response to the laser flash photolysis experiment, made measurement and interpretation of the kinetics somewhat challenging, as exemplified by the uncertainties surrounding some of the calculated decay lifetimes posted in Table 3.1.

Despite these difficulties, these compounds exhibit rather interesting excited state kinetics that warrant further investigation. A comparison of the relative intensities of the laser flash photolysis data collected for the $NBnV^{6+}$ series hints at the possibility that the underlying kinetics are rather more complicated than they first seem. For example, while Figure 3.12 demonstrates that $NB0V^{6+}$ and $NB1V^{6+}$ exhibit similar decay kinetics and have similar ΔA values at 400 nm, the relative intensity of the long-lived component of the $NB0V^{6+}$ transient absorption is approximately 4 times larger than that of $NB1V^{6+}$ at

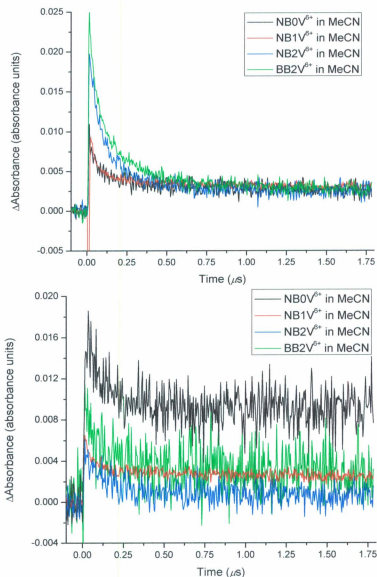


Figure 3.12 Laser flash photolysis of BB2V^{6+} and NB_nV^{6+} ($n = 0 - 2$) in CH_3CN at 400 nm (top) and 590 nm (bottom) upon 266 nm collinear excitation at (298 ± 3) K.

590 nm, which is instead comparable to that of NB2V^{6+} . This indicates that while the NB0V^{6+} and NB1V^{6+} dendrimers may share common structural features and a similar initial kinetic feature, it is clear that the details of the kinetic process responsible for the long-lived transient absorption (or, the kinetic process itself) are not the same.

Furthermore, laser flash photolysis of BB2V^{6+} in CH_3CN yields rather similar kinetics as seen for NB1V^{6+} and NB2V^{6+} in the same experimental conditions. Thus, it would appear from these results that not only is the NB0V^{6+} species rather unlike the remaining $\text{NB}n\text{V}^{6+}$ dendrimers, but that they and the BB2V^{6+} dendrimers are much more similar to each other than to NB0V^{6+} ; it is apparent that there is a property of NB0V^{6+} that sets it apart from all the other benzene- and naphthalene-capped dendrimers that have been discussed thusfar.

3.4.1.2 UV-Visible Spectroscopy and Laser Flash Photolysis of BB0V^{6+} in CH_3CN .

In light of these laser flash photolysis results, it would seem that the anomalous kinetics of the BB0V^{6+} dendrimer are somewhat less unusual and that, in some ways, both of the zeroth-generation dendrimers exhibit similar behavior. With that said, laser flash photolysis of BB0V^{6+} still yields unique excited state dynamics that were not matched by any of the other dendrimers, such as the absence of biphasic kinetics in the transient absorption of this compound at 590 nm.

The observation of increasing transient absorbance of BB0V^{6+} upon repeated excitations is particularly interesting, as it may indicate that photochemical changes may

have been taking place or that the transiently absorbing BBOV^{6+} species had not relaxed back to the ground state by the time the next excitation pulse was provided, causing an increase in the total ΔA signal with each measurement. This effect was quite profound, and given that each of these dendrimers exhibit extremely long-lived excited states, the ground state UV-Visible absorbance spectra were acquired using a UV-Visible spectrophotometer before and after 266 nm excitation of this compound. These measurements revealed that not only were there small but observable spectral changes upon excitation, but that the resultant spectral changes were not permanent; rather, they seemed to persist for several minutes. By periodically measuring the rate of change in the UV-Visible spectrum of the solution at 400 nm, it was determined that the product of a single 266 nm excitation pulse had a lengthy decay lifetime of $\tau = \sim 5000$ s (Figure 3.13). The combination of the observed wavelengths of maximum absorbance (i.e. $\lambda_{\text{abs}} \sim 400$ and 590-600 nm) and the extremely long duration of this excited state strongly indicate that the species responsible for these spectral changes is the methyl viologen cation radical $\text{MV}^{\bullet+}$.^{1,23} Thus, it would appear that 266 nm excitation of these dendrimers ultimately results in long-term electron trapping in the tris(methyl viologen) core, though it is not clear at this time whether multiple MV^{2+} species are being reduced or if only a single electron is being injected into the electron acceptor core.

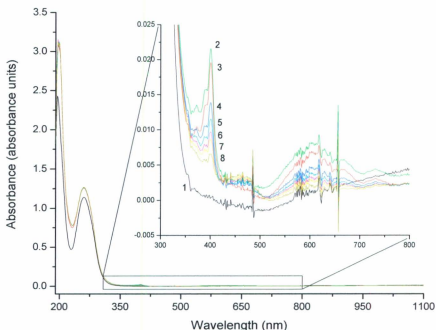


Figure 3.13 Absorbance spectra of BB0V^{6+} in CH_3CN following a single 266 nm excitation pulse ((298 ± 3) K, 1 atm N_2). Spectra were acquired periodically over 10 minutes in the order 1-8. (Inset: Baseline magnified to show spectral changes with time.)

3.4.2 Charge Trapping in a Tris(Methyl Viologen) Acceptor Core.

3.4.2.1 Long-Lived Transient Absorption of $\text{MV}^{\bullet+}$ Cation Radical at 590 nm.

Ultimately, 266 nm excitation of the BB_nV^{6+} and NB_nV^{6+} dendrimers in CH_3CN yields at least one long-lived monoreduced methyl viologen moiety in the dendrimer core, meaning that the $\text{MV}^{\bullet+}$ is acting as the electron acceptor in a donor-acceptor (D-A) or donor-bridge-acceptor (D-B-A) formalism. However, the absorbance spectra of these compounds show that the absorbance band being probed by a 266 nm excitation source

corresponds to a transition that is localized within the tris(methyl viologen) core, and not on the dendrimer arms. Therefore, the observed excited state kinetics and electron transfer dynamics originate from the acceptor core rather than the donor dendritic arms, and charge trapping in these chromophores-quencher compounds is the result of hole transfer from the MV^{2+} acceptors to the dendrimer.

As illustrated in **Figure 3.10**, laser flash photolysis of $BB0V^{6+}$ in CH_3CN yields an extremely long-lived transient absorption signal that does not appear to deteriorate within a useful observable timescale for measurement by the laser flash photolysis spectrometer, and subsequent measurement of this species by ground-state UV-Visible spectrophotometry has assigned this absorbance as being due to the $MV^{\bullet+}$ cation radical. However, in comparing this data with that of $NBnV^{6+}$ ($n = 0 - 2$) and $BB2V^{6+}$ in CH_3CN (**Figure 3.11**), it is apparent that these latter decay traces differ in that they exhibit biphasic kinetics under the same experimental conditions, where an initial decay of $\tau \sim 50 - 100$ ns precedes the familiar long-lived absorbance of $BB0V^{6+}$. Thus, the fact that an initial decay process was observed in all the dendrimers, save for $BB0V^{6+}$, leads to the conclusion that these results are due to a property that is intrinsic to (or at least more readily observed and most strongly expressed in) the zeroth-order dendrimers in $BB0V^{6+}$, the smallest of all the molecules studied.

3.4.2.2 Biphasic Transient Absorption Kinetics at 400 nm.

The excited state dynamics on display in the transient absorption decay traces of these dendrimers at 400 nm are similar to those acquired at 590 nm, but important differences are nonetheless observed. Each of the TA traces collected at 400 nm (for all dendrimers except BB0V⁶⁺) not only exhibited long-lived absorbances, but these features all had similar values of ΔA . This suggests a common origin for this feature in each of the different molecules, irrespective of dendrimer generation, and given the similarity of this absorbance to that observed at 590 nm this signal is almost certainly also due to the MV^{•+} species, which is known to strongly absorb at both of these wavelengths.¹ These quasi-stable absorbances are each preceded by a more rapid exponential decay process of $\tau \sim 30 - 40$ ns, values that are similar to what was observed at 590 nm. While there is little evidence of a trend across molecules in these decay processes at either wavelength, the lifetimes are somewhat consistent within each molecule at both wavelengths, and though attempting to quantify this data is a questionable practice for previously-stated reasons, these similar decay rates seem to provide limited evidence to support the assertion that the rapid exponential decays at 400 and 590 nm are in fact both due to the same kinetic process. Given the wavelengths at which this occurs and the variability of the molecules that exhibit this similar behavior, it is reasonable to assume that this process is due to loss of MV^{•+} cation radical absorbance. In the absence of compelling evidence one can speculate that this decay process could be due to reverse hole transfer or by quenching *via*

an undesirable side reaction, though it could also be the result of electron-hole recombination from a doubly- or triply- reduced acceptor core.

This hypothesis has thus far been considered in the absence of the transient absorption decay traces of BB0V^{6+} in CH_3CN . As shown in Figure 3.10, the rate of decay of the initial "short-lived" component at 400 nm is more than 50 times slower for BB0V^{6+} relative to these properties in BB2V^{6+} . This anomalous decay lifetime could have two possible origins: either (a), given that the long-lived absorbance of BB0V^{6+} persists for minutes at a time, perhaps an increase in the lifetime of the initial rapid decay of the $\text{MV}^{•+}$ could and should be expected; or (b), this decay process is due to a second species that is present in BB0V^{6+} but not any of the other dendrimers. Of these two options, (a) initially seems to present the most reasonable and plausible scenario. However, if this signal is indeed due to an attenuated rate of quenching of the $\text{MV}^{•+}$ cation radical, then, based on the data collected for the other dendrimers, the same exponential decay process should be observed at 590 nm; the data clearly demonstrate that this is not the case. Therefore, either this invocation of an attenuated rate of decay is incorrect, or the assignment of the decay process at 400 and 590 nm as being due to $\text{MV}^{•+}$ was incorrect. For these (and other) reasons, in attempting to explain the unusual photophysics of BB0V^{6+} , the assignment of this absorbance as being due to a hypothetical second excited state must be carefully considered.

3.4.2.3 Electron Transfer in $BBnV^{6+}$ and $NBnV^{6+}$.

Up to this point, the role of the dendrimer arms as electron donors and their involvement in the excited state dynamics of the tris(methyl viologen) core has been ignored. While the Discussion has thus far focused on the generation of the $MV^{\bullet+}$ cation radical species, it is important to remember that the hole transfer required to produce this molecule results in the oxidation of some donor group, and thus the nature of this species before and after photoexcitation must factor strongly into the longevity of the charge separated state. By discussing the dynamics of electron transfer in the dendrimers of the 1st to 3rd generations, this Section aims to determine what property of the $BB0V^{6+}$ (and to a lesser extent, $NB0V^{6+}$) dendrimer is responsible for yielding such unique and atypical excited state dynamics upon excitation of the tris(methyl viologen) core.

Formation of the $MV^{\bullet+}$ cation radical in these dendrimers is accomplished by electron hole transfer *via* the oligomeric backbone to an appropriate hole acceptor. Examining the structure of the dendrimers of 1st generation or greater, we see that each molecule is composed of two types of structural moieties: "benzyl ether" (i.e. 1,3-bis(methyleneoxy)benzene) groups (BnO) and naphthalene or benzene capping groups (Np or Ph). Either of these functional groups can act as an electron donor source for the tris(methyl viologen) core to yield a charge separated biradical state, resulting in the formation of either a $[MV^{\bullet+}/BnO^{\bullet+}]$ or, eventually, a $[MV^{\bullet+}/Np^{\bullet+}(\text{or Ph}^{\bullet+})]$ pair. Both of these species can be produced in significant quantities, as the driving force for electron transfer in these donor-acceptor pairs is quite similar ($\Delta G^{\circ} = 2.0$ and 1.8 eV,

respectively),⁷ which also means that the BnO^{\bullet} species can oxidize the terminal naphthyl groups due to the slightly positive driving force for this process ($\Delta G^{\circ} = 0.2 \text{ eV}$). These electron transfer processes were previously reported to be rapid enough to completely quench the typically strong fluorescence from the 1,3-bis(methyleneoxy)benzene groups,¹⁴ and this appears to be supported by the lack of fluorescence in the BBnV^{6+} dendrimers in this study.

The proposed electron transfer kinetics of these dendrimers is shown in **Figure 3.14**. Rapid electron transfer initially yields a MV^{\bullet} cation radical and an oxidized donor group on the vicinal 1,3-bis(methyleneoxy)benzene unit, which can then accept an electron *via* back E_tT to quench the MV^{\bullet} species, or can accept an electron from a neighbouring BnO group. The latter pathway uncouples the radical within the MV^{\bullet} species from its hole by causing hole migration out onto the dendrimer arm, causing long-term charge trapping within the tris(methyl viologen) core. Furthermore, this migrated hole is susceptible to interception by contaminants in solution.

This kinetic scheme affords some insight into the dynamics on display in the laser flash photolysis results. The absorbance observed at both 400 and 590 nm in the 1st–3rd generation dendrimers is, as previously stated, due to formation of the MV^{\bullet} cation radical (i.e. a $[\text{MV}^{\bullet}/\text{BnO}^{\bullet}]$ pair). Thus, the rapid exponential decay that follows is ostensibly due to radical/hole recombination by back E_tT from the MV^{\bullet} to the BnO^{\bullet} group, whereas the long-lived absorbance accrues from migration of the hole away from the dendrimer core. Providing that the solvent is sufficiently pure and that the solution is free

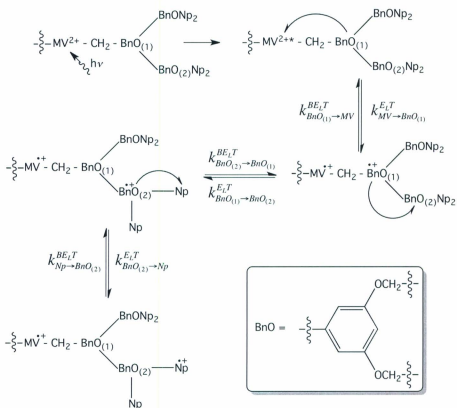


Figure 3.14 Hole migration *via* sequential E_LT processes upon photoexcitation of the tris(methyl viologen) core in NB2V6⁺ (remainder of structure omitted for the sake of clarity). Hole quenching side reactions are not shown but are possible from all BnO• and Np• states.

of oxygen, the resultant charge separated species should persist until hole migration back towards the core re-enables radical/hole recombination. While the [MV•/Np•] pair does lie at a slightly lower potential than the [MV•/BnO•] pair, the difference is sufficiently small that some amount of reverse electron transfer will occur over time, eventually

leading to quenching of the reduced core and relaxation of the chromophore to the ground state. Thus, we see that while the excited state behavior of these dendritic chromophores is initially determined by the methyl viologen units in the dendrimer core, it is the interplay of $E_L T$ processes in the BnO and Np groups on the dendrimer arms that drives the excited state dynamics of these molecules. Importantly, this observation is key to understanding the rather more complex dynamics observed in **BB0V⁶⁺**.

3.4.2.4 The Energy Gap Law in Electron Transfer in **BB0V⁶⁺**.

BB0V⁶⁺ stands apart from the other dendrimers in this work in that the dendrimer arms of this species lack both naphthyl and 1,3-bis(methyleneoxy)benzene units, consisting instead of a 2-carbon aliphatic bridge terminated by a phenyl group (Figure 3.6). Therefore, the fact that 266 nm excitation of **BB0V⁶⁺** yields $MV^{\bullet+}$ cation radical transient absorbance indicates that, just as with the other dendrimers, electron transfer also occurs from the phenyl groups to the core. What is also clear from the results of laser flash photolysis observed at 590 nm is that there is little to no decay of this $MV^{\bullet+}$ state on the $\sim 50 \mu s$ timescale being probed by the spectrometer, indicating that there is some unique feature of this zeroth-order dendrimer that is preventing charge recombination and subsequent relaxation of the chromophore.

The laser flash photolysis results acquired at 400 nm demonstrate an initial decay process of $\tau = (13.2 \pm 0.4) \mu\text{s}$, and as it has already been stated that this is not due to the $\text{MV}^{\bullet+}$ cation radical, it stands to reason that this feature is due to the dendrimer arm of BB0V^{6+} ; more precisely, it must be due to the decay of a substituted benzene cation radical, which are known to absorb at and around 400 nm.²⁴⁻²⁶ The lack of any other decay processes at 400 or – importantly – at 590 nm indicate that this transient species is being quenched by something other than the ostensibly monoreduced tris(methyl viologen) core, and in the absence of any other suitable functional groups on the dendrimer itself, it would seem that this quenching is likely due to a scavenger species of some sort (such as oxygen, or a solvent contaminant/impurity such as acrylonitrile). As a result of this quenching, the electron that was transferred to the dendrimer core can no longer undergo radical/hole recombination, and thus it remains trapped on the methyl viologen moiety until such a time as an opportunistic quencher (likely O_2) can scavenge this radical. Indeed, a decrease in $\text{MV}^{\bullet+}$ absorbance was seen in NB1V^{6+} in high-purity solvent relative to that seen in lower-quality solvent (Figure 3.15), which would imply that a reduction in the rate of quenching by radical scavengers leads to less excited state quenching and permits more back $\text{E}_\text{L}\text{T}$ to take place, reducing the amount of $\text{MV}^{\bullet+}$ and thus also the absorbance intensity detected by the UV-Vis spectrophotometer. It has been reported that benzene and/or alkylbenzene cation radical is susceptible to deprotonation by a suitable base; it is likely that this is a contributing factor in the interception of this radical species by opportunistic scavengers.

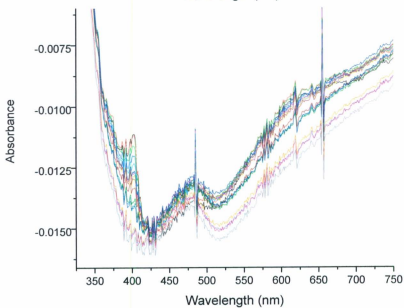
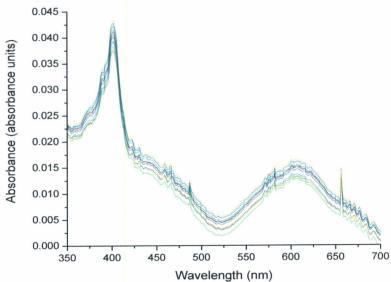


Figure 3.15 UV-Vis spectra of NB1V^{6+} in ACS CH_3CN (top) and Honeywell B & J Brand CH_3CN (bottom) following 266 nm excitation at (298 ± 3) K.

While this interpretation of the results explains the unusually long-lived absorbance of the $MV^{\bullet+}$ cation radical, it is not yet clear why this species is observed to decay exponentially in all dendrimers, save for $BB0V^{6+}$. That there exists a barrier to back E_LT in the $BB0V^{6+}$ species that is present in neither the 1st – 3rd generation dendrimers nor in $NB0V^{6+}$ clearly indicates that this effect is due to a combination of (a) the presence of terminal benzene groups and (b) the complete absence of 1,3-bis(methyleneoxy)benzene or terminal naphthalene units. Recall that the similar values of ΔG^\ominus for electron transfer in the latter two groups enable hole migration and, as a result, are responsible for the biphasic kinetics observed in the larger dendrimers at 400 and 590 nm. It is therefore interesting to note that the oxidation potentials of naphthalene and benzene versus SCE are 1.78 and 2.48 V, respectively.^{26,27} Therefore, whereas there is a positive driving force of 0.2 eV for oxidation of a terminal naphthyl group by $BnO^{\bullet+}$, comparison of the oxidation potentials indicates that oxidation of a terminal phenyl group under the same conditions is energetically uphill by -0.5 eV; this in turn encourages $MV^{\bullet+}$ quenching by back E_LT . While the oxidation potential of benzene is significantly higher than that of naphthalene, it is important to note that its ionization potential of 9.25 eV,²⁸ while very large, is still below the 10.8 eV threshold reported for oxidation by $MV^{\bullet+}$.¹

What is even more important than this interpretation of the data is that the resultant benzene cation radical lies at a higher potential than either the naphthalene or 1,3-bis(methyleneoxy)benzene cation radicals relative to the ground state. Electron transfer to the MV^{2+} group by a benzene unit yields an excited state whose potential energy surface

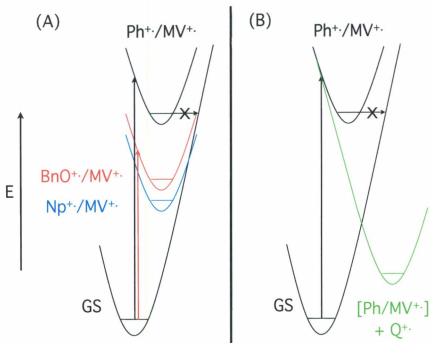


Figure 3.16 Illustration of potential energy surfaces corresponding to possible reaction pathways of the BBnV^{6+} and NBnV^{6+} dendrimers. (a) The $[\text{Ph}^{\bullet}/\text{MV}^{\bullet}]$ charge-separated state lies in the inverted region, attenuating the rate of relaxation by charge recombination. The $[\text{BnO}^{\bullet}/\text{MV}^{\bullet}]$ and $[\text{Np}^{\bullet}/\text{MV}^{\bullet}]$ PE surfaces are not as nested and can easily undergo exchange with each other. (b) Deprived of a facile back-reaction pathway, the $[\text{Ph}^{\bullet}/\text{MV}^{\bullet}]$ state is quenched intermolecularly.

lies at higher energy and further into the inverted region (Figure 3.16). Therefore, the attenuation of back $\text{E}_{\text{L}}\text{T}$ in BB0V^{6+} is as predicted by energy gap law, whereby the rate of decay of an excited state is inversely proportional to the driving force for this process (as stated in the Introduction). This is due to the lack of coupling between the potential energy surface for the excited state and an appropriate acceptor mode of a lower-lying

potential energy surface. Thus, while the Np^{\bullet} and BnO^{\bullet} species can undergo E_LT between themselves and, to a small degree, with the MV^{\bullet} unit, back E_LT from the Ph^{\bullet} species is energetically disfavoured. As a result, the benzene cation radical (which is a very strong oxidant) preferentially reacts with other radical scavengers in solution, trapping the radical in the tris(methyl viologen) core.

3.4.3 Emission in NBnV^{6+} Dendrimers.

Initially it was thought that all the dendritic compounds studied in this work were non-emissive, and that is effectively the case on the timescales being probed by a steady-state spectrofluorometer. However, subsequent laser flash photolysis experiments have shown that there is indeed an emission observed in the NBnV^{6+} ($n = 1 - 3$) dendrimers when the solvent being used is sufficiently pure, though this signal could not be time-resolved as it was convoluted in the laser pulse. It is nonetheless possible, in concert with the results previously discussed in this document, to glean some insight into the excited state behavior of this class of compounds from this brief luminescence.

These dendrimers are composed of methyl viologen, 1,3-bis(methyleneoxy)benzene, and naphthalene units, all of which yield emission when in the appropriate environment. However, it has been shown previously that neither the MV^{2+} nor BnO^{\bullet} species are fluorescent in these types of dendrimers, as the rapidity of electron transfer preemptively quenches these luminescent states; therefore, the emission observed in the NBnV^{6+} dendrimers originates from the terminal naphthalene groups. MV^{2+} excitation rapidly causes E_LT from the vicinal BnO , and the resultant electron hole propagates away from

the dendrimer core towards the terminal naphthyl units. Examination of the thermodynamic driving force for each E_{LT} step shows that this is possible because transfer through the BnO units to the naphthyl-rich periphery is energetically downhill by ~ 0.2 eV. The end result is that excitation of the tris(methyl viologen) core in these dendrimers causes rapid production of the Np^{\bullet} species, which is ostensibly responsible for the emission seen in these dendrimers; the lack of observable emission in any of the benzyl-capped $BBnV^{6+}$ dendrimers seems to support this observation as well. Furthermore, using a high-quality spectroscopic grade solvent will reduce radical quenching rates and extend the lifetime of the Np^{\bullet} species, enhancing the opportunity for emission to accrue from this state. However, the clear lack of emission in the $NBOV^{6+}$ molecule shows that Np^{\bullet} is not the source of fluorescence either, as it would stand to reason that this species should yield the greatest emission intensity relative to its long-lived transient absorbance intensity (which is due to the MV^{\bullet} cation radical), owing to the fact that the lack of 1,3-bis(methyleneoxy)benzene groups attenuates back E_{LT} from the Np^{\bullet} to the MV^{\bullet} unit in 0th generation dendrimers relative to the larger molecules.

An insight into this dilemma is provided by a slight modification of an experiment carried out on $BBOV^{6+}$, wherein ground state absorbance spectra of $NB1V^{6+}$ were acquired in both low-quality and high-quality (Figure 3.15) grades of CH_3CN immediately following excitation by a 266 nm excitation source. The absorbances at 400 nm and ~ 600 nm observed in reagent grade CH_3CN are a clear indication of formation and persistence of the MV^{\bullet} cation radical due to trapping of the injected electron inside the tris(methyl

viologen) core, which in turn is due to hole quenching, made possible by the presence of opportunistic radical scavengers in the low-quality solvent. This is in stark contrast to the spectra acquired in high-quality spectroscopic grade CH_3CN , wherein a dramatic reduction in the intensity of MV^{\bullet} absorbance is observed; in fact, this data was collected following 25 consecutive 266 nm pulses from an Nd:YAG excitation source. Simply put, the comparative lack of contaminants in the high-quality solvent neither causes radical quenching nor attenuation of radical/hole recombination, reducing the lifetime of the MV^{\bullet} species and accordingly decreasing its absorbance at 400 and ~600 nm.

The spectra acquired in high-quality solvent differed from those acquired in the low-quality solvent in another important way: the absorbance feature that is centred at 475 nm in the high-quality solvent spectra is unique to this environment, and did not manifest itself in the other solvent system under any circumstances. Clearly, the solvent dependence of both the new absorbance band and the rapid emission indicates that these are spectral markers for another transient species formed in the $\text{NB}_n\text{V}^{\bullet}$ ($n > 0$) dendrimers, one whose lifetime appears to be sensitive to radical quenching processes. These results are ascribed to formation of a naphthalene dimer cation radical (Np_2^{\bullet} in Figure 3.17), which is known to exhibit spectral features that strongly resemble those observed in this study and have been observed in other naphthalene-containing dendrimers.^{7,29-31} This complex is formed from the combination of a naphthalene cation radical species with a nearby naphthalene group. Assigning the emission to this complex logically precludes their detection in the benzene-capped dendrimers, and upon

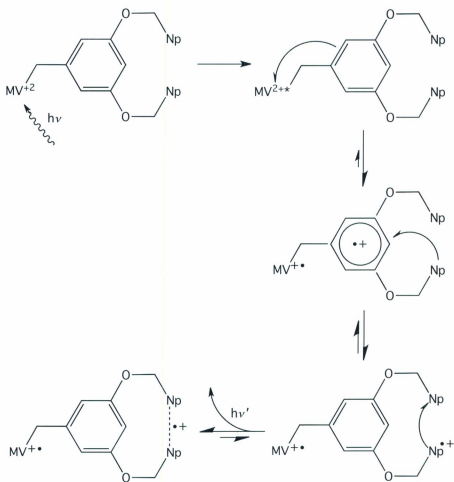


Figure 3.17 Electron transfer pathway and naphthalene cation radical dimer formation in $NB1V^{6+}$ (majority of structure omitted for simplicity).

consideration of the structure of $NB0V^{6+}$ it becomes apparent that such a small structure cannot easily reorganize itself to accommodate facile dimerization of the terminal naphthalene functionalities. Indeed, it has been previously demonstrated that when

combining to form an excimer, naphthalenes preferentially arrange themselves to yield a π -stacked symmetrical dimer;^{29,32} this configuration cannot be readily accommodated by the short dendrimer arm lengths of NB0V⁶⁺.

It should be noted that naphthalene cation radical fluoresces and also yields absorbance features at 390, 485, and 570 nm at 77 K in a 1:1 (v/v) 1-chlorobutane/2-methylbutane mixed solvent (though the 570 nm signal disappears upon warming).³⁰ Nonetheless, the lack of observable fluorescence or ~475 nm absorbance in NB0V⁶⁺ confirms that Np^{•+} does not play a role in the spectroscopy of these compounds.

3.5 Conclusions and Future Work.

This research reaffirms the ability of methyl viologen units to act as electron acceptors in synthetic antennae such as dendrimers. These groups are resistant to deleterious side reactions and can store an electron for long periods of time, and the large redox potentials required for E_LT to occur drives hole migration and further chemistry within the dendrons. However, this reactivity is initiated by excitation of the MV²⁺ molecule itself, rather than excitation of the chromophores of the dendrons; this potentially limits the utility of antenna based upon this design to applications where the excitation source is highly-energetic UV light, as it is blind to longer (visible) wavelengths. Nonetheless, other results that were referenced in this research (such as the PTZ-Ru polypyridyl-MV²⁺ polymers of Meyer *et. al.*⁴) demonstrate how these molecules can be incorporated into polymeric structures to assist in both E_LT and E_NT processes. Furthermore, previous work by Ghaddar *et. al.*⁷ and the research presented in this Chapter demonstrate that E_LT

can indeed proceed at reasonably fast rates in small uphill steps, exemplified by the ~ 0.2 eV barrier to $\text{Np} \rightarrow \text{BnO}$ hole transfer. This suggests that it may be possible to widen the window of available wavelengths for excitation through the judicious choice of electron donors and acceptors within a multichromophoric dendrimer.

The ability of a tris(methyl viologen) core to accept an electron is clear. What is less certain is (a) whether each MV^{2+} is capable of simultaneously accepting and storing one electron, (b) whether the electron is trapped on a single MV^{2+} or if there is potential for site hopping, and (c) whether any MV^{2+} acceptor is capable of storing more than one electron at a time. Power dependence studies akin to those used in previous work⁷ would be a logical first step in ascertaining whether it is possible for multiple electron injections to form any doubly-reduced methyl viologen units, while electroanalytical techniques may determine the number of electrons such a tris(methyl viologen) core could accept. The potential for these methyl viologen arrays to function as multielectron trap sites warrants further investigation for scientific interest as well as the possibility of insight into design of multielectron reaction centres.

3.6 References.

- (1) Peon, J.; Tan, X.; Hoerner, J. D.; Xia, C.; Luk, Y. F.; Kohler, B. *J. Phys. Chem. A* **2001**, *105*, 5768.
- (2) Häupl, T.; Lomoth, R.; Hammarström, L. *J. Phys. Chem. A* **2003**, *107*, 435.
- (3) Juris, A. *Annu. Rep. Prog. Chem., Sect. C* **2003**, *99*, 177.
- (4) Sykora, M.; Maxwell, K. A.; DeSimone, J. M.; Meyer, T. J. *Proc. Natl. Acad. Sci. USA* **2000**, *97*, 7687.
- (5) White, B. G. *Trans. Faraday Soc.* **1969**, *65*, 2000.
- (6) Chitose, N.; LaVerne, J. A.; Katsumura, Y. *J. Phys. Chem. A* **1998**, *102*, 2087.
- (7) Ghaddar, T.; Wishart, J.; Thompson, D. W.; Whitesell, J.; Fox, M. A. *J. Am. Chem. Soc.* **2002**, *124*, 8285.
- (8) Mau, A. W.-H.; Overbeck, J. M.; Loder, J. W.; Sasse, W. H. F. *J. Chem. Soc., Faraday Trans. 2* **1986**, *82*, 869.
- (9) Alvaro, M.; Facey, G. A.; García, H.; García, S.; Scaiano, J. C. *J. Phys. Chem.* **1996**, *100*, 18173.
- (10) Farrington, J. A.; Ebert, M.; Land, E. J.; Fletcher, K. *Biochim. Biophys. Acta* **1973**, *314*, 372.
- (11) Marchioni, F.; Venturi, M.; Credi, A.; Balzani, V.; Belohradsky, M.; Elizarov, A.; Tseng, H.; Stoddart, J. F. *J. Am. Chem. Soc.* **2004**, *126*, 568.
- (12) Hiraiishi, T.; Kamachi, T.; Okura, I. *J. Photochem. Photobiol., A* **1998**, *116*, 119.
- (13) Alvaro, M.; Ferrer, B.; García, H. *Chem. Phys. Lett.* **2002**, *351*, 374.
- (14) Ceroni, P.; Vicinelli, V.; Maestri, M.; Balzani, V.; Muller, W. M.; Muller, U.; Hahn, U.; Osswald, F.; Vögtle, F. *New J. Chem.* **2001**, *25*, 989.
- (15) Ong, W.; Kaifer, A. E. *J. Am. Chem. Soc.* **2002**, *124*, 9358.
- (16) Toba, R.; Maria Quintela, J.; Peinador, C.; Roman, E.; Kaifer, A. E. *Chem. Commun.* **2001**, 857.

- (17) Balzani, V.; Bandmann, H.; Ceroni, P.; Giansante, C.; Hahn, U.; Klärner, F.; Müller, U.; Müller, W.; Verhaelen, C.; Vicinelli, V.; Vögtle, F. *J. Am. Chem. Soc.* **2006**, *128*, 637.
- (18) Cameron, C. S.; Gorman, C. B. *Adv. Funct. Mater.* **2002**, *12*, 17.
- (19) Cardona, C. M.; Mendoza, S.; Kaifer, A. E. *Chem. Soc. Rev.* **2000**, *29*, 37.
- (20) Yonemoto, E. H.; Saupé, G. B.; Schmehl, R. H.; Hubig, S. M.; Riley, R. L.; Iverson, B.; Mallouk, T. E. *J. Am. Chem. Soc.* **1994**, *116*, 4786.
- (21) Alstrum-Acevedo, J.; Brennaman, M.; Meyer, T. J. *Inorg. Chem.* **2005**, *44*, 6802.
- (22) Concepcion, J. J.; Jurss, J. W.; Brennaman, M. K.; Hoertz, P. G.; Patrocinio, A. O. T.; Murakami Iha, N. Y.; Templeton, J. L.; Meyer, T. J. *Acc. Chem. Res.* **2009**, *42*, 1954.
- (23) Watanabe, T.; Honda, K. *J. Phys. Chem.* **1982**, *86*, 2617.
- (24) Baciocchi, E.; Del Giacco, T.; Elisei, F. *J. Am. Chem. Soc.* **1993**, *115*, 12290.
- (25) Kim, E. K.; Bockman, T. M.; Kochi, J. K. *J. Am. Chem. Soc.* **1993**, *115*, 3091.
- (26) Merkel, P. B.; Luo, P.; Dinnocenzo, J. P.; Farid, S. *J. Org. Chem.* **2009**, *74*, 5163.
- (27) Gould, I. R.; Ege, D.; Moser, J. E.; Farid, S. *J. Am. Chem. Soc.* **1990**, *112*, 4290.
- (28) Grubb, S. C.; Whetten, R. L.; Albrecht, A. C.; Grant, E. R. *Chem. Phys. Lett.* **1984**, *108*, 420.
- (29) Chandross, E.; Dempster, C. *J. Am. Chem. Soc.* **1970**, *92*, 3586.
- (30) Tsuchida, A.; Tsujii, Y.; Ito, S.; Yamamoto, M.; Wada, Y. *J. Phys. Chem.* **1989**, *93*, 1244.
- (31) Ghaddar, T. H.; Whitesell, J. K.; Fox, M. A. *J. Phys. Chem. B* **2001**, *105*, 8729.
- (32) Pabst, M.; Lunkenheimer, B.; Köhn, A. *J. Phys. Chem. C* **2011**, *115*, 8335.

Appendix A. Quantum Mechanical Description of Transitions Between States.

A.1 The Schrödinger Equation.

Perhaps the most fundamental equation in quantum mechanics is the *Schrödinger equation* (equation [A.1]), which invokes the idea of a wavefunction Ψ that contains a complete description of a system (in this case, a molecule) and the Hamiltonian operator \hat{H} , which in turn is comprised of the sum of operators that make up the kinetic and potential energies of the molecule (equation [A.2]):¹

$$\hat{H}\Psi = E\Psi \quad [\text{A.1}]$$

$$\hat{H} = \hat{T} + V \quad [\text{A.2}]$$

While the classical kinetic energy operator \hat{T} is based on the classical physics relation of momentum and mass ($T = \frac{p^2}{2m}$), Schrödinger instead applied a momentum operator that was appropriate for systems described by wavefunctions (equation [A.3]),

$$\hat{H} = -\frac{\hbar^2}{2m}\nabla^2 + V(\vec{r}, \vec{R}) \quad [\text{A.3}]$$

Considering that the momentum portion of the Hamiltonian will be dependent on the parameters of the atoms and the electrons of the molecule, this expression can be further developed in terms of both the sum of kinetic energies of N nuclei of nuclear charge Z described by coordinate vectors \vec{R} and masses M_N and the sum of kinetic energies of n electrons described by coordinate vectors \vec{r} and mass m :²

$$\hat{H} = -\sum_N \frac{\hbar^2}{2M_N} \nabla_N^2 - \sum_n \frac{\hbar^2}{2m} \nabla_n^2 + V(\vec{r}, \vec{R}) \quad [\text{A.4}]$$

The potential energy function $V(\vec{r}, \vec{R})$ in equation [A.4] describes the forces involved in the interaction of nuclei and electrons with each other within the molecule, and can be expanded into a summation of all possible nucleus-nucleus, electron-electron, and nucleus-electron interactions of the molecule (equation [A.5]):

$$V(\vec{r}, \vec{R}) = -\sum_{N,n} \frac{Z_N e^2}{|R_N - r_n|} + \sum_{N>O} \frac{Z_N Z_O e^2}{|R_N - R_O|} + \sum_{n>o} \frac{e^2}{|r_n - r_o|} \quad [\text{A.5}]$$

The number of dependencies of the operator increases at an alarming rate with increasing molecular size; thus, an exact solution of the Schrödinger equation is impossible for all but the most simplistic quantum mechanical models.

A.2 Born-Oppenheimer Approximation.

Fortunately, an exact solution is rarely, if ever, necessary, because reasonable assumptions and approximations can be made to simplify the computational burden of determining solutions to this equation. Perhaps the most important of these simplifications is the *Born-Oppenheimer approximation*,^{2,3} which arises from the recognition that the masses of the nuclei are many orders of magnitude larger than the mass of an electron, and on short timescales the significantly larger inertial moment

effectively renders the motion of nuclei negligible relative to that of the electrons. Therefore, the Hamiltonian can be separated into its electronic [A.6] and nuclear components, yielding the electronic Schrödinger equation, [A.7]:

$$\hat{H}_e = \sum_n \frac{\hbar^2}{2m} \nabla_n^2 + V_e(\vec{r}, \vec{R}) \quad [\text{A.6}]$$

$$\hat{H}_e \Psi_e(\vec{r}, \vec{R}) = E_e(\vec{R}) \Psi_e(\vec{r}, \vec{R}) \quad [\text{A.7}]$$

Given that nuclear motion is negligible on the timescale of electronic motion, the nuclear coordinates \vec{R} listed in the electronic energy and wavefunction in [A.7] are merely parameters, and the wavefunction solutions of this equation can be further divided into nuclear ($\chi_n(\vec{R})$) and electronic ($\Psi_e(\vec{r}, \vec{R})$) wavefunctions (equation [A.8]):

$$\Psi = \sum_n \sum_e \chi_n(\vec{R}) \Psi_e(\vec{r}, \vec{R}) \quad [\text{A.8}]$$

A.3 Adiabatic Approximation.

While the B-O approximation has simplified the computational burden of solving the Schrödinger equation, equation [A.8] is still dependent on a large number of variables. At this point, adiabatic theory is invoked to further simplify the wavefunctions.⁴ Simply put, the adiabatic approximation states that so long as the rate of change of a Hamiltonian is sufficiently gradual, then the wavefunction of the system will remain in its initial eigenstate irrespective of the eventual total amount of change in the Hamiltonian.^{2,5} Using the wavefunctions of [A.8], elaboration of the Schrödinger equation using the

expanded Hamiltonian of [A.4] yields off-diagonal nuclear kinetic energy terms that can be eliminated, reducing the summation of wavefunctions in [A.8] to a single term (equation [A.9]):

$$\Psi = \chi_v(\vec{R})\Psi_e(\vec{r}, \vec{R}) \quad [\text{A.9}]$$

Finally, the nuclear wavefunction $\chi_v(\vec{R})$ can be determined by the greatly simplified expression [A.10], corresponding to an equation where the potential energy term $V(\vec{r}, \vec{R})$ is equivalent to the electronic energy $E_e(\vec{R})$:

$$\left\{ -\sum_N \frac{\hbar^2}{2M_N} \nabla_N^2 + E_e(\vec{R}) \right\} \chi_v(\vec{R}) = E \chi_v(\vec{R}) \quad [\text{A.10}]$$

While these equations are certainly easier to handle, the solution of the electronic Schrödinger equation is still not trivial because of the complexity of the electronic wavefunction. This is alleviated by treating the electronic wavefunction in terms of its orbital ($\psi_{el}(\vec{r}, \vec{R})$) and spin ($\psi_s(\vec{r}, \vec{R})$) components (equation [A.11]):

$$\Psi(\vec{r}, \vec{R}) = \Psi_e(\vec{r}, \vec{R})\chi_v(\vec{R}) = \psi_{el}(\vec{r}, \vec{R})\psi_s(\vec{r}, \vec{R})\chi_v(\vec{R}) \quad [\text{A.11}]$$

A.4 Formation and Relaxation of Excited States by Radiative Processes.

A.4.1 Absorption of a Photon.

Sections 1.1 and 1.2 introduce a description of the probability - and thus the rate constant - of a transition between two weakly interacting states as initiated by some potential \hat{V} or, more specifically, as initiated by the absorption of a photon. The interaction of a photon with a molecule is a result of the coupling between the electromagnetic field of the photon with that of the molecule. In the event that the energy of this photon ($h\nu$) corresponds to the energy difference between two vibronic states of energies E_1 and E_2 , the energy of the photon will be absorbed by the molecule and the transition will proceed, resulting in the formation of an excited final state that lies at a higher energy than the initial state from which it was formed. As per Einstein, the rate for this absorptive process (R_A) is given in equation [A.12],⁶

$$R_A = N_1 \rho_\nu B_{12} \quad [\text{A.12}]$$

where N_1 is the number of molecules in state 1 (the initial state), ρ_ν is the energy density of radiation with frequency ν , and B_{12} is the Einstein coefficient of absorption.

A.4.2 Spontaneous and Stimulated Emission of a Photon From an Excited State.

From this excited state there are two radiative (i.e. involving the release of a photon) pathways for relaxation: *spontaneous emission* and *stimulated emission*.⁷ Just as a molecule can accept photons of energy $h\nu$ to yield an excited state, it can also decay from an excited

state of energy E_2' to a lower state of energy E_1' by releasing a photon of energy $E_2' - E_1' = \Delta E' = h\nu'$; it is this ejected photon that is the origin of emission spectra, and the rate of generation of these photons (R_{SPE}) is given in equation [A.13],

$$R_{SPE} = N_2 A_{12} \quad [\text{A.13}]$$

where A_{12} is the Einstein coefficient of spontaneous emission, and N_2 is the number of molecules in state 2 (the excited state).

Spontaneous emission may be thought of as being the reverse of the mechanism of photon absorption, but as equation [A.13] demonstrates, the rate of emission by this process is unaffected by the electromagnetic field of light and only depends on the quantity of excited molecules populating state 2. Stimulated emission, on the other hand, arises in situations where the energy supplied to the molecule by the electromagnetic field of the light is quite large, and is shown to be a conceptual opposite of the process of absorption by equation [A.14],

$$R_{STE} = N_2 \rho_\nu B_{21} \quad [\text{A.14}]$$

where B_{21} is the Einstein coefficient of absorption/stimulated emission, and is related to the coefficient of absorption A by^{8,9}

$$A = 8\pi h c n^3 \langle \hat{\nu}^{-3} \rangle^{-1} B \quad [\text{A.15}]$$

where c is the speed of light, n is the refractive index of the medium, and $\langle \hat{\nu}^{-3} \rangle^{-1}$ is the inverse of the average energy value of $\hat{\nu}^{-3}$ of the emission. In situations where the energy levels being described are non-degenerate, $B_{12} = B_{21} = B$. $\langle \hat{\nu}^{-3} \rangle^{-1}$ can be evaluated as

$$\langle \hat{\nu}^{-3} \rangle^{-1} = \frac{\left(\int I(\hat{\nu}) d\hat{\nu} \right)}{\left(\int \frac{I(\hat{\nu})}{\hat{\nu}^3} d\hat{\nu} \right)} \quad [\text{A.16}]$$

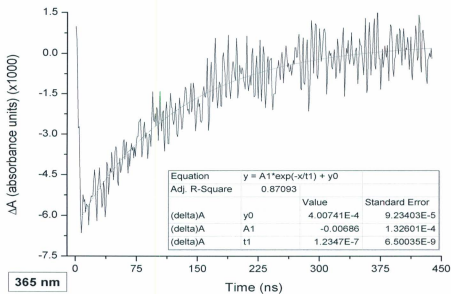
where I is the intensity of emission in photons $\text{cm}^{-1} \text{ s}^{-1}$.^{8,9} Just as absorption of a photon required energy transfer from the electromagnetic field of the light to the molecule, stimulated emission arises from a strong interaction of the EM field with the molecule, which initiates energy transfer from the molecule to the field and results in ejection of a photon.

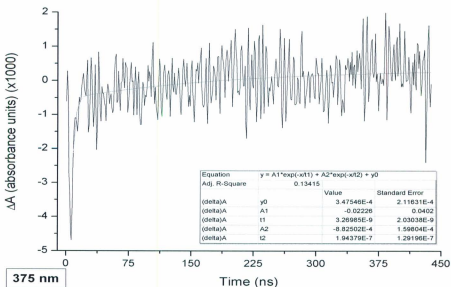
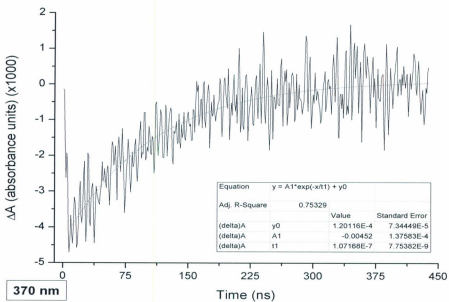
A.5 References.

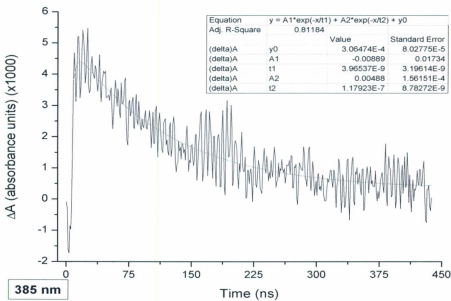
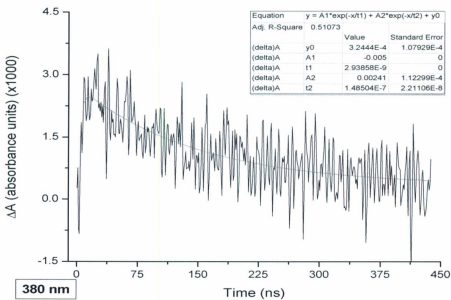
- (1) Merzbacher, E. *Quantum Mechanics*; 2nd ed.; Wiley & Sons: New York, 1970.
- (2) In *Comprehensive Chemical Kinetics*; Compton, R. G., Ed.; Elsevier: 1990; Vol. Volume 30, p 69.
- (3) Eckart, C. *Phys. Rev.* **1935**, *46*, 383.
- (4) Claude, J. P. Ph.D. Dissertation, University of North Carolina at Chapel Hill, 1995.
- (5) Turro, N. J.; Ramamurthy, V.; Scaiano, J. C. *Modern Molecular Photochemistry of Organic Molecules*; University Science Books: Sausalito, California, 2010.
- (6) Loudon, R. *The Quantum Theory of Light*; 2nd ed.; Clarendon Press: London, 1983.
- (7) Jortner, J.; Rice, S. A.; Hochstrasser, R. M. *Advances in Photochemistry*; Wiley-Interscience: New York, 1969; Vol. 7.
- (8) Strickler, S.; Berg, R. J. *Chem. Phys.* **1962**, *37*, 814.
- (9) Graff, D. K. Ph.D. Dissertation, University of North Carolina at Chapel Hill, 1994.

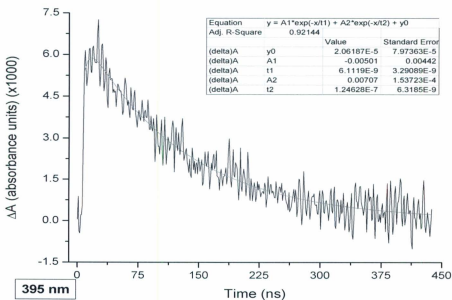
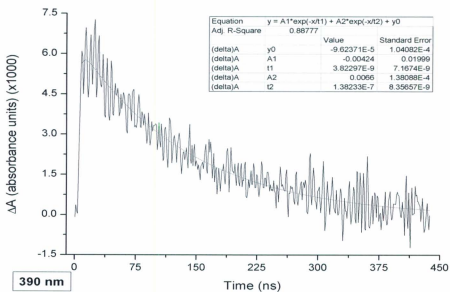
Appendix B. Laser Flash Photolysis Data.

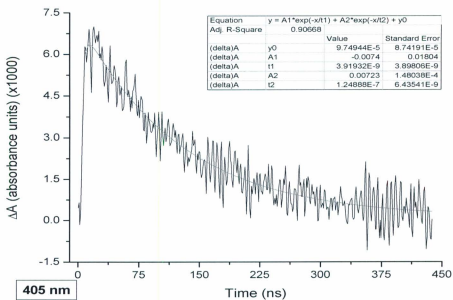
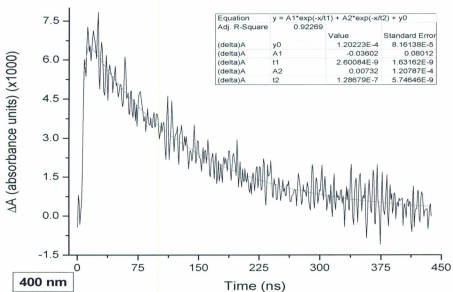
- B.1 Transient absorption decay traces from 365 – 510 nm and 520 – 650 nm upon 355 nm excitation of RuD0 in CH₃CN solution at 298 K (450 ns timescale, 5 nm increments, 2.325 nm slit width).

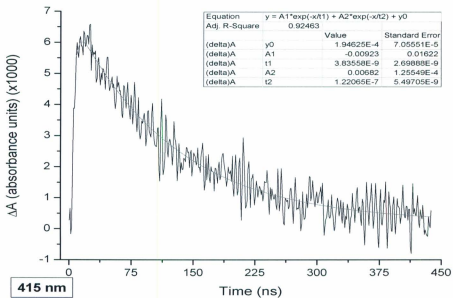
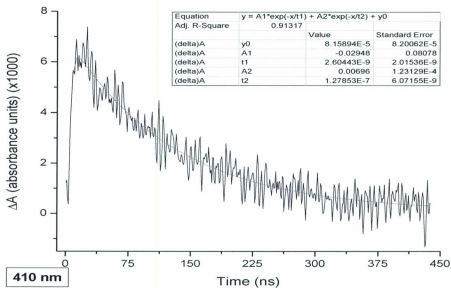


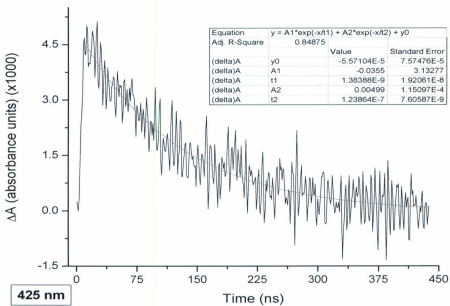
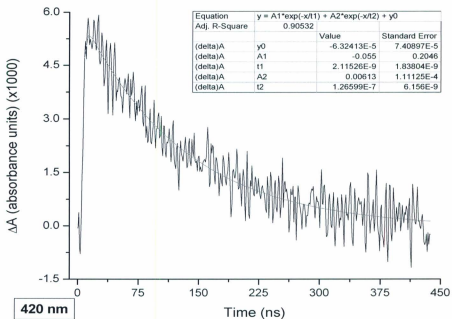


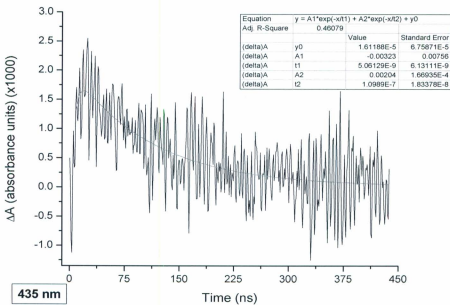
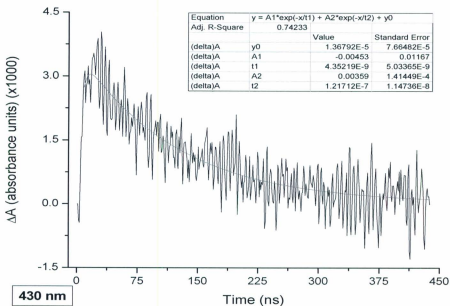


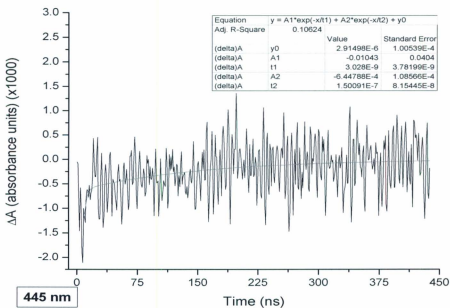
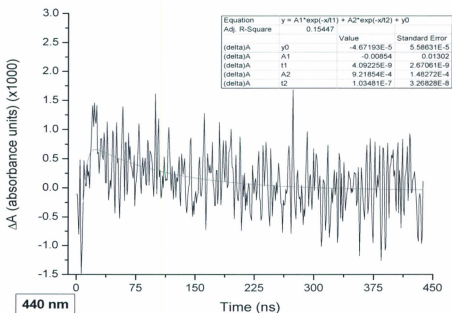


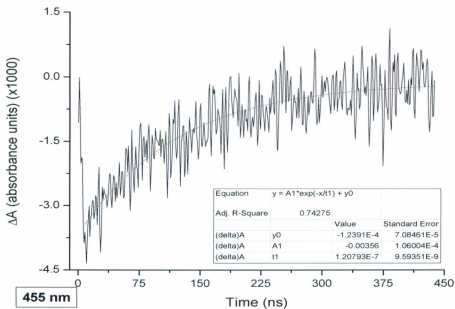
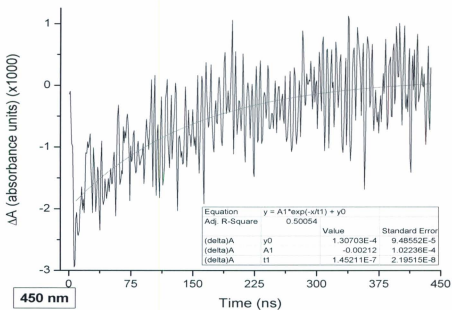


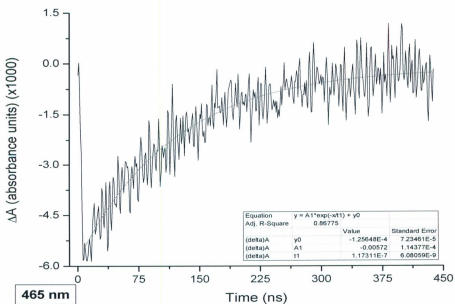
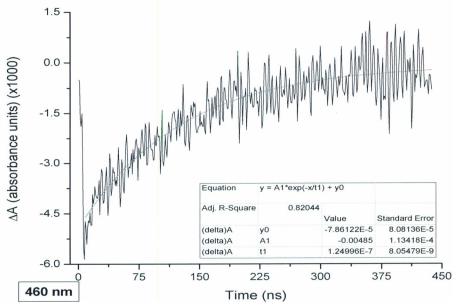


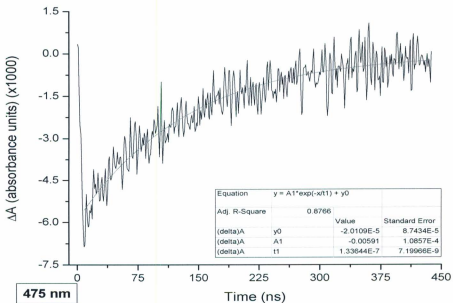
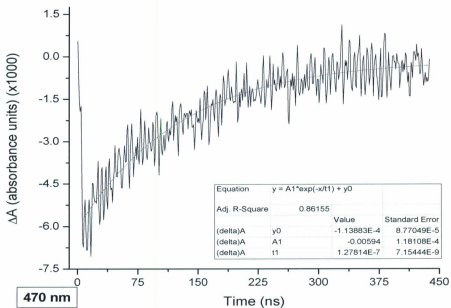


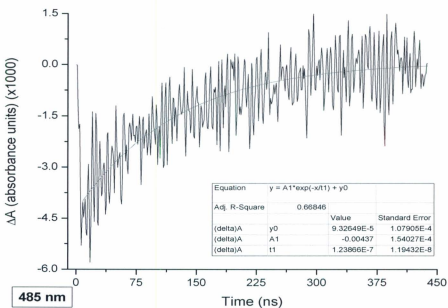
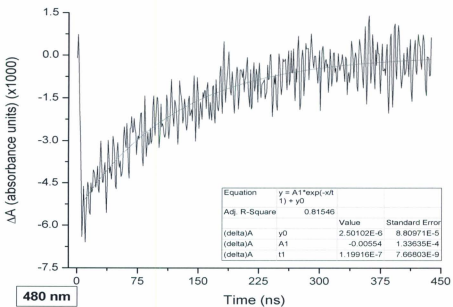


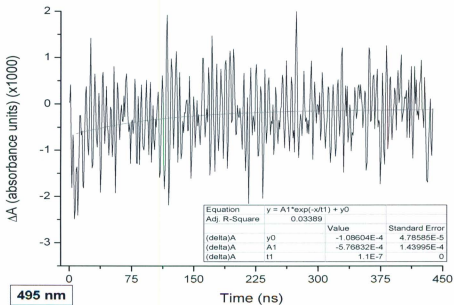
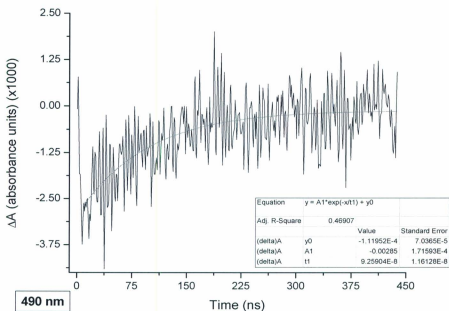


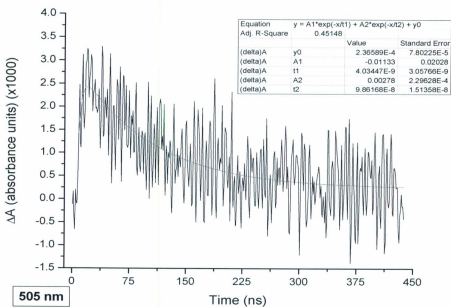
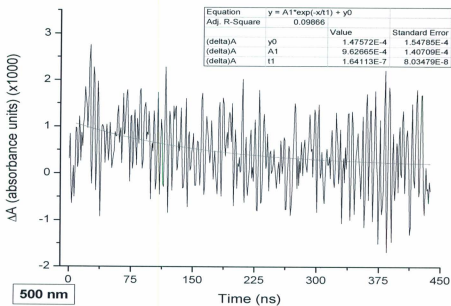


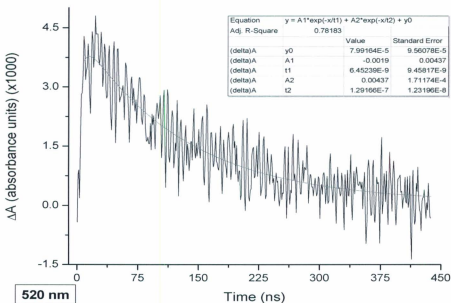
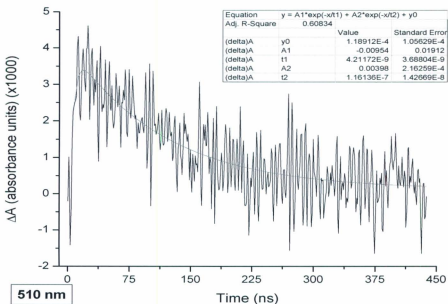


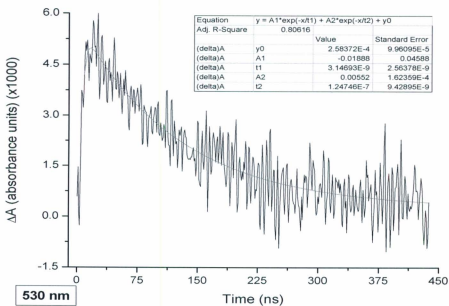
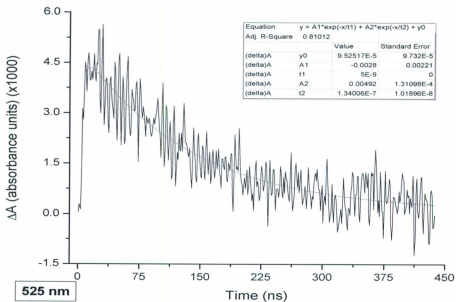


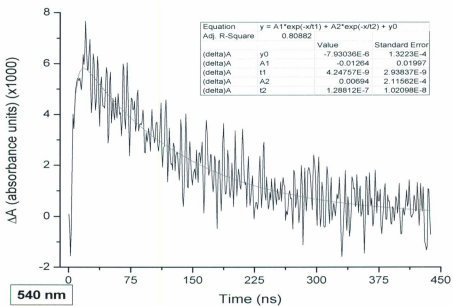
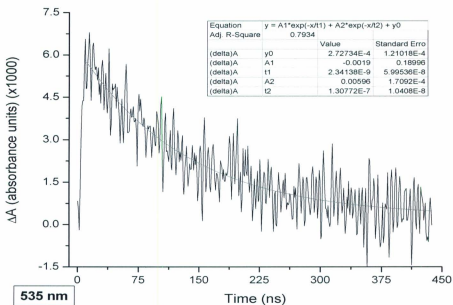


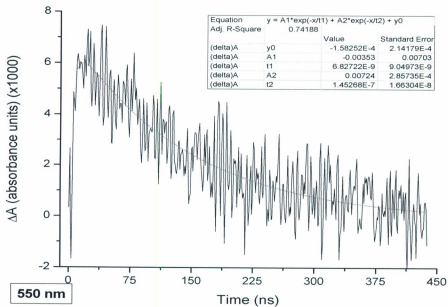
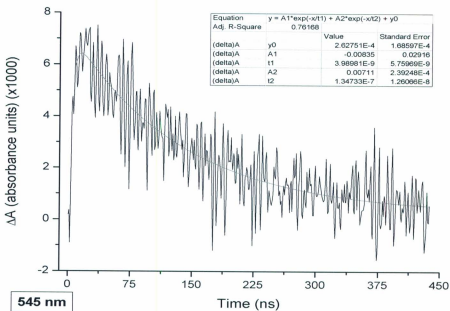


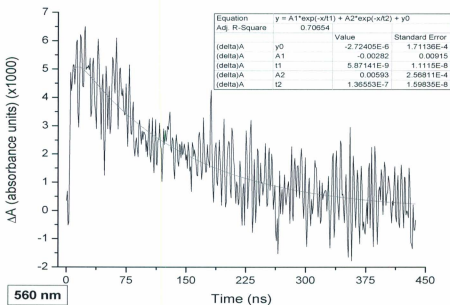
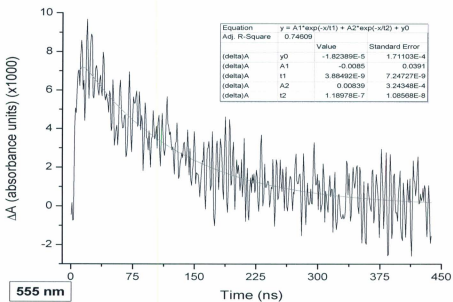


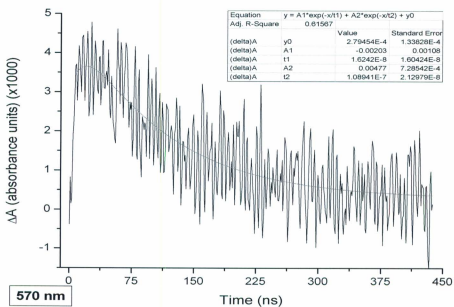
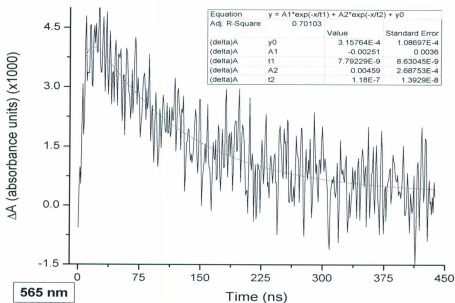


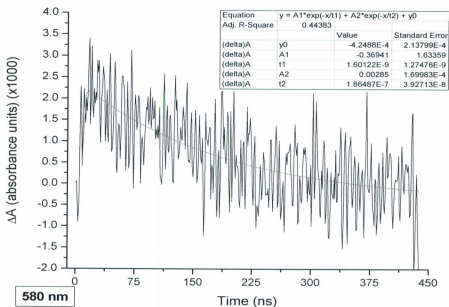
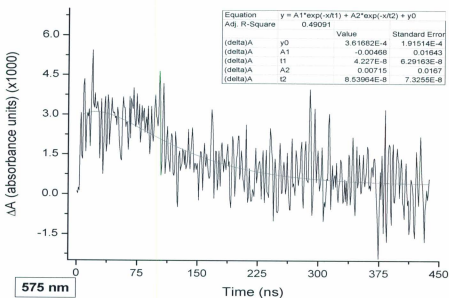


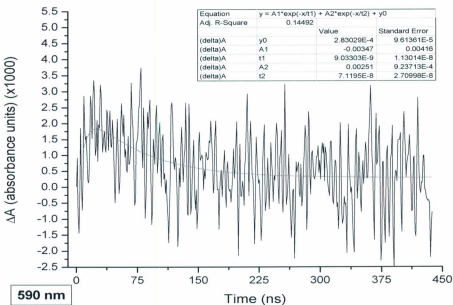
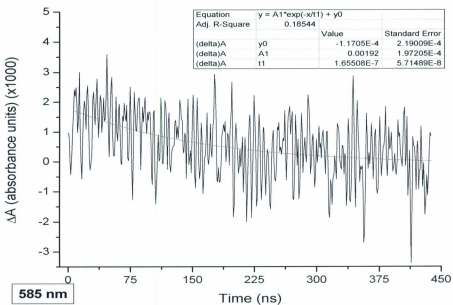


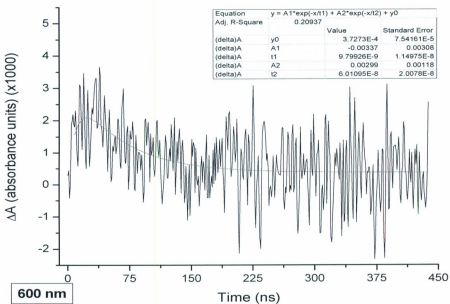
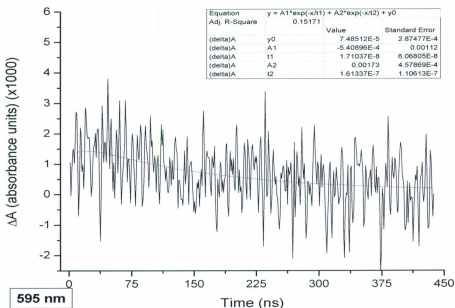


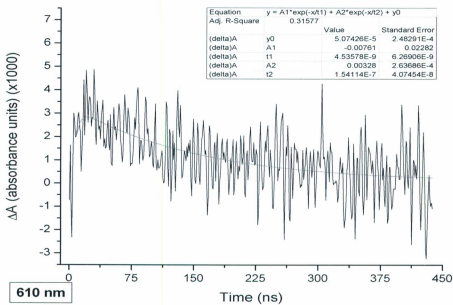
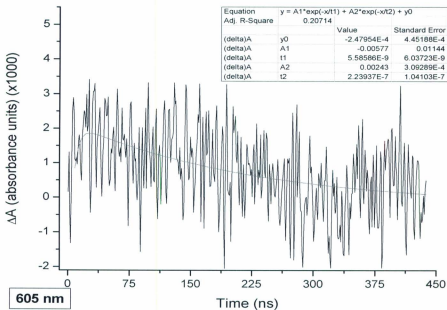


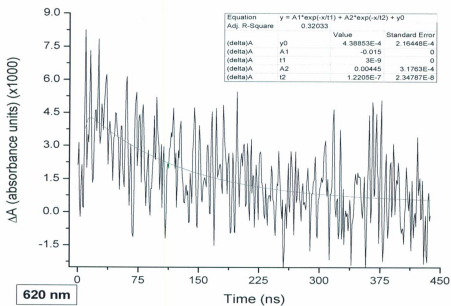
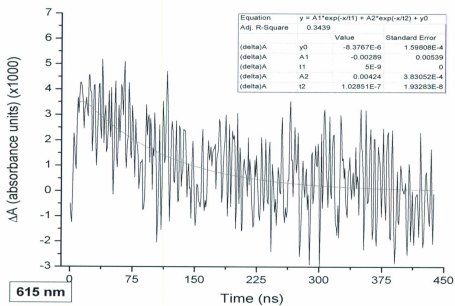


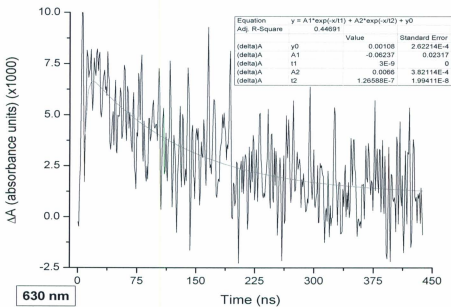
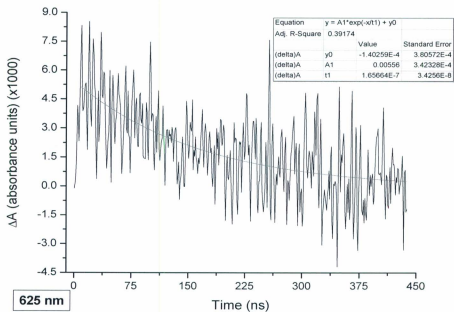


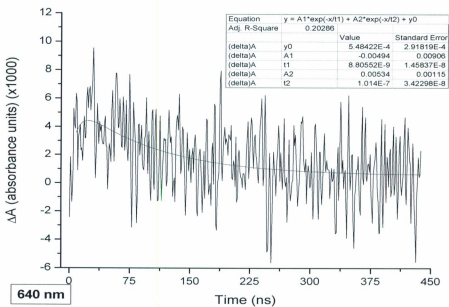
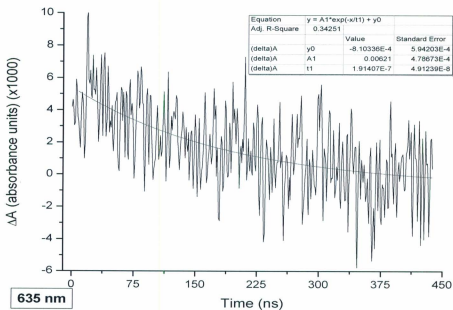


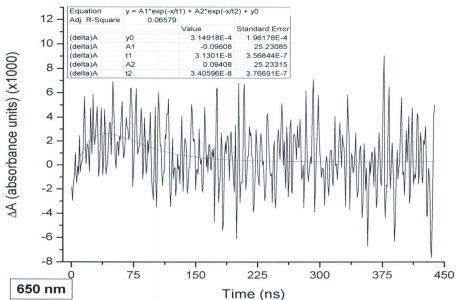
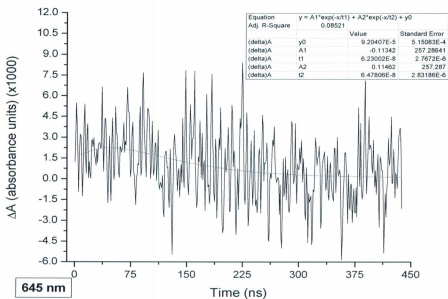












B.2

Transient absorption decay traces from 400 – 690 nm upon 355 nm excitation of RuD0 in a glass-supported PMMA film at 298 K (9.0 μ s timescale, 10 nm increments, 2.325 nm slit width).

